

# Energy-stable boundary conditions based on a quadratic form: Applications to outflow/open-boundary problems in incompressible flows



Naxian Ni, Zhiguo Yang, Suchuan Dong\*

Center for Computational & Applied Mathematics, Department of Mathematics, Purdue University, West Lafayette, IN 47907, USA

## ARTICLE INFO

### Article history:

Received 18 July 2018

Received in revised form 17 March 2019

Accepted 13 April 2019

Available online 18 April 2019

### Keywords:

Energy stability

Energy stable boundary condition

Energy balance

Backflow instability

Open boundary condition

Outflow boundary condition

## ABSTRACT

We present a set of new energy-stable open boundary conditions for tackling the backflow instability in simulations of outflow/open boundary problems for incompressible flows. These boundary conditions are developed through two steps: (i) devise a general form of boundary conditions that ensure the energy stability by re-formulating the boundary contribution into a quadratic form in terms of a symmetric matrix and computing an associated eigen problem; and (ii) require that, upon imposing the boundary conditions from the previous step, the scale of boundary dissipation should match a physical scale. These open boundary conditions can be re-cast into the form of a traction-type condition, and therefore they can be implemented numerically using the splitting-type algorithm from a previous work. The current boundary conditions can effectively overcome the backflow instability typically encountered at moderate and high Reynolds numbers. In general they give rise to a non-zero traction on the entire open boundary, unlike previous related methods which only take effect in the backflow regions of the boundary. Extensive numerical experiments in two and three dimensions are presented to test the effectiveness and performance of the presented methods, and simulation results are compared with the available experimental data to demonstrate their accuracy.

© 2019 Elsevier Inc. All rights reserved.

## 1. Introduction

Outflow/open-boundary problems are an important and challenging class of problems for incompressible flow simulations. Several types of flows that are of practical engineering/biological significance belong to this class, such as wakes, jets, shear layers, cardiovascular and respiratory flows. The predominant challenge in the numerical simulations of such problems lies in the treatment of the outflow or open boundary [21,32]. At low Reynolds numbers a number of types of open/outflow boundary conditions (OBC) can work well and lead to reasonable simulation results. But when the Reynolds number increases beyond some moderate value, typically close to 2000 (which can be as low as several hundred depending on the flow geometry), the so-called backflow instability (see e.g. [10]) will become a severe issue, and many OBCs that work well for low Reynolds numbers cease to work. Backflow instability refers to the numerical instability caused by the un-controlled energy influx into the domain through the open/outflow boundary, often associated with strong vortices or backflows on such boundaries. A telltale symptom of this instability is that an otherwise stable computation blows up instantly when a

\* Corresponding author.

E-mail address: sdong@purdue.edu (S. Dong).

vortex reaches the open/outflow boundary [11,13,35,19]. It is observed that usual measures such as increasing the mesh resolution or reducing the time step size do not help with this instability [12].

To tackle the backflow instability, the energy influx into the domain through the open boundary, if any, must be controlled in some fashion. Employing a large enough computational domain such that vortices can be sufficiently dissipated before reaching the outflow boundary, or artificially increasing the viscosity in a region near/at the outflow boundary (so-called sponge) such that vortices can be smoothed out or sufficiently weakened, are some measures in actual simulations. These measures may not be desirable in terms of e.g. the increased computational cost due to the larger domain or the negative influence on the accuracy due to the artificially modified viscosity in regions of the flow, and additionally they may not always be effective with the increase of Reynolds number.

How to algorithmically control the energy influx through the open boundary by devising effective open boundary conditions seems a more attractive approach. A number of researchers have contributed to this area, and there appears to be a surging interest in recent years. In the early works (see e.g. [6,7]) the traction on the open boundary is modified to include a term  $\frac{1}{2}(\mathbf{n} \cdot \mathbf{u})^- \mathbf{u}$ , where  $\mathbf{u}$  and  $\mathbf{n}$  are respectively the velocity on and the directional unit vector of the boundary, and  $(\mathbf{n} \cdot \mathbf{u})^-$  is equal to  $\mathbf{n} \cdot \mathbf{u}$  if  $\mathbf{n} \cdot \mathbf{u} < 0$  and zero otherwise. This OBC has also appeared or is studied in some later works; see e.g. [25,16,18,5] among others. A variant of this form, with a term  $(\mathbf{n} \cdot \mathbf{u})^- \mathbf{u}$  in the traction (without the 1/2 factor), has been investigated in a number of works (see e.g. [1,26,30,20,23]). It is noted that in [26] a form  $\beta(\mathbf{n} \cdot \mathbf{u})^- \mathbf{u}$ , with a constant  $0 < \beta < 1$ , has also been considered. In [12] an OBC with a modified traction term  $[\frac{1}{2}|\mathbf{u}|^2 \mathbf{n}] \Theta_0(\mathbf{n}, \mathbf{u})$  is suggested, where  $\Theta_0(\mathbf{n}, \mathbf{u})$  is a smoothed step function essentially taking the unit value if  $\mathbf{n} \cdot \mathbf{u} < 0$  and vanishing otherwise. So this additional traction term only takes effect in regions of backflow on the open boundary, and has no effect in normal outflow regions or if no backflow is present. Note that this is very different from the total pressure ( $p + \frac{1}{2}|\mathbf{u}|^2$ , where  $p$  denotes the normalized static pressure) as discussed in e.g. [22], which can lead to a similar term  $\frac{1}{2}|\mathbf{u}|^2 \mathbf{n}$  on the boundary. This term in the total pressure, unlike that of [12], precludes the energy from exiting the domain even in normal outflow situations, resulting in poor and unphysical simulation results [22]. In contrast, the boundary condition of [12] can ensure the energy stability on the open boundary and produce accurate simulation results for outflow problems. In [14] a general form of OBCs that ensure the energy stability on the open boundary has been proposed. This form contains those of [6,1,20,23,12] as particular cases. More importantly, the general form suggests other forms of energy-stable OBCs involving terms such as  $\frac{1}{4} [|\mathbf{u}|^2 \mathbf{n} + (\mathbf{n} \cdot \mathbf{u}) \mathbf{u}] \Theta_0(\mathbf{n}, \mathbf{u})$ ,  $\frac{1}{2} [|\mathbf{u}|^2 \mathbf{n} + (\mathbf{n} \cdot \mathbf{u}) \mathbf{u}] \Theta_0(\mathbf{n}, \mathbf{u})$ , and  $[|\mathbf{u}|^2 \mathbf{n}] \Theta_0(\mathbf{n}, \mathbf{u})$ . Several of them have been studied in detail in [14]. It is observed that the term  $(\mathbf{n} \cdot \mathbf{u}) \mathbf{u}$  (with or without the 1/2 factor) in the OBC tends to cause the vortices to move laterally as they cross the open boundary, while the term  $|\mathbf{u}|^2 \mathbf{n}$  tends to squeeze the vortices along the direction normal to the open boundary. In [10] a convective-like energy-stable OBC is proposed, which contains an inertia term (velocity time-derivative) and represents a Newton's second-law type relation on the open boundary. Under certain situations it can be reduced to a form that is reminiscent of the usual convective boundary condition, hence the name "convective-like" condition. This OBC not only ensures the energy stability but also provides a control over the velocity on the outflow boundary. It is observed in [10] that the inertia term in this OBC allows the vortices to discharge from the domain in a more smooth and natural fashion, when compared with the previous energy-stable OBCs without the inertia term (see e.g. those of [14]). A generalization of this condition to other forms of convective-like energy-stable OBCs has also been provided in [10]. Besides the above methods, other OBCs that can work with the backflow instability also exist. We refer the reader to e.g. those of [2,3] which are given based on a weak formulation of the Navier-Stokes equations, and also to [4] for a recent study of several methods in the context of physiological flows. We also refer to [9,15,38] for methods dealing with two-phase and multiphase outflow/open boundaries and related issues.

The principle for addressing the backflow instability lies in the management and control of the boundary contribution of the open boundary to the energy balance of the system. A key strategy for achieving this is to devise boundary conditions such that the boundary contribution to the energy balance is dissipative (i.e. negative semi-definite) on the open/outflow boundary. This strategy has been employed in the developments of [12,14,10] and several other afore-mentioned methods. Recently, a more systematic roadmap to formulating boundary conditions to ensure the definiteness of the boundary contribution (in the context of compressible Navier-Stokes equations) is proposed in [28]. This roadmap involves three main steps: (i) reformulate the boundary contribution into a quadratic form in terms of a symmetric matrix, (ii) rotate the variables to diagonalize the matrix, and (iii) formulate the boundary condition in the form of the eigen-variables corresponding to the negative eigenvalues expressed in terms of the eigen-variables corresponding to the positive eigenvalues. This procedure is very recently applied in [29] to the incompressible Navier-Stokes equations in two dimensions to investigate the boundary conditions on solid walls and far fields that can bound the energy of the system.

Inspired by [28,29], we develop in this paper a set of new open/outflow boundary conditions for tackling the backflow instability for incompressible flows in two and three dimensions based on the procedure of [28]. By formulating the boundary integral term in the energy balance equation into a quadratic form involving a symmetric matrix, we have derived a general form of boundary conditions that ensure the energy dissipation on the open boundary. It should be pointed out that, due to differences in the formulation of the quadratic form and the symmetric matrix involved therein, the energy-stable boundary conditions obtained here are different from those of [29], even though the procedure used for deriving the boundary conditions is similar.

We find that the energy-stable boundary conditions as devised above based on the quadratic form can be re-formulated equivalently into a traction-type condition similar to those of [12,14], albeit involving a different traction term. More importantly, we observe that the boundary conditions as obtained above in general give rise to poor or even unphysical results

in numerical simulations of outflow problems, even though the computations are indeed stable, unless the algorithmic parameters take certain values for the given flow problem under study. We further observe that the values for the algorithmic parameters that can lead to “good” simulation results, unfortunately, are flow-problem dependent.

An investigation of this issue reveals that the resultant dissipation on the open boundary after imposing these conditions is crucial to and strongly influences the accuracy of simulation results. By requiring that the scale of the boundary dissipation on the open boundary should match a reasonable physical scale, we attain a set of OBCs in two and three dimensions that can effectively overcome the backflow instability and also provide accurate simulation results. This set of new OBCs is different from and not equivalent to the family of conditions developed in [14,12]. For one thing, the new boundary conditions are active (i.e. leading to generally non-zero traction) on the entire open boundary, in both backflow regions and normal outflow regions. In contrast, the previous methods only take effect in the backflow regions of the open boundary, and give rise to a zero traction in normal outflow regions due to the terms like  $\Theta_0(\mathbf{n}, \mathbf{u})$  or  $(\mathbf{n} \cdot \mathbf{u})^-$ .

Therefore, the current energy-stable OBCs with physical accuracy are developed through two steps: (i) devise energy-stable boundary conditions based on a quadratic form in terms of a symmetric matrix, using the procedure of [28]; (ii) require that the boundary dissipation with these conditions should match a physical scale. The boundary conditions resulting from the first step only can lead to poor or even unphysical simulation results, even though the computations are stable.

The contribution of this paper lies in the set of energy-stable and physically-accurate open boundary conditions developed herein for incompressible flows. These OBCs can be implemented numerically with the commonly-used splitting-type schemes for the incompressible Navier-Stokes equations. This is because the current conditions are formulated in a traction form, similar to those of [12,14]. This allows us to employ any of the algorithms developed in the previous works (see [12,14,10]) for simulations with the new OBCs. For the numerical experiments reported in the current work, the algorithm from [10] has been employed.

The current implementation of these OBCs is based on the  $C^0$ -continuous spectral element method [33,24,39], similar to previous works [12,14,10]. It should be pointed out that these boundary conditions are given on the continuum level, irrespective of the numerical methods used for their implementation. They can also be used with other popular techniques such as finite difference, finite element, or finite volume methods.

The rest of this paper is organized as follows. In Section 2 we first derive the general forms of energy-stable boundary conditions, referred to as OBC-A, based on the method of quadratic forms in two/three dimensions. Then we require that the scale of boundary dissipation should match a physical scale, and thus acquire another set of OBCs. Two boundary conditions among this set, referred to as OBC-B and OBC-C, are studied in more detail. The numerical implementation of these boundary conditions is also discussed. In Section 3 we present extensive numerical simulations using two canonical flows, the flow past a circular cylinder and a jet impinging on a wall, to test the accuracy and performance of the boundary conditions. Section 4 concludes the discussions with some closing remarks. Appendix A provides a proof of Theorem 2.1 used in Section 2. Appendix B is a summary of the boundary conditions OBC-A, OBC-B and OBC-C. Appendix C summarizes the numerical algorithm from [10] and provides implementation details of OBCs.

## 2. Energy-stable boundary conditions for incompressible Navier-Stokes equations

### 2.1. Navier-Stokes equations and energy balance relation

Consider a flow domain  $\Omega$  in two or three dimensions, whose boundary is denoted by  $\partial\Omega$ , and an incompressible flow on this domain. Let  $L$  denote a length scale,  $U_0$  denote a velocity scale, and  $\nu_f$  denote the kinematic viscosity of the fluid. The flow is described by the normalized incompressible Navier-Stokes equations,

$$\frac{\partial \mathbf{u}}{\partial t} + \mathbf{u} \cdot \nabla \mathbf{u} + \nabla p - \nu \nabla^2 \mathbf{u} = \mathbf{f}, \tag{1a}$$

$$\nabla \cdot \mathbf{u} = 0, \tag{1b}$$

where  $\mathbf{u}(\mathbf{x}, t)$  is the velocity,  $p(\mathbf{x}, t)$  is the pressure,  $\mathbf{f}(\mathbf{x}, t)$  is an external body force, and  $\mathbf{x}$  and  $t$  are the spatial coordinate and time, respectively.  $\nu$  is the non-dimensional viscosity, given by  $\nu = \frac{1}{Re} = \frac{\nu_f}{U_0 L}$ , where  $Re$  is the Reynolds number. The equations (1a)–(1b) are to be supplemented by appropriate boundary conditions on  $\partial\Omega$ , which is the focus of this work, together with the following initial condition

$$\mathbf{u}(\mathbf{x}, 0) = \mathbf{u}_{in}(\mathbf{x}), \tag{2}$$

where the initial velocity  $\mathbf{u}_{in}$  satisfies equation (1b) and is compatible with the boundary condition on  $\partial\Omega$ .

Taking the  $L^2$  inner product between (1a) and  $\mathbf{u}$  and using integration by part, the divergence theorem and equation (1b), we arrive at the following energy-balance equation

$$\frac{\partial}{\partial t} \int_{\Omega} \frac{1}{2} |\mathbf{u}|^2 = \int_{\Omega} \mathbf{f} \cdot \mathbf{u} - \nu \int_{\Omega} \|\nabla \mathbf{u}\|^2 + \underbrace{\int_{\partial\Omega} \left[ \mathbf{n} \cdot \mathbf{T} \cdot \mathbf{u} - \frac{1}{2} (\mathbf{u} \cdot \mathbf{u}) (\mathbf{n} \cdot \mathbf{u}) \right]}_{\text{boundary term (BT)}}, \tag{3}$$

where  $\mathbf{n}$  is the outward-pointing unit vector normal to  $\partial\Omega$ ,  $\mathbf{T} = -p\mathbf{I} + \nu\nabla\mathbf{u}$  and  $\mathbf{I}$  is the identity tensor.  $\mathbf{T}$  can be roughly considered as the fluid stress tensor. If the external body force is absent ( $\mathbf{f} = 0$ ), the volume integral term on the right hand side (RHS) of the above equation is always dissipative and will not cause the system energy to increase over time. The surface integral term, on the other hand, is indefinite. Its contribution to the system energy depends on the boundary conditions imposed on the domain boundary.

2.2. Energy-stable boundary conditions based on a quadratic form

We are interested in the boundary conditions on  $\partial\Omega$  such that the boundary integral term on RHS of equation (3) is always non-positive. As such, the contribution of the surface integral will not cause the system energy to increase over time. Such boundary conditions are referred to as energy-stable boundary conditions.

Inspired by the strategy of [28] to enforce the definiteness of the boundary contribution, we will first reformulate the boundary integral term in (3) into a quadratic form in terms of a symmetric matrix. Then by looking into the eigenvalues and the associated eigenvectors of this matrix, we formulate the boundary condition in the form of a relation between those eigenvariables corresponding to the eigenvalues of different signs. By imposing a proper condition on the coefficients involved in this relation, the boundary condition can guarantee the negative semi-definiteness of the quadratic form.

The following property about a particular form of symmetric matrices will be extensively used subsequently:

**Theorem 2.1.** Let  $\mathbf{G}$  denote an  $m \times m$  ( $m \geq 1$ ) real symmetric matrix,  $\mathbf{I}_m$  denote the  $m \times m$  identity matrix, and  $\mathbf{A} = \begin{bmatrix} \mathbf{0} & -\mathbf{I}_m \\ -\mathbf{I}_m & \mathbf{G} \end{bmatrix}$ .

Then

- (a) The eigenvalues of  $\mathbf{A}$  are real and non-zero.
- (b)  $\lambda$  is an eigenvalue of  $\mathbf{A}$  if and only if  $(\lambda - \frac{1}{\lambda})$  is an eigenvalue of  $\mathbf{G}$ .
- (c)  $\begin{bmatrix} \mathbf{Z} \\ -\lambda\mathbf{Z} \end{bmatrix}$  is an eigenvector of  $\mathbf{A}$  corresponding to the eigenvalue  $\lambda$  if and only if  $\mathbf{Z}$  is an eigenvector of  $\mathbf{G}$  corresponding to the eigenvalue  $(\lambda - \frac{1}{\lambda})$ .

A proof of this property is provided in Appendix A. This theorem suggests that the eigenvalues and the eigenvectors of the  $2m \times 2m$  matrix  $\mathbf{A}$  can be constructed based on those of the  $m \times m$  matrix  $\mathbf{G}$ . Let  $\xi$  denote an eigenvalue (real) of the symmetric matrix  $\mathbf{G}$ . Then the corresponding eigenvalues of matrix  $\mathbf{A}$  are given by  $\lambda = \frac{\xi}{2} \pm \sqrt{(\frac{\xi}{2})^2 + 1}$ . Therefore, half of the eigenvalues of  $\mathbf{A}$  are positive and half are negative.

2.2.1. Two dimensions (2D)

We first consider two dimensions in space. Let  $\mathbf{n}$  and  $\boldsymbol{\tau}$  denote the unit vectors normal (pointing outward) and tangential to the boundary  $\partial\Omega$ , respectively, and  $\mathbf{n} \times \boldsymbol{\tau} = \mathbf{e}_z$ , where  $\mathbf{e}_z$  denotes the unit vector along the third (i.e.  $z$ ) direction normal to the two-dimensional plane. Define the normal and tangent components of the fluid stress and the velocity on the boundary by

$$T_{nn} = \mathbf{n} \cdot \mathbf{T} \cdot \mathbf{n}, \quad T_{n\tau} = \mathbf{n} \cdot \mathbf{T} \cdot \boldsymbol{\tau}, \quad u_n = \mathbf{n} \cdot \mathbf{u}, \quad u_\tau = \boldsymbol{\tau} \cdot \mathbf{u}, \quad \text{on } \partial\Omega. \tag{4}$$

Note that  $\mathbf{u} = u_n\mathbf{n} + u_\tau\boldsymbol{\tau}$ , and  $\mathbf{n} \cdot \mathbf{T} = T_{nn}\mathbf{n} + T_{n\tau}\boldsymbol{\tau}$  on  $\partial\Omega$ . The boundary term in equation (3) can then be written as a quadratic form with a symmetric matrix  $\mathbf{A}$  as follows,

$$BT = -\frac{1}{2} \begin{bmatrix} T_{nn} \\ T_{n\tau} \\ u_n \\ u_\tau \end{bmatrix}^T \underbrace{\begin{bmatrix} 0 & 0 & -1 & 0 \\ 0 & 0 & 0 & -1 \\ -1 & 0 & u_n & \alpha u_\tau \\ 0 & -1 & \alpha u_\tau & \beta u_n \end{bmatrix}}_{\text{matrix } \mathbf{A}} \underbrace{\begin{bmatrix} T_{nn} \\ T_{n\tau} \\ u_n \\ u_\tau \end{bmatrix}}_{\mathbf{x}} = -\frac{1}{2} \mathbf{x}^T \mathbf{A} \mathbf{x}, \tag{5}$$

where the superscript in  $(\cdot)^T$  denotes transpose,  $\alpha$  a chosen constant satisfying  $0 \leq \alpha \leq \frac{1}{2}$ , and  $\beta = 1 - 2\alpha$ . This matrix has the form as given by Theorem 2.1 with  $m = 2$ , and in this case  $\mathbf{G} = \begin{bmatrix} u_n & \alpha u_\tau \\ \alpha u_\tau & \beta u_n \end{bmatrix}$ . In what follows, we distinguish two cases: (i)  $0 < \alpha \leq \frac{1}{2}$ , and (ii)  $\alpha = 0$ , and treat them individually.

**Case 0**  $< \alpha \leq \frac{1}{2}$ . The matrix **A** defined in (5) has four distinct eigenvalues,

$$\begin{cases} \lambda_1 = \frac{\xi_1}{2} - \sqrt{\left(\frac{\xi_1}{2}\right)^2 + 1}, & \lambda_2 = \frac{\xi_2}{2} - \sqrt{\left(\frac{\xi_2}{2}\right)^2 + 1}, \\ \lambda_3 = \frac{\xi_1}{2} + \sqrt{\left(\frac{\xi_1}{2}\right)^2 + 1}, & \lambda_4 = \frac{\xi_2}{2} + \sqrt{\left(\frac{\xi_2}{2}\right)^2 + 1}, \end{cases} \tag{6}$$

where  $\xi_1$  and  $\xi_2$  are the eigenvalues of the matrix **G** given by,

$$\begin{cases} \xi_1 = (1 - \alpha)u_n + \alpha\sqrt{u_n^2 + u_\tau^2} = (1 - \alpha)u_n + \alpha|\mathbf{u}| \\ \xi_2 = (1 - \alpha)u_n - \alpha\sqrt{u_n^2 + u_\tau^2} = (1 - \alpha)u_n - \alpha|\mathbf{u}|, \end{cases} \tag{7}$$

and  $|\mathbf{u}|$  denotes the velocity magnitude. Note that  $\lambda_1, \lambda_2 < 0$ , and  $\lambda_3, \lambda_4 > 0$ . The following relations will be useful for subsequent discussions,

$$\begin{cases} 1 - \lambda_1^2 = -\xi_1\lambda_1, & 1 - \lambda_3^2 = -\xi_1\lambda_3; \\ 1 - \lambda_2^2 = -\xi_2\lambda_2, & 1 - \lambda_4^2 = -\xi_2\lambda_4. \end{cases} \tag{8}$$

If  $|\mathbf{u}| = 0$ , the contribution of the boundary term in (3) vanishes. So we assume that  $|\mathbf{u}| \neq 0$  in the following derivation of the boundary conditions.

The eigenvectors of **G** corresponding to the eigenvalues  $\xi_1$  and  $\xi_2$  have two representations, given by

$$\begin{cases} \begin{bmatrix} 1 \\ \eta \end{bmatrix}, \begin{bmatrix} -\eta \\ 1 \end{bmatrix}, & \text{if } u_n \geq 0; \\ \begin{bmatrix} \eta \\ 1 \end{bmatrix}, \begin{bmatrix} 1 \\ -\eta \end{bmatrix}, & \text{if } u_n < 0, \end{cases} \tag{9}$$

where

$$\eta = \frac{u_\tau}{|\mathbf{u}| + |u_n|}. \tag{10}$$

If  $u_\tau \neq 0$ , both representations of the eigenvectors are equivalent. But when  $u_\tau = 0$  only one of these two representations is suitable, depending on the sign of  $u_n$  as given above. Based on Theorem 2.1, the four eigenvectors of the matrix **A** are given by

$$\begin{bmatrix} 1 \\ \eta \\ -\lambda_1 \\ -\eta\lambda_1 \end{bmatrix}, \begin{bmatrix} -\eta \\ 1 \\ \eta\lambda_2 \\ -\lambda_2 \end{bmatrix}, \begin{bmatrix} 1 \\ \eta \\ -\lambda_3 \\ -\eta\lambda_3 \end{bmatrix}, \begin{bmatrix} -\eta \\ 1 \\ \eta\lambda_4 \\ -\lambda_4 \end{bmatrix}, \quad \text{if } u_n \geq 0, \tag{11}$$

and by

$$\begin{bmatrix} \eta \\ 1 \\ -\eta\lambda_1 \\ -\lambda_1 \end{bmatrix}, \begin{bmatrix} 1 \\ -\eta \\ -\lambda_2 \\ \eta\lambda_2 \end{bmatrix}, \begin{bmatrix} \eta \\ 1 \\ -\eta\lambda_3 \\ -\lambda_3 \end{bmatrix}, \begin{bmatrix} 1 \\ -\eta \\ -\lambda_4 \\ \eta\lambda_4 \end{bmatrix}, \quad \text{if } u_n < 0. \tag{12}$$

We use the four eigenvectors of **A** to form an orthogonal matrix  $\hat{\mathbf{P}}$ . For  $u_n \geq 0$ ,

$$\hat{\mathbf{P}} = \underbrace{\begin{bmatrix} 1 & -\eta & 1 & -\eta \\ \eta & 1 & \eta & 1 \\ -\lambda_1 & \eta\lambda_2 & -\lambda_3 & \eta\lambda_4 \\ -\eta\lambda_1 & -\lambda_2 & -\eta\lambda_3 & -\lambda_4 \end{bmatrix}}_{\mathbf{P}} \underbrace{\frac{1}{\sqrt{1 + \eta^2}} \text{diag} \left( \frac{1}{\sqrt{1 + \lambda_1^2}}, \dots, \frac{1}{\sqrt{1 + \lambda_4^2}} \right)}_{\mathbf{N}} = \mathbf{PN} \tag{13}$$

and for  $u_n < 0$ ,

$$\hat{\mathbf{P}} = \underbrace{\begin{bmatrix} \eta & 1 & \eta & 1 \\ 1 & -\eta & 1 & -\eta \\ -\eta\lambda_1 & -\lambda_2 & -\eta\lambda_3 & -\lambda_4 \\ -\lambda_1 & \eta\lambda_2 & -\lambda_3 & \eta\lambda_4 \end{bmatrix}}_{\mathbf{P}} \underbrace{\frac{1}{\sqrt{1 + \eta^2}} \text{diag} \left( \frac{1}{\sqrt{1 + \lambda_1^2}}, \dots, \frac{1}{\sqrt{1 + \lambda_4^2}} \right)}_{\mathbf{N}} = \mathbf{PN}. \tag{14}$$

Then the matrix  $\mathbf{A}$  in (5) can be written as

$$\mathbf{A} = \mathbf{P}\mathbf{N} \begin{bmatrix} \lambda_1 & & & \\ & \lambda_2 & & \\ & & \lambda_3 & \\ & & & \lambda_4 \end{bmatrix} \mathbf{N}^T \mathbf{P}^T = \mathbf{P}\mathbf{\Lambda}\mathbf{P}^T \tag{15}$$

where

$$\mathbf{\Lambda} = \begin{bmatrix} \mathbf{\Lambda}^- & \mathbf{0} \\ \mathbf{0} & \mathbf{\Lambda}^+ \end{bmatrix}, \quad \mathbf{\Lambda}^+ = \frac{1}{2(1+\eta^2)} \text{diag} \left( \frac{1}{\sqrt{(\xi_1/2)^2 + 1}}, \frac{1}{\sqrt{(\xi_2/2)^2 + 1}} \right), \quad \mathbf{\Lambda}^- = -\mathbf{\Lambda}^+, \tag{16}$$

and we have used the relations  $\lambda_1\lambda_3 = -1$  and  $\lambda_2\lambda_4 = -1$ .

The quadratic form in (5) is then transformed into

$$\begin{aligned} BT &= -\frac{1}{2} \mathbf{X}^T \mathbf{P}\mathbf{\Lambda}\mathbf{P}^T \mathbf{X} = -\frac{1}{2} \mathbf{W}^T \mathbf{\Lambda} \mathbf{W} = -\frac{1}{2} [(\mathbf{W}^-)^T \quad (\mathbf{W}^+)^T] \begin{bmatrix} \mathbf{\Lambda}^- & \mathbf{0} \\ \mathbf{0} & \mathbf{\Lambda}^+ \end{bmatrix} \begin{bmatrix} \mathbf{W}^- \\ \mathbf{W}^+ \end{bmatrix} \\ &= -\frac{1}{2} (\mathbf{W}^-)^T \mathbf{\Lambda}^- \mathbf{W}^- - \frac{1}{2} (\mathbf{W}^+)^T \mathbf{\Lambda}^+ \mathbf{W}^+ \end{aligned} \tag{17}$$

where

$$\mathbf{W} = \mathbf{P}^T \mathbf{X} = \begin{bmatrix} \mathbf{W}^- \\ \mathbf{W}^+ \end{bmatrix}. \tag{18}$$

Define the matrix formed by the eigenvectors of  $\mathbf{G}$  as

$$\mathbf{S} = \begin{cases} \begin{bmatrix} 1 & -\eta \\ \eta & 1 \end{bmatrix}, & \text{if } u_n \geq 0, \\ \begin{bmatrix} \eta & 1 \\ 1 & -\eta \end{bmatrix}, & \text{if } u_n < 0. \end{cases} \tag{19}$$

Then  $\mathbf{W}^-$  and  $\mathbf{W}^+$  are specifically given by

$$\begin{cases} \mathbf{W}^- = \mathbf{S}^T \begin{bmatrix} T_{nn} \\ T_{n\tau} \end{bmatrix} - \begin{bmatrix} \lambda_1 & \\ & \lambda_2 \end{bmatrix} \mathbf{S}^T \begin{bmatrix} u_n \\ u_\tau \end{bmatrix}, \\ \mathbf{W}^+ = \mathbf{S}^T \begin{bmatrix} T_{nn} \\ T_{n\tau} \end{bmatrix} - \begin{bmatrix} \lambda_3 & \\ & \lambda_4 \end{bmatrix} \mathbf{S}^T \begin{bmatrix} u_n \\ u_\tau \end{bmatrix}. \end{cases} \tag{20}$$

$\mathbf{W}^-$  and  $\mathbf{W}^+$  are the eigenvariables corresponding to the negative and the positive eigenvalues of matrix  $\mathbf{A}$ .

Following the strategy of [28], we consider boundary conditions of the form

$$\mathbf{W}^- = \mathbf{R}\mathbf{W}^+, \quad \text{with } \mathbf{R} = \begin{bmatrix} a_{11} & a_{12} \\ a_{21} & a_{22} \end{bmatrix} \tag{21}$$

where  $\mathbf{R}$  is a chosen constant matrix satisfying the conditions to be specified below. Substitute (21) into (17), and the quadratic form becomes

$$BT = -\frac{1}{2} (\mathbf{W}^+)^T \underbrace{(\mathbf{R}^T \mathbf{\Lambda}^- \mathbf{R} + \mathbf{\Lambda}^+)}_{\mathbf{Q}} \mathbf{W}^+ = -\frac{1}{2} (\mathbf{W}^+)^T \mathbf{Q} \mathbf{W}^+ \tag{22}$$

We require that the matrix  $\mathbf{R}$  be chosen such that matrix  $\mathbf{Q}$  as defined above is symmetric positive semi-definite (semi-SPD). As such, the boundary term in (3) will always be non-positive, and the energy stability of the system is guaranteed. Therefore, equation (21) represents a class of energy-stable boundary conditions.

Let us look into the semi-SPD requirement on  $\mathbf{Q}$  in more detail. Let

$$z_1 = \frac{1}{\sqrt{(\xi_1/2)^2 + 1}}, \quad z_2 = \frac{1}{\sqrt{(\xi_2/2)^2 + 1}}, \quad \mathbf{M} = \text{diag}(z_1, z_2). \tag{23}$$

In light of (16) and (22), we have  $\mathbf{Q} = \frac{1}{2(1+\eta^2)} (-\mathbf{R}^T \mathbf{M} \mathbf{R} + \mathbf{M})$ . Therefore we only need to find  $\mathbf{R}$  such that the matrix  $\mathbf{Q}_1 = \mathbf{M} - \mathbf{R}^T \mathbf{M} \mathbf{R}$  be symmetric positive semi-definite for all  $u_n \in (-\infty, \infty)$ ,  $u_\tau \in (-\infty, \infty)$ , and  $|\mathbf{u}| > 0$ . Requiring that the eigenvalues of  $\mathbf{Q}_1$  be non-negative is equivalent to the following conditions:

$$z_1(a_{11}^2 + a_{12}^2 - 1) + z_2(a_{21}^2 + a_{22}^2 - 1) \leq 0, \tag{24a}$$

$$-z_1^2 a_{12}^2 - z_2^2 a_{21}^2 + z_1 z_2 \left[ (a_{11} a_{22} - a_{12} a_{21})^2 + 1 - (a_{11}^2 + a_{22}^2) \right] \geq 0, \tag{24b}$$

for all  $u_n, u_\tau \in (-\infty, \infty)$  and  $|\mathbf{u}| > 0$ . Noting that  $z_1 \in (0, 1]$ ,  $z_2 \in (0, 1]$ , and  $\frac{z_2}{z_1} \in (0, \infty)$ , we conclude that

$$a_{12} = 0, \quad a_{21} = 0, \quad a_{11}^2 \leq 1, \quad a_{22}^2 \leq 1. \tag{25}$$

This is one set of conditions the matrix  $\mathbf{R}$  must satisfy.

Substituting the expressions of (20) into the boundary conditions (21) leads to

$$(\mathbf{I}_2 - \mathbf{R})\mathbf{S}^T \begin{bmatrix} T_{nm} \\ T_{n\tau} \end{bmatrix} = \left( -\mathbf{R} \begin{bmatrix} \lambda_3 & \\ & \lambda_4 \end{bmatrix} + \begin{bmatrix} \lambda_1 & \\ & \lambda_2 \end{bmatrix} \right) \mathbf{S}^T \begin{bmatrix} u_n \\ u_\tau \end{bmatrix}, \tag{26}$$

where  $\mathbf{I}_2$  is the identity matrix of dimension two. We require that  $(\mathbf{I}_2 - \mathbf{R})$  be non-singular, i.e.

$$a_{11} \neq 1, \quad a_{22} \neq 1. \tag{27}$$

This is another set of conditions for  $\mathbf{R}$ . Equation (26) is then transformed into

$$\begin{bmatrix} T_{nm} \\ T_{n\tau} \end{bmatrix} = \mathbf{S}^{-T} (\mathbf{I}_2 - \mathbf{R})^{-1} \left( -\mathbf{R} \begin{bmatrix} \lambda_3 & \\ & \lambda_4 \end{bmatrix} + \begin{bmatrix} \lambda_1 & \\ & \lambda_2 \end{bmatrix} \right) \mathbf{S}^T \begin{bmatrix} u_n \\ u_\tau \end{bmatrix} = \mathbf{S}^{-T} \begin{bmatrix} K_1 & \\ & K_2 \end{bmatrix} \mathbf{S}^T \begin{bmatrix} u_n \\ u_\tau \end{bmatrix}. \tag{28}$$

where

$$K_1 = \frac{\lambda_1 - a_{11}\lambda_3}{1 - a_{11}}, \quad K_2 = \frac{\lambda_2 - a_{22}\lambda_4}{1 - a_{22}}. \tag{29}$$

Substituting the expressions (19) for  $\mathbf{S}$  into (28), we get the boundary conditions in the following form. For  $u_n \geq 0$ ,

$$T_{nm} = \frac{K_1 + K_2\eta^2}{1 + \eta^2} u_n + \frac{\eta(K_1 - K_2)}{1 + \eta^2} u_\tau = f_1(u_n, u_\tau), \tag{30a}$$

$$T_{n\tau} = \frac{\eta(K_1 - K_2)}{1 + \eta^2} u_n + \frac{K_1\eta^2 + K_2}{1 + \eta^2} u_\tau = f_2(u_n, u_\tau). \tag{30b}$$

For  $u_n < 0$ ,

$$T_{nm} = \frac{K_1\eta^2 + K_2}{1 + \eta^2} u_n + \frac{\eta(K_1 - K_2)}{1 + \eta^2} u_\tau = f_1(u_n, u_\tau), \tag{31a}$$

$$T_{n\tau} = \frac{\eta(K_1 - K_2)}{1 + \eta^2} u_n + \frac{K_1 + K_2\eta^2}{1 + \eta^2} u_\tau = f_2(u_n, u_\tau). \tag{31b}$$

In the above equations  $K_1$  and  $K_2$  are given by (29),  $\eta$  is given by (10), and  $\lambda_i$  ( $1 \leq i \leq 4$ ) are given by (6).  $a_{11}$  and  $a_{22}$  are constant parameters satisfying the following conditions, in light of equations (25) and (27),

$$-1 \leq a_{11} < 1, \quad -1 \leq a_{22} < 1. \tag{32}$$

These boundary conditions ensure the energy stability of the system.

Let us next look into the boundary term (22) associated with these boundary conditions. The matrix  $\mathbf{Q}$  is reduced to  $\mathbf{Q} = \frac{1}{2(1+\eta^2)} \text{diag}(z_1(1 - a_{11}^2), z_2(1 - a_{22}^2))$  in light of equations (25) and (27). Let  $\mathbf{W}^+ = \begin{bmatrix} W_1 \\ W_2 \end{bmatrix}$ . Then we have, in light of equations (20) and (28),

$$\begin{bmatrix} W_1 \\ W_2 \end{bmatrix} = \mathbf{W}^+ = \begin{bmatrix} -\frac{2}{z_1(1-a_{11})} & \\ & -\frac{2}{z_2(1-a_{22})} \end{bmatrix} \mathbf{S}^T \begin{bmatrix} u_n \\ u_\tau \end{bmatrix}. \tag{33}$$

Substituting the above expression and the expression (19) into (22), we get

$$BT = \begin{cases} -\frac{1}{2} \left[ \frac{1+a_{11}}{1-a_{11}} \frac{2}{z_1(1+\eta^2)} (u_n + \eta u_\tau)^2 + \frac{1+a_{22}}{1-a_{22}} \frac{2}{z_2(1+\eta^2)} (-\eta u_n + u_\tau)^2 \right], & \text{if } u_n \geq 0, \\ -\frac{1}{2} \left[ \frac{1+a_{11}}{1-a_{11}} \frac{2}{z_1(1+\eta^2)} (\eta u_n + u_\tau)^2 + \frac{1+a_{22}}{1-a_{22}} \frac{2}{z_2(1+\eta^2)} (u_n - \eta u_\tau)^2 \right], & \text{if } u_n < 0. \end{cases} \tag{34}$$

According to this expression, for the boundary conditions given by (30a)–(31b), the amount of dissipation on the boundary is controlled by the parameters  $a_{11}$  and  $a_{22}$ . The larger  $a_{11}$  and  $a_{22}$  are, the more dissipative these boundary conditions are. If  $a_{11} = a_{22} = -1$ , the boundary dissipation vanishes completely. In other words, no energy can be convected through the boundary (into or out of domain) where these conditions are imposed. When  $a_{11} \rightarrow 1$  or  $a_{22} \rightarrow 1$ , the dissipation on the boundary will become infinitely large.

**Remark 1.** When deriving the boundary conditions (30a)–(31b), we have assumed that locally  $|\mathbf{u}| \neq 0$  on the boundary. These boundary conditions, however, can also accommodate the case when  $|\mathbf{u}| = 0$  locally on the boundary, if we modify the definition of  $\eta$  in (10) as follows to make it well defined for  $|\mathbf{u}| = 0$ ,

$$\eta = \frac{u_\tau}{|\mathbf{u}| + |u_n| + \epsilon}, \tag{35}$$

where  $\epsilon$  is a small positive number on the order of magnitude of the machine zero or smaller (e.g.  $\epsilon = 10^{-18}$ ). With this modified definition for  $\eta$ , when  $\mathbf{u} = 0$  locally at any point on the boundary, the boundary conditions are reduced to  $T_{nn} = T_{n\tau} = 0$ .

The boundary conditions (30a)–(31b) can be written into a vector form,

$$\begin{cases} \mathbf{n} \cdot \mathbf{T} = \mathbf{E}(\mathbf{u}, \partial\Omega), \text{ or} \\ -p\mathbf{n} + \nu\mathbf{n} \cdot \nabla\mathbf{u} - \mathbf{E}(\mathbf{u}, \partial\Omega) = \mathbf{0}, \end{cases} \tag{36}$$

where in two dimensions

$$\mathbf{E}(\mathbf{u}, \partial\Omega) = f_1(u_n, u_\tau)\mathbf{n} + f_2(u_n, u_\tau)\boldsymbol{\tau}, \tag{37}$$

and  $f_1, f_2$  are given in (30a)–(31b).

**Case  $\alpha = 0$ .** The matrix  $\mathbf{A}$  has two double eigenvalues,

$$\begin{cases} \lambda_1 = \lambda_2 = \frac{u_n}{2} - \sqrt{\left(\frac{u_n}{2}\right)^2 + 1}, \\ \lambda_3 = \lambda_4 = \frac{u_n}{2} + \sqrt{\left(\frac{u_n}{2}\right)^2 + 1}. \end{cases} \tag{38}$$

Note that they satisfy the relation  $u_n - \lambda_i = -\frac{1}{\lambda_i}$  ( $1 \leq i \leq 4$ ). The corresponding eigenvectors are

$$\begin{bmatrix} 1 \\ 0 \\ -\lambda_1 \\ 0 \end{bmatrix}, \begin{bmatrix} 0 \\ 1 \\ 0 \\ -\lambda_1 \end{bmatrix}, \begin{bmatrix} 1 \\ 0 \\ -\lambda_3 \\ 0 \end{bmatrix}, \begin{bmatrix} 0 \\ 1 \\ 0 \\ -\lambda_3 \end{bmatrix}. \tag{39}$$

Matrix  $\mathbf{A}$  can then be expressed as

$$\mathbf{A} = \mathbf{P}\boldsymbol{\Lambda}\mathbf{P}^T = \mathbf{P} \begin{bmatrix} \boldsymbol{\Lambda}^- & \\ & \boldsymbol{\Lambda}^+ \end{bmatrix} \mathbf{P}^T, \tag{40}$$

where

$$\mathbf{P} = \begin{bmatrix} 1 & 0 & 1 & 0 \\ 0 & 1 & 0 & 1 \\ -\lambda_1 & 0 & -\lambda_3 & 0 \\ 0 & -\lambda_1 & 0 & -\lambda_3 \end{bmatrix} = \begin{bmatrix} \mathbf{I}_2 & \mathbf{I}_2 \\ -\lambda_1\mathbf{I}_2 & -\lambda_3\mathbf{I}_2 \end{bmatrix}, \quad \boldsymbol{\Lambda}^- = -\boldsymbol{\Lambda}^+ = -\frac{1}{2\sqrt{(u_n/2)^2 + 1}}\mathbf{I}_2. \tag{41}$$

Accordingly, the boundary term in (5) is transformed into

$$\begin{aligned} BT &= -\frac{1}{2}\mathbf{X}^T\mathbf{P}\boldsymbol{\Lambda}\mathbf{P}^T\mathbf{X} = -\frac{1}{2}\mathbf{W}^T\boldsymbol{\Lambda}\mathbf{W} = -\frac{1}{2}\begin{bmatrix} \mathbf{W}^- \\ \mathbf{W}^+ \end{bmatrix}^T \begin{bmatrix} \boldsymbol{\Lambda}^- & 0 \\ & \boldsymbol{\Lambda}^+ \end{bmatrix} \begin{bmatrix} \mathbf{W}^- \\ \mathbf{W}^+ \end{bmatrix} \\ &= -\frac{1}{2}\left[(\mathbf{W}^-)^T\boldsymbol{\Lambda}^-\mathbf{W}^- + (\mathbf{W}^+)^T\boldsymbol{\Lambda}^+\mathbf{W}^+\right], \end{aligned} \tag{42}$$

where  $\mathbf{W} = \mathbf{P}^T\mathbf{X} = \begin{bmatrix} \mathbf{W}^- \\ \mathbf{W}^+ \end{bmatrix}$ .  $\mathbf{W}^-$  and  $\mathbf{W}^+$  are vectors of dimension two given specifically by

$$\begin{cases} \mathbf{W}^- = \begin{bmatrix} T_{nn} \\ T_{n\tau} \end{bmatrix} - \lambda_1 \begin{bmatrix} u_n \\ u_\tau \end{bmatrix}, \\ \mathbf{W}^+ = \begin{bmatrix} T_{nn} \\ T_{n\tau} \end{bmatrix} - \lambda_3 \begin{bmatrix} u_n \\ u_\tau \end{bmatrix}. \end{cases} \tag{43}$$

We again introduce boundary conditions in the form of equation (21), where the  $2 \times 2$  constant matrix  $\mathbf{R} = \begin{bmatrix} a_{11} & a_{12} \\ a_{21} & a_{22} \end{bmatrix}$  is to be determined. Therefore, the boundary term in (42) can be transformed into the same form as equation (22), in which the matrix

$$\mathbf{Q} = \mathbf{R}^T \mathbf{\Lambda}^{-} \mathbf{R} + \mathbf{\Lambda}^{+} = \frac{1}{2\sqrt{(u_n/2)^2 + 1}} (\mathbf{I}_2 - \mathbf{R}^T \mathbf{R}) \tag{44}$$

is required to be symmetric positive semi-definite. Requiring that the eigenvalues of  $\mathbf{Q}$  be non-negative leads to the following conditions:

$$a_{11}^2 + a_{12}^2 + a_{21}^2 + a_{22}^2 \leq 2, \text{ and} \tag{45a}$$

$$a_{11}^2 + a_{12}^2 + a_{21}^2 + a_{22}^2 \leq 1 + (a_{11}a_{22} - a_{12}a_{21})^2. \tag{45b}$$

A sufficient condition to guarantee both (45a) and (45b) is

$$a_{11}^2 + a_{12}^2 + a_{21}^2 + a_{22}^2 \leq 1. \tag{46}$$

This indicates that when  $a_{ij}$  ( $i, j = 1, 2$ ) are chosen to be sufficiently small the matrix  $\mathbf{R}$  will guarantee the positive semi-definiteness of the matrix  $\mathbf{Q}$  and the non-positivity of the surface integral term in (3).

In light of equation (43), the boundary condition in the form of equation (21) is transformed into

$$(\mathbf{I} - \mathbf{R}) \begin{bmatrix} T_{nn} \\ T_{n\tau} \end{bmatrix} = (\lambda_1 \mathbf{I} - \lambda_3 \mathbf{R}) \begin{bmatrix} u_n \\ u_\tau \end{bmatrix}. \tag{47}$$

We impose the requirement that  $(\mathbf{I} - \mathbf{R})$  be non-singular, i.e.

$$\mathcal{K} = \det(\mathbf{I} - \mathbf{R}) = (1 - a_{11})(1 - a_{22}) - a_{12}a_{21} \neq 0. \tag{48}$$

This is another condition the matrix  $\mathbf{R}$  must satisfy. Consequently, the boundary condition (47) becomes

$$\begin{bmatrix} T_{nn} \\ T_{n\tau} \end{bmatrix} = (\mathbf{I} - \mathbf{R})^{-1} (\lambda_1 \mathbf{I} - \lambda_3 \mathbf{R}) \begin{bmatrix} u_n \\ u_\tau \end{bmatrix}. \tag{49}$$

In component forms they are

$$T_{nn} = \frac{1}{\mathcal{K}} [(1 - a_{22})(\lambda_1 - \lambda_3 a_{11}) - \lambda_3 a_{12} a_{21}] u_n + \frac{1}{\mathcal{K}} (\lambda_1 - \lambda_3) a_{12} u_\tau = f_1(u_n, u_\tau), \tag{50a}$$

$$T_{n\tau} = \frac{1}{\mathcal{K}} (\lambda_1 - \lambda_3) a_{21} u_n + \frac{1}{\mathcal{K}} [(1 - a_{11})(\lambda_1 - \lambda_3 a_{22}) - \lambda_3 a_{12} a_{21}] u_\tau = f_2(u_n, u_\tau), \tag{50b}$$

where  $\mathcal{K}$  is given by (48),  $\lambda_1$  and  $\lambda_3$  are given by (38), and the chosen constants  $a_{ij}$  ( $i, j = 1, 2$ ) satisfy the conditions (45a), (45b) and (48). These are the energy-stable boundary conditions for the case  $\alpha = 0$ .

Let us now consider a simplified case:  $\mathbf{R}$  is assumed to be a diagonal matrix. The conditions (45a), (45b) and (48) are then reduced to

$$a_{12} = a_{21} = 0, \quad -1 \leq a_{11} < 1, \quad -1 \leq a_{22} < 1. \tag{51}$$

These are the same as those conditions for  $\mathbf{R}$  in the case  $0 < \alpha \leq \frac{1}{2}$ ; see equation (32). The boundary conditions (50a)–(50b) are reduced to

$$\begin{cases} T_{nn} = \frac{\lambda_1 - \lambda_3 a_{11}}{1 - a_{11}} u_n, \\ T_{n\tau} = \frac{\lambda_1 - \lambda_3 a_{22}}{1 - a_{22}} u_\tau. \end{cases} \tag{52}$$

With the above condition, the boundary term becomes

$$BT = -\frac{1}{2} \sqrt{u_n^2 + 4} \left( \frac{1 + a_{11}}{1 - a_{11}} u_n^2 + \frac{1 + a_{22}}{1 - a_{22}} u_\tau^2 \right). \tag{53}$$

For this simplified case, the amount of boundary dissipation is controlled by the constants  $a_{11}$  and  $a_{22}$ , and it is more dissipative with increasing  $a_{11}$  and  $a_{22}$ . It is noted that when  $a_{11} = a_{22} = -1$ ,  $BT = 0$ , and the boundary condition (52) is reduced to  $\mathbf{n} \cdot \mathbf{T} - \frac{1}{2} (\mathbf{n} \cdot \mathbf{u}) \mathbf{u} = 0$ .

The boundary conditions (50a)–(50b) can be cast into the same vectorial form as given by (36), in which  $\mathbf{E}(\mathbf{u}, \partial\Omega)$  is given by

$$\mathbf{E}(\mathbf{u}, \partial\Omega) = f_1(u_n, u_\tau) \mathbf{n} + f_2(u_n, u_\tau) \boldsymbol{\tau}, \tag{54}$$

where  $f_1(u_n, u_\tau)$  and  $f_2(u_n, u_\tau)$  are defined by (50a) and (50b).

2.2.2. Three dimensions (3D)

We next consider three dimensions in space. Let  $\mathbf{n}$  denote the outward-pointing unit vector normal to the boundary  $\partial\Omega$ , and  $\boldsymbol{\tau}$  and  $\mathbf{s}$  denote the unit vectors along the two independent directions tangent to  $\partial\Omega$ , such that  $(\mathbf{n}, \boldsymbol{\tau}, \mathbf{s})$  are mutually orthogonal and form a right-handed system. Define the three components along the  $(\mathbf{n}, \boldsymbol{\tau}, \mathbf{s})$  directions for the stress vector  $\mathbf{n} \cdot \mathbf{T}$  and the velocity  $\mathbf{u}$ ,

$$T_{nn} = \mathbf{n} \cdot \mathbf{T} \cdot \mathbf{n}, \quad T_{n\tau} = \mathbf{n} \cdot \mathbf{T} \cdot \boldsymbol{\tau}, \quad T_{ns} = \mathbf{n} \cdot \mathbf{T} \cdot \mathbf{s}, \quad u_n = \mathbf{n} \cdot \mathbf{u}, \quad u_\tau = \boldsymbol{\tau} \cdot \mathbf{u}, \quad u_s = \mathbf{s} \cdot \mathbf{u}. \tag{55}$$

In three dimensions the boundary term in the energy balance equation can be written as

$$BT = -\frac{1}{2} \begin{bmatrix} T_{nn} \\ T_{n\tau} \\ T_{ns} \\ u_n \\ u_\tau \\ u_s \end{bmatrix}^T \underbrace{\begin{bmatrix} 0 & 0 & 0 & -1 & 0 & 0 \\ 0 & 0 & 0 & 0 & -1 & 0 \\ 0 & 0 & 0 & 0 & 0 & -1 \\ -1 & 0 & 0 & u_n & \alpha_1 u_\tau & \alpha_2 u_s \\ 0 & -1 & 0 & \alpha_1 u_\tau & \beta_1 u_n & 0 \\ 0 & 0 & -1 & \alpha_2 u_s & 0 & \beta_2 u_n \end{bmatrix}}_{\text{matrix } \mathbf{A}} \underbrace{\begin{bmatrix} T_{nn} \\ T_{n\tau} \\ T_{ns} \\ u_n \\ u_\tau \\ u_s \end{bmatrix}}_{\mathbf{x}} = -\frac{1}{2} \mathbf{x}^T \mathbf{A} \mathbf{x}, \tag{56}$$

where  $\alpha_1$  and  $\alpha_2$  are chosen constants satisfying  $0 \leq \alpha_1 \leq \frac{1}{2}$  and  $0 \leq \alpha_2 \leq \frac{1}{2}$ , and  $\beta_1 = 1 - 2\alpha_1$  and  $\beta_2 = 1 - 2\alpha_2$ . The

matrix  $\mathbf{A}$  has the form as discussed in Theorem 2.1, and  $\mathbf{G} = \begin{bmatrix} u_n & \alpha_1 u_\tau & \alpha_2 u_s \\ \alpha_1 u_\tau & \beta_1 u_n & 0 \\ \alpha_2 u_s & 0 & \beta_2 u_n \end{bmatrix}$ .

Let  $\xi_1, \xi_2$  and  $\xi_3$  denote the three (real) eigenvalues of  $\mathbf{G}$ , and  $\mathbf{Z}_1, \mathbf{Z}_2$  and  $\mathbf{Z}_3$  denote the corresponding orthonormal eigenvectors, and  $\mathbf{S} = [\mathbf{Z}_1 \ \mathbf{Z}_2 \ \mathbf{Z}_3]$  denote the orthogonal matrix formed by these eigenvectors. According to Theorem 2.1, the eigenvalues of  $\mathbf{A}$  are

$$\begin{cases} \lambda_1 = \frac{\xi_1}{2} - \sqrt{\left(\frac{\xi_1}{2}\right)^2 + 1}, & \lambda_2 = \frac{\xi_2}{2} - \sqrt{\left(\frac{\xi_2}{2}\right)^2 + 1}, & \lambda_3 = \frac{\xi_3}{2} - \sqrt{\left(\frac{\xi_3}{2}\right)^2 + 1}, \\ \lambda_4 = \frac{\xi_1}{2} + \sqrt{\left(\frac{\xi_1}{2}\right)^2 + 1}, & \lambda_5 = \frac{\xi_2}{2} + \sqrt{\left(\frac{\xi_2}{2}\right)^2 + 1}, & \lambda_6 = \frac{\xi_3}{2} + \sqrt{\left(\frac{\xi_3}{2}\right)^2 + 1}. \end{cases} \tag{57}$$

The corresponding eigenvectors are given by

$$\begin{bmatrix} \mathbf{Z}_1 \\ -\lambda_1 \mathbf{Z}_1 \end{bmatrix}, \quad \begin{bmatrix} \mathbf{Z}_2 \\ -\lambda_2 \mathbf{Z}_2 \end{bmatrix}, \quad \begin{bmatrix} \mathbf{Z}_3 \\ -\lambda_3 \mathbf{Z}_3 \end{bmatrix}, \quad \begin{bmatrix} \mathbf{Z}_1 \\ -\lambda_4 \mathbf{Z}_1 \end{bmatrix}, \quad \begin{bmatrix} \mathbf{Z}_2 \\ -\lambda_5 \mathbf{Z}_2 \end{bmatrix}, \quad \begin{bmatrix} \mathbf{Z}_3 \\ -\lambda_6 \mathbf{Z}_3 \end{bmatrix}. \tag{58}$$

Let  $\mathbf{C}_1 = \text{diag}(\lambda_1, \lambda_2, \lambda_3)$ ,  $\mathbf{C}_2 = \text{diag}(\lambda_4, \lambda_5, \lambda_6)$ , and  $\mathbf{P} = \begin{bmatrix} \mathbf{S} & \mathbf{S} \\ -\mathbf{S}\mathbf{C}_1 & -\mathbf{S}\mathbf{C}_2 \end{bmatrix}$ . Then matrix  $\mathbf{A}$  can be represented as

$$\mathbf{A} = \mathbf{P} \begin{bmatrix} \frac{\lambda_1}{1+\lambda_1^2} & & \\ & \ddots & \\ & & \frac{\lambda_6}{1+\lambda_6^2} \end{bmatrix} \mathbf{P}^T = \mathbf{P} \mathbf{\Lambda} \mathbf{P}^T = \mathbf{P} \begin{bmatrix} \mathbf{\Lambda}^- & \mathbf{0} \\ \mathbf{0} & \mathbf{\Lambda}^+ \end{bmatrix} \mathbf{P}^T, \tag{59}$$

where  $\mathbf{\Lambda}^- = -\mathbf{\Lambda}^+ = -\text{diag}\left(\frac{1}{2\sqrt{(\xi_1/2)^2+1}}, \frac{1}{2\sqrt{(\xi_2/2)^2+1}}, \frac{1}{2\sqrt{(\xi_3/2)^2+1}}\right)$ . Let

$$\begin{bmatrix} \mathbf{W}^- \\ \mathbf{W}^+ \end{bmatrix} = \mathbf{W} = \mathbf{P}^T \mathbf{x} = \begin{bmatrix} \mathbf{S}^T & -\mathbf{C}_1 \mathbf{S}^T \\ \mathbf{S}^T & -\mathbf{C}_2 \mathbf{S}^T \end{bmatrix} \begin{bmatrix} \mathbf{T}_n \\ \mathbf{U} \end{bmatrix} = \begin{bmatrix} \mathbf{S}^T \mathbf{T}_n - \mathbf{C}_1 \mathbf{S}^T \mathbf{U} \\ \mathbf{S}^T \mathbf{T}_n - \mathbf{C}_2 \mathbf{S}^T \mathbf{U} \end{bmatrix}, \tag{60}$$

where  $\mathbf{T}_n = \begin{bmatrix} T_{nn} \\ T_{n\tau} \\ T_{ns} \end{bmatrix}$  and  $\mathbf{U} = \begin{bmatrix} u_n \\ u_\tau \\ u_s \end{bmatrix}$ . Analogous to 2D, we consider boundary conditions of the form  $\mathbf{W}^- = \mathbf{R} \mathbf{W}^+$ , where  $\mathbf{R}$  is a chosen  $3 \times 3$  constant matrix. The boundary term (56) is then transformed into

$$\begin{aligned} BT &= -\frac{1}{2} \left[ (\mathbf{W}^-)^T \mathbf{\Lambda}^- \mathbf{W}^- + (\mathbf{W}^+)^T \mathbf{\Lambda}^+ \mathbf{W}^+ \right] = -\frac{1}{2} (\mathbf{W}^+)^T \underbrace{\left[ \mathbf{R}^T \mathbf{\Lambda}^- \mathbf{R} + \mathbf{\Lambda}^+ \right]}_{\mathbf{Q}} \mathbf{W}^+ \\ &= -\frac{1}{2} (\mathbf{W}^+)^T \mathbf{Q} \mathbf{W}^+. \end{aligned} \tag{61}$$

We then require that  $\mathbf{R}$  be chosen such that the symmetric matrix  $\mathbf{Q} = \mathbf{R}^T \mathbf{\Lambda}^- \mathbf{R} + \mathbf{\Lambda}^+$  is positive semi-definite to ensure the non-positivity of the boundary term.

Since the closed form for  $\xi_i$  ( $i = 1, 2, 3$ ) is unknown, it is difficult to determine the general form for the matrix  $\mathbf{R}$  that ensures the positive semi-definiteness of  $\mathbf{Q}$ . In the current work we consider only the following special case for three dimensions: We assume that  $\mathbf{R}$  is a diagonal matrix, i.e.  $\mathbf{R} = \text{diag}(a_{11}, a_{22}, a_{33})$ . With this assumption, the requirement that  $\mathbf{Q}$  be symmetric positive semi-definite leads to the conditions

$$a_{11}^2 \leq 1, \quad a_{22}^2 \leq 1, \quad a_{33}^2 \leq 1. \tag{62}$$

Substitution of the expressions for  $\mathbf{W}^-$  and  $\mathbf{W}^+$  in (60) into the boundary condition leads to

$$(\mathbf{I}_3 - \mathbf{R})\mathbf{S}^T \mathbf{T}_n = (\mathbf{C}_1 - \mathbf{R}\mathbf{C}_2)\mathbf{S}^T \mathbf{U}. \tag{63}$$

We further require that  $(\mathbf{I}_3 - \mathbf{R})$  be non-singular. With this and the condition (62), we get

$$\mathbf{R} = \text{diag}(a_{11}, a_{22}, a_{33}), \text{ where } -1 \leq a_{11}, a_{22}, a_{33} < 1. \tag{64}$$

With this  $\mathbf{R}$  matrix the boundary condition (63) becomes

$$\mathbf{T}_n = \mathbf{S}(\mathbf{I}_3 - \mathbf{R})^{-1}(\mathbf{C}_1 - \mathbf{R}\mathbf{C}_2)\mathbf{S}^T \mathbf{U} = \mathbf{S} \begin{bmatrix} \frac{\lambda_1 - \lambda_4 a_{11}}{1 - a_{11}} & & \\ & \frac{\lambda_2 - \lambda_5 a_{22}}{1 - a_{22}} & \\ & & \frac{\lambda_3 - \lambda_6 a_{33}}{1 - a_{33}} \end{bmatrix} \mathbf{S}^T \mathbf{U}. \tag{65}$$

Equivalently, it can be written as

$$\begin{bmatrix} T_{nn} \\ T_{n\tau} \\ T_{ns} \end{bmatrix} = \mathbf{L} \begin{bmatrix} u_n \\ u_\tau \\ u_s \end{bmatrix} = \begin{bmatrix} L_{11}u_n + L_{12}u_\tau + L_{13}u_s \\ L_{21}u_n + L_{22}u_\tau + L_{23}u_s \\ L_{31}u_n + L_{32}u_\tau + L_{33}u_s \end{bmatrix} = \begin{bmatrix} g_1(u_n, u_\tau, u_s) \\ g_2(u_n, u_\tau, u_s) \\ g_3(u_n, u_\tau, u_s) \end{bmatrix} \tag{66}$$

where

$$\begin{bmatrix} L_{11} & L_{22} & L_{33} \\ L_{21} & L_{22} & L_{23} \\ L_{31} & L_{32} & L_{33} \end{bmatrix} = \mathbf{L} = \mathbf{S} \begin{bmatrix} \frac{\lambda_1 - \lambda_4 a_{11}}{1 - a_{11}} & & \\ & \frac{\lambda_2 - \lambda_5 a_{22}}{1 - a_{22}} & \\ & & \frac{\lambda_3 - \lambda_6 a_{33}}{1 - a_{33}} \end{bmatrix} \mathbf{S}^T. \tag{67}$$

In vector form, this boundary condition is the same as given by (36), but here in 3D  $\mathbf{E}(\mathbf{u}, \partial\Omega)$  is given by

$$\mathbf{E}(\mathbf{u}, \partial\Omega) = g_1(u_n, u_\tau, u_s)\mathbf{n} + g_2(u_n, u_\tau, u_s)\boldsymbol{\tau} + g_3(u_n, u_\tau, u_s)\mathbf{s}, \tag{68}$$

where  $g_1, g_2$  and  $g_3$  are defined by (66). The boundary term (61) is accordingly transformed into

$$BT = -\frac{1}{2}(\mathbf{S}^T \mathbf{U})^T \begin{bmatrix} \frac{2(1+a_{11})\sqrt{(\xi_1/2)^2+1}}{1-a_{11}} & & \\ & \frac{2(1+a_{22})\sqrt{(\xi_2/2)^2+1}}{1-a_{22}} & \\ & & \frac{2(1+a_{33})\sqrt{(\xi_3/2)^2+1}}{1-a_{33}} \end{bmatrix} (\mathbf{S}^T \mathbf{U}). \tag{69}$$

This expression indicates that the dissipativeness of the boundary condition (66) is controlled by the coefficients  $a_{ii}$  ( $i = 1, 2, 3$ ). The larger the  $a_{ii}$ , the more dissipative the boundary condition. If  $a_{11} = a_{22} = a_{33} = -1$ , the boundary dissipation vanishes. When  $a_{ii} \rightarrow 1$  ( $i = 1, 2, 3$ ), the boundary dissipation approaches infinity. It is further noted that if  $\alpha_1 = \alpha_2 = 0$  and  $a_{11} = a_{22} = a_{33} = -1$  the 3D boundary condition (66) will be reduced to  $\mathbf{n} \cdot \mathbf{T} - \frac{1}{2}(\mathbf{n} \cdot \mathbf{u})\mathbf{u} = 0$ .

In summary,  $\mathbf{E}(\mathbf{u}, \partial\Omega)$  in the 3D boundary condition is computed as follows. Given domain boundary  $\partial\Omega$  (with normal and tangent vectors  $\mathbf{n}, \boldsymbol{\tau}, \mathbf{s}$ ), the velocity  $\mathbf{u}$  on  $\partial\Omega$ , the chosen constants  $a_{ii}$  ( $i = 1, 2, 3$ ),  $\alpha_1$  and  $\alpha_2$ , we take the following steps:

- Compute  $u_n, u_\tau, u_s$  based on equation (55).
- Form matrix  $\mathbf{G}$ . Compute its eigenvalues  $\xi_i$  ( $i = 1, 2, 3$ ) and eigenvectors. Use the eigenvectors to form the orthogonal matrix  $\mathbf{S}$ .
- Compute  $\lambda_i$  ( $i = 1, \dots, 6$ ) by equation (57). Compute matrix  $\mathbf{L}$  by equation (67).
- Compute  $g_1, g_2, g_3$  according to equation (66),

$$\begin{cases} g_1(u_n, u_\tau, u_s) = L_{11}u_n + L_{12}u_\tau + L_{13}u_s, \\ g_2(u_n, u_\tau, u_s) = L_{21}u_n + L_{22}u_\tau + L_{23}u_s, \\ g_3(u_n, u_\tau, u_s) = L_{31}u_n + L_{32}u_\tau + L_{33}u_s. \end{cases} \tag{70}$$

- Form  $\mathbf{E}(\mathbf{u}, \partial\Omega)$  based on equation (68).

2.3. Open/outflow boundary conditions for incompressible flows

The class of boundary conditions obtained in the previous section ensures that the boundary contribution in the energy balance equation will not cause the system energy to increase over time. We next apply these boundary conditions to specifically deal with outflow or open boundaries.

We assume that two types of boundaries (which are non-overlapping) are present:  $\partial\Omega = \partial\Omega_d \cup \partial\Omega_o$ .  $\partial\Omega_d$  is the Dirichlet type boundary, on which the velocity is given,

$$\mathbf{u} = \mathbf{w}(\mathbf{x}, t), \quad \text{on } \partial\Omega_d, \tag{71}$$

where  $\mathbf{w}$  is the boundary velocity. On the open/outflow boundary  $\partial\Omega_o$  none of the flow variables is known.

On the outflow/open boundary  $\partial\Omega_o$  we impose the family of boundary conditions from Section 2.2,

$$-p\mathbf{n} + \nu\mathbf{n} \cdot \nabla\mathbf{u} - \mathbf{E}(\mathbf{u}, \partial\Omega_o) = 0, \quad \text{on } \partial\Omega_o, \tag{72}$$

where

$$\mathbf{E}(\mathbf{u}, \partial\Omega_o) = \begin{cases} f_1(u_n, u_\tau)\mathbf{n} + f_2(u_n, u_\tau)\boldsymbol{\tau}, & \text{in 2D,} \\ g_1(u_n, u_\tau, u_s)\mathbf{n} + g_2(u_n, u_\tau, u_s)\boldsymbol{\tau} + g_3(u_n, u_\tau, u_s)\mathbf{s}, & \text{in 3D.} \end{cases} \tag{73}$$

In the above expressions  $f_1$  and  $f_2$  are given by (30a)–(31b) or (50a)–(50b), and  $g_i$  ( $i = 1, 2, 3$ ) are given by (70). In 2D,  $(\mathbf{n}, \boldsymbol{\tau})$  are the local unit vectors normal and tangent to  $\partial\Omega_o$ , and  $(u_n, u_\tau)$  are the local velocity components in these directions. In 3D,  $(\mathbf{n}, \boldsymbol{\tau}, \mathbf{s})$  are the local unit vectors normal to  $\partial\Omega_o$  and along the two tangent directions of  $\partial\Omega_o$ , and  $(u_n, u_\tau, u_s)$  are the local velocity components in these directions.

The dissipation on the boundary, upon imposing the condition (72), is determined by the coefficients  $\frac{1+a_{ii}}{1-a_{ii}}$  ( $i = 1, 2, 3$ ). When  $a_{ii} \rightarrow -1$  the boundary dissipation vanishes, and when  $a_{ii} \rightarrow 1$  the boundary dissipation becomes infinite. Both cases are obviously unphysical, even though they may be energy stable. So we expect the physical accuracy of simulation results will be poor for these cases. Indeed, numerical experiments suggest that the best results correspond to  $a_{ii}$  somewhat negative and not too far from zero.

If no backflow occurs on the open boundary  $\partial\Omega_o$ , an often-used boundary condition is the traction free condition, i.e.  $\mathbf{n} \cdot \mathbf{T} = -p\mathbf{n} + \nu\mathbf{n} \cdot \nabla\mathbf{u} = 0$ , which produces reasonable simulation results but is unstable if backflow occurs at moderate and high Reynolds numbers. With the traction-free condition, the boundary term in (3) becomes  $BT = -\frac{1}{2}(\mathbf{n} \cdot \mathbf{u})|\mathbf{u}|^2$ , which physically means that the kinetic energy is convected out of the domain by the normal velocity (when  $u_n > 0$ ). This suggests that a reasonable scale for the magnitude of dissipation on the open boundary  $\partial\Omega_o$  is comparable to

$$|BT| = \frac{1}{2}|u_n||\mathbf{u}|^2. \tag{74}$$

For further development it is important to realize another point. The conditions for the  $\mathbf{R}$  matrix that ensure the energy dissipation on the boundary derived in the previous section are based on the local point-wise values of the flow fields on each individual point of the boundary. Energy stability is guaranteed as long as the coefficient  $a_{ii}$  satisfies the conditions given in Section 2.2 for an  $\alpha$  coefficient (or the coefficients  $\alpha_1$  and  $\alpha_2$  in 3D) on each individual point of the boundary  $\partial\Omega_o$ . On different points of the boundary and over time, however,  $a_{ii}$  and  $\alpha$  do not have to assume the same value. In other words, the coefficients can be e.g. prescribed field distributions  $a_{ii}(\mathbf{x}, t)$  and  $\alpha(\mathbf{x}, t)$  (or  $\alpha_1(\mathbf{x}, t)$  and  $\alpha_2(\mathbf{x}, t)$  in 3D), as long as they satisfy the conditions from Section 2.2 on each point of  $\partial\Omega_o$  at all time.

In light of the above observations, with the boundary conditions (72) and (73) we will consider two configurations for  $a_{ii}$  ( $i = 1, 2, 3$  for 3D and  $i = 1, 2$  for 2D) and  $\alpha$ :

- $a_{ii}$  and  $\alpha$  (or in 3D,  $\alpha_1$  and  $\alpha_2$ ) are uniform constants on the entire boundary  $\partial\Omega_o$  and over time, which satisfy the conditions from Section 2.2.
- $a_{ii}$  and  $\alpha$  (or in 3D,  $\alpha_1$  and  $\alpha_2$ ) may be field distributions, which (i) satisfy the conditions from Section 2.2 for energy stability and further (ii) are such that the magnitude of boundary dissipation on  $\partial\Omega_o$  satisfies equation (74).

These two configurations lead to two different sets of open boundary conditions.

Let us look into the second set of boundary conditions in more detail. There are many means to choose  $a_{ii}$  and  $\alpha$  to satisfy (74). We specifically consider two ways below. In the first, we note that in the 3D equation (69)  $\mathbf{S}$  is an orthogonal matrix and  $(\mathbf{S}^T \mathbf{U})^T (\mathbf{S}^T \mathbf{U}) = \mathbf{U}^T \mathbf{U} = |\mathbf{u}|^2$ . Therefore the boundary term (69) reduces to (74) if

$$\frac{1+a_{ii}}{1-a_{ii}} 2\sqrt{\left(\frac{\xi_i}{2}\right)^2 + 1} = |u_n|, \quad \text{or} \quad a_{ii} = -\frac{\sqrt{\xi_i^2 + 4} - |u_n|}{\sqrt{\xi_i^2 + 4} + |u_n|}, \tag{75}$$

for  $i = 1, 2, 3$ , where  $\xi_i$  ( $i = 1, 2, 3$ ) are the eigenvalues of the matrix  $\mathbf{G}$  and depends on  $\alpha_1$  and  $\alpha_2$ . Similarly, for 2D the boundary terms in equations (34) and (53) will reduce to the form given by equation (74) if  $a_{ii}$  are given by the same

expression as in (75) for  $i = 1, 2$ , noting that  $\xi_i$  ( $i = 1, 2$ ) are now the eigenvalues of the matrix  $\mathbf{G}$  in 2D and depend on  $\alpha$ . Substitution of the  $a_{ii}$  expression (75) into equations (30a)–(31b) and also equations (70) results in greatly simplified expressions for  $f_i$  ( $i = 1, 2$ ) and  $g_i$  ( $i = 1, 2, 3$ ) in equation (73), as given below,

$$(2D) \begin{cases} f_1(u_n, u_\tau) = \frac{1}{2} [(u_n - |u_n|)u_n + \alpha u_\tau^2], \\ f_2(u_n, u_\tau) = \frac{1}{2} u_\tau [(1 - \alpha)u_n - |u_n|]; \end{cases} \tag{76}$$

$$(3D) \begin{cases} g_1(u_n, u_\tau, u_s) = \frac{1}{2} [(u_n - |u_n|)u_n + \alpha_1 u_\tau^2 + \alpha_2 u_s^2], \\ g_2(u_n, u_\tau, u_s) = \frac{1}{2} u_\tau [(1 - \alpha_1)u_n - |u_n|], \\ g_3(u_n, u_\tau, u_s) = \frac{1}{2} u_s [(1 - \alpha_2)u_n - |u_n|]. \end{cases} \tag{77}$$

We fix the  $\alpha$  coefficient in 2D (or  $\alpha_1, \alpha_2$  in 3D) as follows. In 2D we will determine  $\alpha$  to try to make  $a_{ii}$  as large as possible. This requirement is based on the following observation: Numerical simulations with  $a_{ii}$  and  $\alpha$  as uniform constants suggest that larger  $a_{ii}$  values ( $-1 \leq a_{ii} < 1$ ) appear to be able to reduce the lateral meandering or distortion of the vortex street as the vortices cross the open boundary. In light of the expression (75), we will find  $\alpha$  such that the  $\min(|\xi_1|, |\xi_2|)$  is minimized and that  $\alpha$  is well defined for all  $|\mathbf{u}| > 0$ . Substituting the  $\xi_1$  and  $\xi_2$  expressions in (7) into this condition, we get

$$\alpha = \frac{|u_n|}{|\mathbf{u}| + |u_n| + \epsilon}, \quad (\text{for 2D}) \tag{78}$$

where  $\epsilon$  is a small positive number on the order of machine zero or smaller (e.g.  $\epsilon \sim 10^{-18}$ ) to make the above expression well-defined even if  $|\mathbf{u}| = 0$ . Note that this expression satisfies  $0 \leq \alpha \leq \frac{1}{2}$ . For three dimensions, the closed form for  $\xi_i$  ( $i = 1, 2, 3$ ) as a function of  $\alpha_1$  and  $\alpha_2$  is unknown, and the coefficients  $\alpha_1$  and  $\alpha_2$  cannot be determined as such. Inspired by the 2D result of (78), we will employ this same expression for  $\alpha_1$  and  $\alpha_2$  in 3D in this work, that is,

$$\alpha_1 = \alpha_2 = \frac{|u_n|}{|\mathbf{u}| + |u_n| + \epsilon}, \quad (\text{for 3D}). \tag{79}$$

The boundary condition (72), with  $E(\mathbf{n}, \partial\Omega_o)$  given by (73) and  $f_i$  and  $g_i$  given by (76) and (77), in which  $\alpha$  is given by (78) and  $\alpha_1$  and  $\alpha_2$  are given by (79), is energy stable and the magnitude of boundary dissipation on  $\partial\Omega_o$  satisfies equation (74).

As a second way to satisfy equation (74), we assume that all  $a_{ii}$  ( $i = 1, 2, 3$ ) are identical. In 3D, let  $\begin{bmatrix} V_1 \\ V_2 \\ V_3 \end{bmatrix} = \mathbf{S}^T \mathbf{U} = \mathbf{S}^T \begin{bmatrix} u_n \\ u_\tau \\ u_s \end{bmatrix}$  and  $Y_i = 2\sqrt{(\xi_i/2)^2 + 1}$  ( $i = 1, 2, 3$ ). Substitution of the boundary term (69) into equation (74) results in

$$a_{11} = a_{22} = a_{33} = \frac{J_t - 1}{J_t + 1}, \quad \text{where } J_t = \frac{|u_n||\mathbf{u}|^2}{(Y_1 V_1^2 + Y_2 V_2^2 + Y_3 V_3^2) + \epsilon}. \tag{80}$$

In the above equation  $\epsilon$  is a small positive number on the order of machine zero or smaller to make the  $J_t$  expression well defined when  $|\mathbf{u}| = 0$ . In 2D, let  $\begin{bmatrix} V_1 \\ V_2 \end{bmatrix} = \frac{1}{\sqrt{1+\eta^2}} \mathbf{S}^T \begin{bmatrix} u_n \\ u_\tau \end{bmatrix}$  and  $Y_i = 2\sqrt{(\xi_i/2)^2 + 1}$  ( $i = 1, 2$ ), where the matrix  $\mathbf{S}$  is given by (19). Then the coefficients  $a_{ii}$  are given by

$$a_{11} = a_{22} = \frac{J_t - 1}{J_t + 1}, \quad \text{where } J_t = \frac{|u_n||\mathbf{u}|^2}{(Y_1 V_1^2 + Y_2 V_2^2) + \epsilon}. \tag{81}$$

In 2D we again determine  $\alpha$  to try to make  $a_{ii}$  (or equivalently  $J_t$ ) as large as possible. Note that  $|\mathbf{u}|^2 = V_1^2 + V_2^2$  in 2D, and (omitting the  $\epsilon$ )  $J_t = \frac{|u_n|}{Y_1 \frac{V_1^2}{V_1^2+V_2^2} + Y_2 \frac{V_2^2}{V_1^2+V_2^2}} \leq \frac{|u_n|}{\min(Y_1, Y_2)}$ . We minimize  $\min(Y_1, Y_2)$ , or equivalently  $\min(|\xi_1|, |\xi_2|)$ , and obtain

again the expression (78) for  $\alpha$ . For 3D we will again employ the expressions in (79) for  $\alpha_1$  and  $\alpha_2$ . The boundary condition (72) with  $\mathbf{E}(\mathbf{u}, \partial\Omega_o)$  given by (73), in which  $a_{ii}$  is given by (81) or (80) and  $\alpha$  (or  $\alpha_1$  and  $\alpha_2$ ) are given by (78) or (79), is another energy-stable open boundary condition whose boundary dissipation satisfies equation (74).

**Remark 2.** One can multiply the  $\mathbf{E}(\mathbf{n}, \partial\Omega_o)$  expression in (73) by the smoothed step function introduced in [12,14] to approximately enforce the requirement that the magnitude of boundary dissipation should be comparable to that given by (74). The modified  $\mathbf{E}(\mathbf{n}, \partial\Omega_o)$  is given by

$$\mathbf{E}(\mathbf{u}, \partial\Omega_o) = \begin{cases} [f_1(u_n, u_\tau)\mathbf{n} + f_2(u_n, u_\tau)\boldsymbol{\tau}] \Theta(\mathbf{n}, \mathbf{u}), & \text{in 2D,} \\ [g_1(u_n, u_\tau, u_s)\mathbf{n} + g_2(u_n, u_\tau, u_s)\boldsymbol{\tau} + g_3(u_n, u_\tau, u_s)\mathbf{s}] \Theta(\mathbf{n}, \mathbf{u}), & \text{in 3D,} \end{cases} \quad (82)$$

where  $\Theta(\mathbf{n}, \mathbf{u})$  is a smoothed step function given by (see [14])

$$\Theta(\mathbf{n}, \mathbf{u}) = \frac{1}{2} \left( 1 - \tanh \frac{\mathbf{n} \cdot \mathbf{u}}{U_0 \delta} \right), \quad \text{and} \quad \lim_{\delta \rightarrow 0} \Theta(\mathbf{n}, \mathbf{u}) = \Theta_0(\mathbf{n}, \mathbf{u}) = \begin{cases} 1, & \text{if } \mathbf{n} \cdot \mathbf{u} < 0, \\ 0, & \text{otherwise.} \end{cases} \quad (83)$$

In the above expression,  $U_0$  is the velocity scale, and  $\delta > 0$  is a small positive constant that controls the sharpness of the smoothed step function. As  $\delta \rightarrow 0$ ,  $\Theta(\mathbf{n}, \mathbf{u})$  approaches the unit step function  $\Theta_0(\mathbf{n}, \mathbf{u})$ . This modified  $\mathbf{E}(\mathbf{u}, \partial\Omega_o)$  enforces the following requirement: (i) if locally no backflow occurs on  $\partial\Omega_o$  (i.e.  $u_n \geq 0$ ), then the boundary condition (72) should reduce to the traction-free condition; (ii) if backflow occurs locally on  $\partial\Omega_o$  (i.e.  $u_n < 0$ ), then the condition (72) shall reduce to the form with  $\mathbf{E}(\mathbf{u}, \partial\Omega_o)$  given by equation (73).

In the current work, we will concentrate on three open boundary conditions (referred to as OBC-A, OBC-B and OBC-C, respectively) corresponding to the two configurations for  $a_{ii}$  as discussed above. More specifically, we concentrate on the OBC (72) with  $\mathbf{E}(\mathbf{u}, \partial\Omega_o)$  given by (73), in which  $f_i$  ( $i = 1, 2$ ) and  $g_i$  ( $i = 1, 2, 3$ ) take three different forms (see Appendix B for a summary of them):

(OBC-A)  $f_i$  ( $i = 1, 2$ ) are given by (30a)–(31b) or (50a)–(50b) and  $g_i$  ( $i = 1, 2, 3$ ) are given by (70), in which  $a_{ii}$  and  $\alpha$  (or  $\alpha_1$  and  $\alpha_2$ ) are uniform constants on the entire  $\partial\Omega_o$ .

(OBC-B)  $f_i$  ( $i = 1, 2$ ) are given by equation (76), in which  $\alpha$  is given by (78), and  $g_i$  ( $i = 1, 2, 3$ ) are given by equation (77), in which  $\alpha_1$  and  $\alpha_2$  are given by (79).

(OBC-C)  $f_i$  ( $i = 1, 2$ ) are given by (30a)–(31b) and  $g_i$  ( $i = 1, 2, 3$ ) are given by (70), in which  $a_{ii}$  are given by (81) for 2D and (80) for 3D, and  $\alpha$  is given by (78) and  $\alpha_1$  and  $\alpha_2$  are given by (79).

With OBC-A the dissipation on the open boundary depends on the constants  $a_{ii}$  and the flow field at  $\partial\Omega_o$ . It is anticipated that the parameters  $a_{ii}$  will influence the accuracy of simulation results, and that certain  $a_{ii}$  values may lead to poor results (e.g.  $a_{ii}$  close to 1 and  $-1$ ). It is also likely that the best values for  $a_{ii}$  with OBC-A will be flow-problem dependent. These points will indeed be observed and confirmed from the numerical experiments in Section 3. With OBC-B and OBC-C, on the other hand, the dissipation on  $\partial\Omega_o$  matches the scale given by equation (74). We anticipate that OBC-B and OBC-C will lead to more accurate simulation results. This will indeed be demonstrated by the numerical simulations in Section 3.

Let us finally discuss how to implement the class of open boundary conditions represented by (72). The equations (1a)–(1b), supplemented by the boundary conditions (71)–(72) and the initial condition (2), constitute the system to be solved for in numerical simulations. This system of equations and boundary conditions are similar in form to those considered in our previous works [14,10]. Therefore one can employ the algorithms developed in [14] or [10] to numerically solve the current system. In this work, we employ the scheme from [10] (presented in Section 2.4 of [10]) to simulate the system consisting of (1a)–(1b), (71)–(72) and (2). This is a velocity-correction type splitting scheme, in which the computations for the pressure and the velocity are de-coupled. For the sake of completeness, we have provided a summary of this algorithm in Appendix C, in which some details on the implementation of these boundary conditions are given. In the 2D implementation, the spatial discretization is performed using a high-order spectral element method [33,24,39]. In the 3D implementation, we restrict our attention to flow domains with at least one homogeneous direction (designated as  $z$  direction), while in the other two directions the domain can be arbitrarily complex. Therefore for spatial discretizations we employ a Fourier spectral expansion of the field variables along the homogeneous  $z$  direction, and a spectral element expansion within the non-homogeneous  $x$ - $y$  planes. We refer to e.g. [11,13,8] for more detailed discussions of the hybrid discretization of Navier-Stokes equations with Fourier spectral and spectral-element methods. All three boundary conditions, OBC-A, OBC-B and OBC-C, have been implemented in 2D, and in 3D only OBC-B and OBC-C are implemented.

### 3. Representative numerical examples

We next present numerical simulations for several representative flow problems in two and three dimensions to test the performance of the energy-stable OBCs developed in Section 2. All these problems involve open/outflow boundaries, and the OBCs are critical to the stability at moderate and high Reynolds numbers.

#### 3.1. Convergence rates

We first use a manufactured analytic solution to the incompressible Navier-Stokes equations on a domain with open boundaries to test the spatial and temporal convergence rates of our method together with the energy-stable OBCs from Section 2.

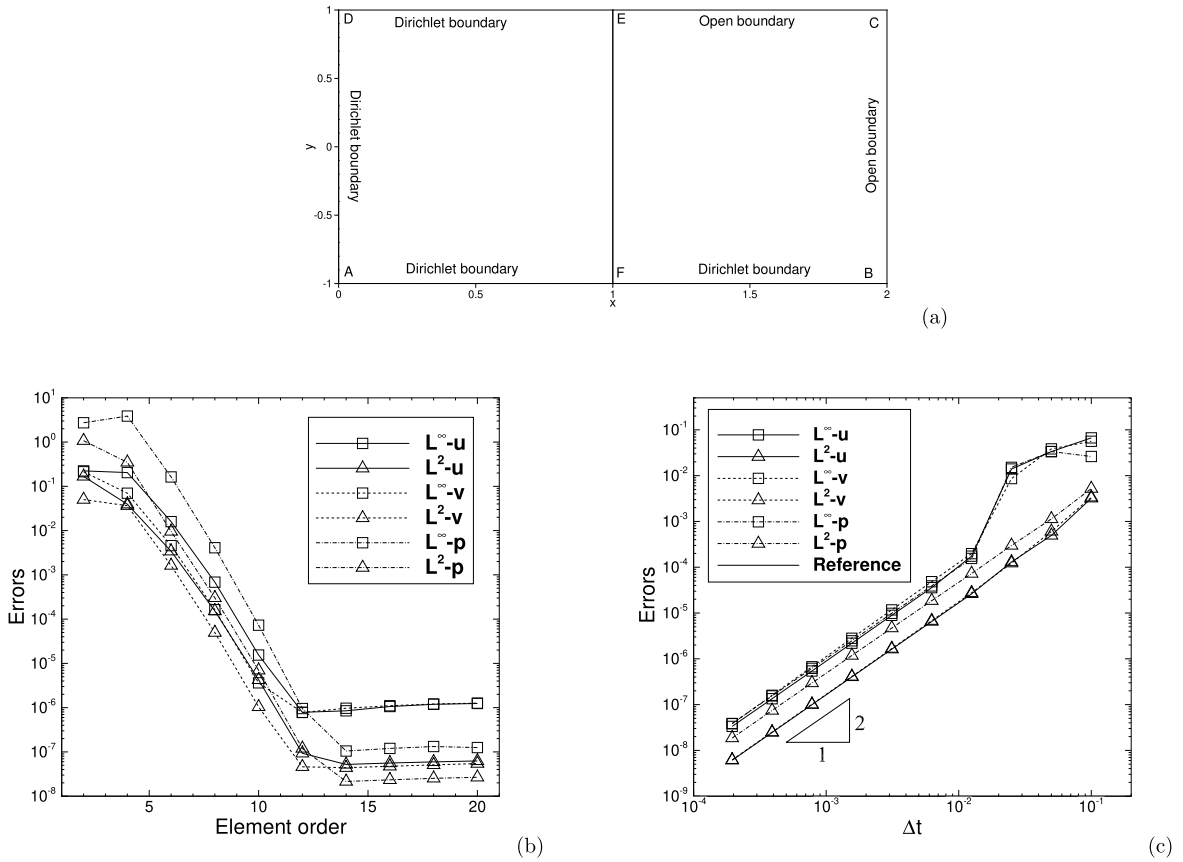


**Fig. 1.** Convergence tests (2D): (a) Mesh and configuration.  $L^\infty$  and  $L^2$  errors of the flow variables as a function of the element order with fixed  $t_f = 0.1$  and  $\Delta t = 0.001$  (b), and of the time step size  $\Delta t$  with fixed element order 16 and  $t_f = 0.5$  (c). OBC-C has been used on the open boundaries.

**Two dimensions (2D)** We consider the 2D rectangular domain  $\overline{ABCD}$  shown in Fig. 1(a),  $0 \leq x \leq 2$  and  $-1 \leq y \leq 1$ , and the following analytic solution to the incompressible Navier-Stokes equations,

$$\begin{cases} u = 2 \cos(\pi y) \sin(\pi x) \sin t \\ v = -2 \sin(\pi y) \cos(\pi x) \sin t \\ p = 2 \sin(\pi y) \sin(\pi x) \cos t \end{cases} \quad (84)$$

where  $\mathbf{u} = (u, v)$ . The external force  $\mathbf{f}$  in (1a) is chosen such that the expressions in (84) satisfy (1a).

The domain is discretized using two uniform quadrilateral spectral elements ( $AFED$  and  $FBCE$ ) as shown in Fig. 1(a). On the boundaries  $\overline{AB}$ ,  $\overline{AD}$  and  $\overline{DE}$  Dirichlet boundary condition (71) is imposed, in which the boundary velocity  $\mathbf{w}(\mathbf{x}, t)$  is set according to the analytic expressions from (84). On the boundaries  $\overline{BC}$  and  $\overline{CE}$  the OBC (113) (in Appendix C) is imposed, in which  $\mathbf{f}_b$  is chosen such that the analytic expressions from (84) satisfy the equation (113) on  $\partial\Omega_o$ . The initial condition is given by (2), in which the initial velocity  $\mathbf{u}_{in}$  is obtained according to the analytic solution in (84) by setting  $t = 0$ .

The Navier-Stokes equations together with the OBCs from Section 2.3 are solved using the numerical algorithm given in Appendix C. The velocity/pressure fields are computed from  $t = 0$  to  $t = t_f$  ( $t_f$  specified below). Then the flow variables at  $t = t_f$  from numerical simulations are compared with the analytic solutions in (84), and the errors in various norms are computed. The element order and the time step size  $\Delta t$  are varied systematically to study their effects on the errors in spatial and temporal convergence tests, respectively. The non-dimensional viscosity in (1a) is fixed at  $\nu = 0.01$  in the following tests.

Fig. 1(b) demonstrates the results for the 2D spatial convergence tests. Here we have employed a fixed  $t_f = 0.1$  and  $\Delta t = 0.001$  (i.e. 100 time steps). The element order is varied systematically between 2 and 20, and for each element order we compute the errors of the numerical solution at  $t = t_f$  against the analytic solution. Fig. 1(b) shows the numerical errors of the velocity and pressure in  $L^\infty$  and  $L^2$  norms as a function of the element order from these tests, in which OBC-C is used on the open boundaries. The errors decrease exponentially with increasing element order as the order is below 12. For orders 12 and beyond, a saturation of the errors is observed at a level  $10^{-7} \sim 10^{-6}$  due to the temporal truncation errors.

Fig. 1(c) demonstrates the results for the 2D temporal convergence tests. Here we have employed a fixed  $t_f = 0.5$  and element order 16. The time step size  $\Delta t$  is varied systematically between  $\Delta t = 0.1$  and  $\Delta t = 1.953125e - 4$ . Fig. 1(c) shows

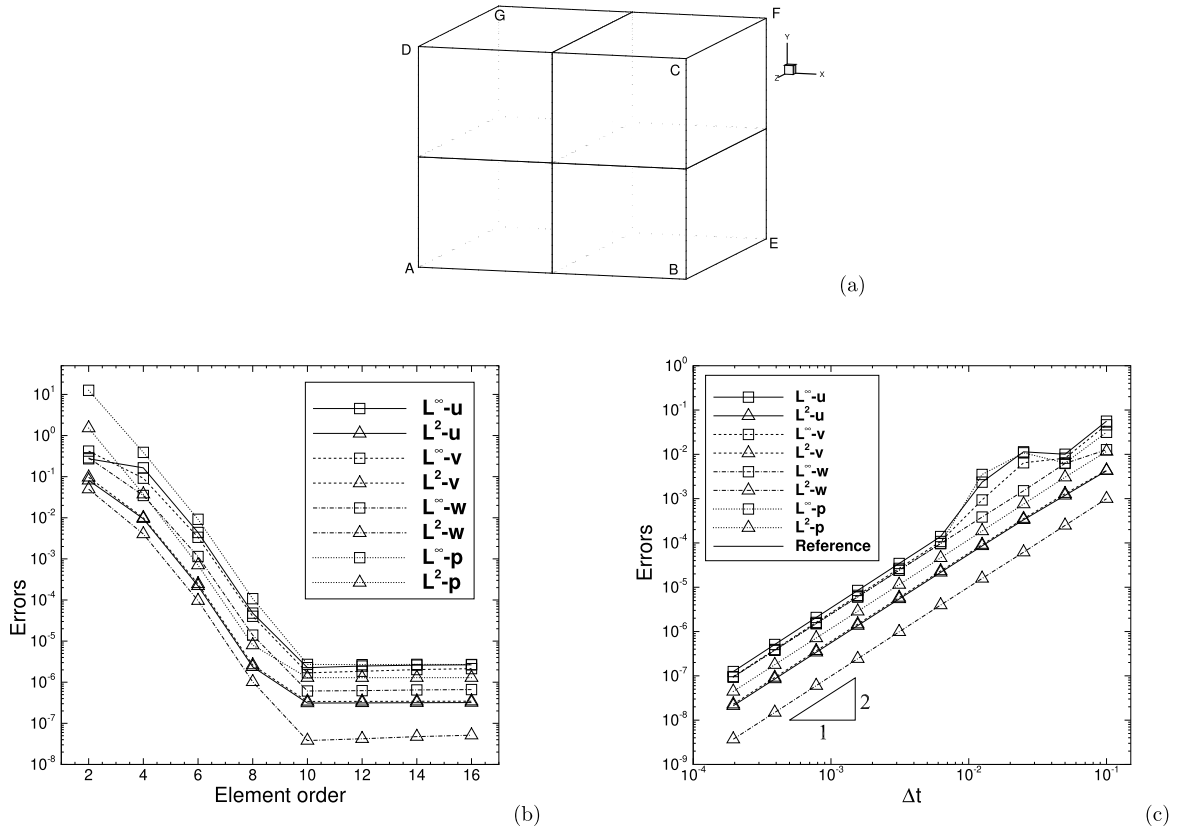


**Fig. 2.** Convergence tests (3D): (a) mesh of four hexahedral elements.  $L^\infty$  and  $L^2$  errors of the flow variables as a function of element order with fixed  $t_f = 0.1$  and  $\Delta t = 0.001$  (b), and of  $\Delta t$  with fixed element order 12 and  $t_f = 0.2$  (c). OBC-B is used on the open boundaries  $DCFG$  and  $BEFC$ .

the  $L^\infty$  and  $L^2$  errors of the flow variables at  $t = t_f$  as a function of  $\Delta t$  in this group of tests. The open boundary condition is again OBC-C in these tests. The rate of convergence with respect to  $\Delta t$  is observed to be second order when  $\Delta t$  is sufficiently small.

**Three dimensions (3D)** We consider the 3D domain as sketched in Fig. 2(a),  $0.25 \leq x \leq 1.25$ ,  $-1 \leq y \leq 1$ , and  $0 \leq z \leq 2$ , and the following analytic solutions to the Navier-Stokes equations,

$$\begin{cases} u = 2 \cos(2\pi x) \cos(\pi y) \cos(\pi z) \sin t, & v = 2 \sin(2\pi x) \sin(\pi y) \cos(\pi z) \sin t, \\ w = 2 \sin(2\pi x) \cos(\pi y) \sin(\pi z) \sin t, & p = 2 \sin(2\pi x) \sin(\pi y) \sin(\pi z) \cos t, \end{cases} \quad (85)$$

where  $\mathbf{u} = (u, v, w)$  in 3D. The external force  $\mathbf{f}$  is chosen such that the analytic expressions in (85) satisfy the equation (1a). We assume that the domain and the flow variables are periodic in  $z$  direction (on faces  $z = 0$  and  $z = 2$ ). The faces  $BEFC$  and  $DCFG$  are open boundaries and the rest are Dirichlet boundaries.

As discussed in Section 2.3, we employ a hybrid Fourier spectral method and spectral element method to discretize the 3D domain. Fourier spectral expansions are employed along the homogeneous  $z$  direction, and spectral element expansions are employed in the  $x$ - $y$  planes. In the numerical tests that follow four Fourier planes are employed in  $z$  direction, and four quadrilateral elements are employed to discretize each plane. The boundary conditions (71) and (113) are imposed on the Dirichlet and open boundaries, in which the boundary velocity  $\mathbf{w}$  is set in accordance with the analytic expressions (85) and the function  $\mathbf{f}_b$  is chosen such that the analytic solutions in (85) satisfy (113) on the open boundaries. The algorithm from the Appendix C is employed in the simulations. The flow fields are obtained from  $t = 0$  to  $t = t_f$ , and the errors of the numerical solution at  $t = t_f$  are computed against the analytic solution given in (85). The non-dimensional viscosity is  $\nu = 0.01$  in the following tests.

In the spatial convergence tests, we use a fixed  $t_f = 0.1$  and  $\Delta t = 0.001$ , and vary the element order systematically between 2 and 16. Fig. 2(b) shows the numerical errors of the velocity and pressure at  $t = t_f$  as a function of the element order, obtained using OBC-B for the open boundaries. An exponential decrease in the numerical errors can be observed when the element order is below 10, and a saturation in the numerical errors is observed for element orders beyond 10 due to the temporal truncation error.

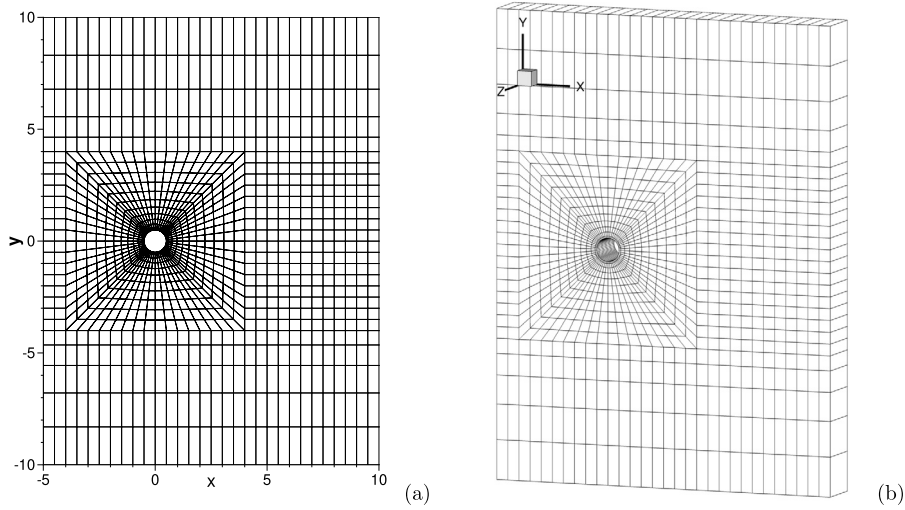


**Fig. 3.** Flow past a circular cylinder: spectral element meshes in (a) 2D, and (b) 3D. The 2D mesh and each x-y plane of the 3D mesh contains 1228 quadrilateral elements.

In the temporal convergence tests we use a fixed  $t_f = 0.2$  and element order 12, and vary  $\Delta t$  systematically between  $\Delta t = 0.1$  and  $\Delta t = 1.953125e - 4$ . We have computed the numerical errors at  $t = t_f$  corresponding to each  $\Delta t$  with OBC-B as the open boundary condition, and in Fig. 2(c) these errors are plotted as a function of  $\Delta t$  (in logarithmic scales). The results signify a second-order convergence rate in time.

To summarize, the 2D and 3D results of this section demonstrate that, with the OBCs herein, our method exhibits a spatial exponential convergence rate and a temporal second-order accuracy for incompressible flows on domains with open/outflow boundaries.

### 3.2. Flow past a circular cylinder

We focus on a canonical wake flow, the flow past a circular cylinder, in 2D and 3D in this section. At moderate/high Reynolds numbers, how to handle the outflow boundary in this flow is critical to the stability of simulations. We employ this canonical problem to test the OBCs developed in the current work.

#### 3.2.1. Two-dimensional simulations

Let us first investigate the cylinder flow numerically in 2D. Consider the domain in Fig. 3(a),  $-5 \leq x/d \leq 10$  and  $-10 \leq y/d \leq 10$ , where  $d$  is the cylinder diameter. The center of the cylinder coincides with the origin of the coordinate system. The top and bottom of the domain ( $y = \pm 10d$ ) are assumed to be periodic. A uniform flow (free-stream velocity  $U_0$ , along the  $x$  direction) enters the domain from the left side, and the wake exits the domain through the right boundary at  $x = 10d$ . We assume no external force is present, and thus  $\mathbf{f} = 0$  in equation (1a). All the length variables are normalized based on the cylinder diameter  $d$ , and all the velocity variables are normalized by the free stream velocity  $U_0$ . So the Reynolds number is defined based on  $U_0$  and  $d$ . All the other variables are normalized accordingly in a consistent way.

We discretize the domain using the spectral element mesh shown in Fig. 3(a), which contains 1228 quadrilateral elements. The algorithm from the Appendix C is used for the simulations. On the cylinder surface no-slip condition is imposed, i.e. the Dirichlet boundary condition (71) with  $\mathbf{w} = 0$ . At the inlet ( $x/d = -5$ ) we impose the Dirichlet condition (71) where the boundary velocity  $\mathbf{w}$  is set based on the free-stream velocity. Periodic conditions are imposed at the top and bottom of the domain. At the outflow boundary ( $x/d = 10$ ) the boundary condition (72) from Section 2.3 is imposed, where OBC-A, OBC-B and OBC-C are all employed and the various algorithmic parameters have been tested.

Fig. 4 illustrates a long-time 2D simulation at Reynolds number  $Re = 100$  with a window of time histories of the forces (drag  $f_x$ , and lift  $f_y$ ) acting on the cylinder. The results are obtained using an element order 8 and OBC-B as the outflow boundary condition. Periodic vortex shedding into the wake induces a fluctuating drag and lift force exerting on the cylinder. Based on these histories we can compute the statistical quantities such as the time-averaged mean and root-mean-square (rms) forces. Table 1 lists the mean and rms forces on the cylinder at Reynolds numbers  $Re = 30$  and 100 obtained using several element orders ranging from 4 to 10. The mean lift is not shown in the table because they are all zeros at  $Re = 30$  and all essentially zeros at  $Re = 100$ . The flow is in a steady state at  $Re = 30$ , and so no averaging is performed at this Reynolds number. When the element order is sufficiently large (6 or above), the forces obtained from the simulations are essentially the same, suggesting convergence with respect to the grid resolution. The majority of subsequent simulations are performed using an element order 8 and  $\Delta t = 2.5e - 4$ , and at lower Reynolds numbers (below  $Re = 60$ ) an element order

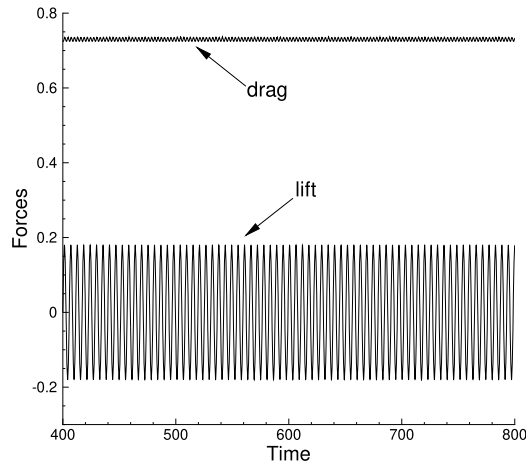
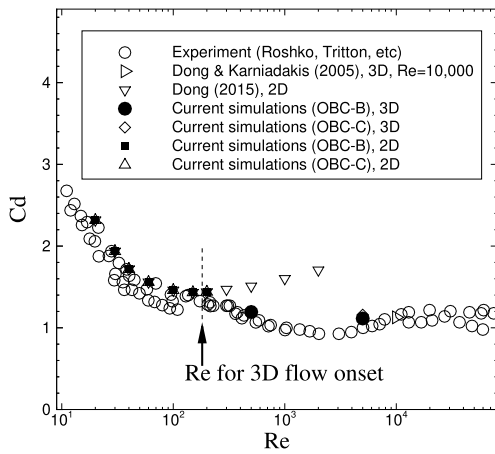


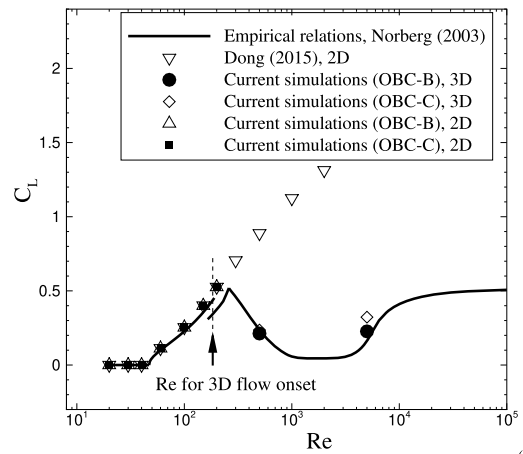
Fig. 4. Time histories of drag ( $x$  component of force,  $f_x$ ) and lift ( $y$  component of force,  $f_y$ ) on the cylinder at  $Re = 100$ , computed using an element order 8 and OBC-B as the outflow boundary condition in 2D.

**Table 1**  
Flow past a cylinder (2D): forces on the cylinder computed using several element orders. OBC-B is used for the outflow boundary condition.

$Re$	Element order	Mean- $f_x$	rms- $f_x$	rms- $f_y$
30	4	0.968	0	0
	6	0.968	0	0
	8	0.968	0	0
	10	0.968	0	0
100	4	0.729	0.00374	0.126
	6	0.730	0.00377	0.127
	8	0.730	0.00377	0.127
	10	0.730	0.00377	0.127



(a)



(b)

Fig. 5. Flow past a cylinder: Comparison of the drag coefficient (a) and the rms lift coefficient (b) as a function of the Reynolds number between current simulations (2D/3D) and the experimental measurements. OBC-B and OBC-C are used as the outflow boundary condition with current simulations.

6 and  $\Delta t = 1e - 3$  have also been employed. A range of Reynolds numbers (to be specified below) has been simulated and studied for this problem.

We first study this flow for a range of low Reynolds numbers ( $Re = 200$  and below). The physical flow is two-dimensional and is either at a steady state (for  $Re \lesssim 45$ ) or unsteady with periodic vortex shedding (for  $Re \lesssim 185$ ) [37]. We have conducted simulations at several Reynolds numbers in this range, and computed the corresponding forces on the cylinder. Figs. 5(a) and (b) are comparisons of the drag coefficients ( $C_d$ ) and rms lift coefficients ( $C_L$ ) obtained from current simulations with those from the experimental measurements and simulations from the literature [36,17,34,31,27,13,10]. These

**Table 2**

2D cylinder flow: comparison of the mean and rms forces on the cylinder obtained using OBC-A (with  $\alpha = 1/2$  and various parameters  $a_{11} = a_{22}$ ), OBC-B, and OBC-C for several Reynolds numbers. Results from the traction-free open boundary condition are included as a reference.

<i>Re</i>	Method	Parameters	Mean- $f_x$	rms- $f_x$	rms- $f_y$
10	OBC-A	$a_{11} = a_{22} = 0.95$	1.652	0	0
		0.9	1.652	0	0
		0.5	1.648	0	0
		0.2	1.644	0	0
		0.1	1.641	0	0
		0.0	1.639	0	0
		-0.1	1.635	0	0
		-0.2	1.630	0	0
		-0.5	1.593	0	0
		-0.9	1.445	0	0
		-0.95	1.427	0	0
		OBC-B	1.631	0	0
		OBC-C	1.631	0	0
Traction-free OBC	1.631	0	0		
20	OBC-A	$a_{11} = a_{22} = 0.95$	1.173	0	0
		0.9	1.173	0	0
		0.5	1.171	0	0
		0.2	1.168	0	0
		0.1	1.166	0	0
		0.0	1.164	0	0
		-0.1	1.162	0	0
		-0.2	1.158	0	0
		-0.5	1.121	0	0
		-0.9	0.967	0	0
		-0.95	0.952	0	0
		OBC-B	1.159	0	0
		OBC-C	1.159	0	0
Traction-free OBC	1.159	0	0		
100	OBC-A	$a_{11} = a_{22} = 0.95$	0.734	0.00412	0.128
		0.9	0.734	0.00412	0.127
		0.5	0.732	0.00392	0.125
		0.2	0.731	0.00378	0.126
		0.1	0.731	0.00377	0.126
		0.0	0.731	0.00377	0.126
		-0.1	0.730	0.00378	0.127
		-0.2	0.730	0.00382	0.127
		-0.5	0.723	0.00425	0.131
		-0.9	(unstable)		
		-0.95	(unstable)		
		OBC-B	0.730	0.00377	0.127
		OBC-C	0.730	0.00378	0.127
Traction-free OBC	0.729	0.00381	0.127		

coefficients are defined by  $C_d = \frac{\bar{f}_x}{\frac{1}{2}\rho_f U_0^2}$  and  $C_L = \frac{f'_y}{\frac{1}{2}\rho_f U_0^2}$ , where  $\bar{f}_x$  denotes the time-averaged (mean) drag,  $f'_y$  denotes the rms-lift on the cylinder, and  $\rho_f$  is the fluid density. Note that the plots also include results from the three-dimensional simulations, which will be discussed subsequently in Section 3.2.2. The current 2D results are obtained using the OBC-B and OBC-C as the outflow boundary conditions. We observe that in this range of Reynolds numbers the current 2D results are in good agreement with the experimental data, and they also agree well with the results from [10]. When the Reynolds number is beyond this range (above  $Re \approx 185 \sim 260$ ), the physical flow will undergo a transition and become three-dimensional [37]. So there will be a large discrepancy between the drag/lift coefficients from 2D simulations and the experimentally observed values [11,14,10].

At these low Reynolds numbers it is relatively easy to carry out a study of how the algorithmic parameters affect the simulation results. OBC-A, OBC-B and OBC-C have all been employed and tested with the open boundary condition (72) in current simulations.

Let us first focus on OBC-A. In Table 2 we list the (time-averaged) mean and rms forces on the cylinder at three Reynolds numbers ( $Re = 10, 20$  and  $100$ ), obtained using OBC-A as the outflow boundary condition under a range of values for  $a_{11}$  (and  $a_{22}$ , with  $a_{22} = a_{11}$ ) and with a fixed  $\alpha = \frac{1}{2}$ . Since the flow is steady at  $Re = 10$  and  $20$ , no time-averaging is performed for these two Reynolds numbers. As a reference, we have also included results computed using the traction-free condition on the outflow boundary, namely,

$$-p\mathbf{n} + \nu\mathbf{n} \cdot \nabla\mathbf{u} = 0, \quad \text{on } \partial\Omega_o. \tag{86}$$

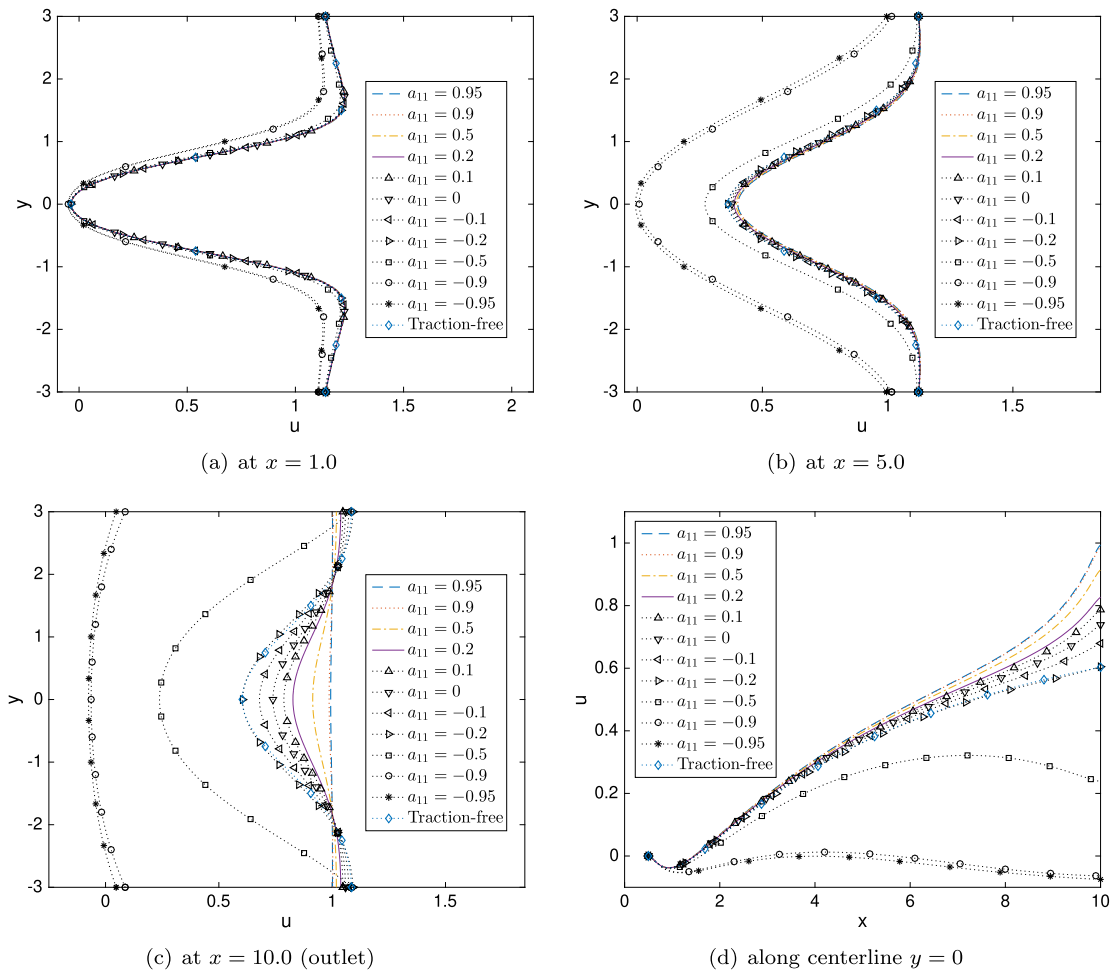


**Fig. 6.** Cylinder flow ( $Re = 20$ ): comparison of streamwise velocity (i.e.  $x$  velocity component) profiles at several downstream locations and along the centerline computed using OBC-A with  $\alpha = 1/2$  and different  $a_{11}$  (and  $a_{22}$ , with  $a_{22} = a_{11}$ ) values. Results from traction-free condition are included for comparison. (For interpretation of the colors in the figure(s), the reader is referred to the web version of this article.)

A trend can be discerned from the data obtained using OBC-A. The mean drag computed using OBC-A tends to decrease with decreasing  $a_{11}$  (and  $a_{22}$ ) values. When compared with the results based on the traction-free condition, the best results with OBC-A seem to correspond to a value around  $a_{11} = a_{22} \approx -0.2$  for the cylinder flow. In an interval around this best value, the computed forces seem to be not sensitive to  $a_{11}$  ( $a_{22}$ ) and they are very close to the forces corresponding to the traction-free condition. Even when  $a_{11} = a_{22} = 0.95$ , the discrepancy in the mean drag seems to be around 1%. But as  $a_{11} = a_{22} \rightarrow -1$ , the discrepancy in the mean drag seems to grow rapidly and becomes very substantial. For example, with  $a_{11} = a_{22} = -0.95$  the difference in the mean drag values produced by OBC-A and the traction-free condition is approximately 18% at  $Re = 20$ . In addition, we observe that at  $Re = 100$ , with  $a_{11} = a_{22} = -0.9$  and smaller, the computation with OBC-A is unstable. We recall that as  $a_{11} = a_{22} \rightarrow 1$  the amount of dissipation on  $\partial\Omega_0$  with OBC-A becomes infinite, and as  $a_{11} = a_{22} \rightarrow -1$  the amount of dissipation approaches zero. The above results with the computed forces suggest that, while the best  $a_{11}$  ( $a_{22}$ ) values seem to be around  $-0.2$ , larger values appear not harmful, but it can be detrimental to the accuracy if  $a_{11}$  ( $a_{22}$ ) is too small.

The velocity distribution in the cylinder wake demonstrates the effects of  $a_{11}$  (and  $a_{22}$ ) on the simulation results even more clearly. Fig. 6 is a comparison of the steady-state streamwise velocity ( $x$  velocity) profiles along the vertical direction at downstream locations  $x/d = 1.0$ ,  $5.0$  and  $10.0$  (plots (a), (b) and (c)), and along the centerline (plot (d)). The different curves correspond to OBC-A with  $\alpha = \frac{1}{2}$  and a set of  $a_{11}$  (and  $a_{22}$ , with  $a_{22} = a_{11}$ ) values ranging from  $-0.95$  to  $0.95$ . For comparison, the velocity profiles computed using the traction-free condition (86) are also included. We have the following observations:

- The velocity profiles corresponding to OBC-A with  $a_{11} = a_{22} = -0.5$  and below exhibit a large discrepancy when compared with the rest of the profiles in essentially the entire wake region.

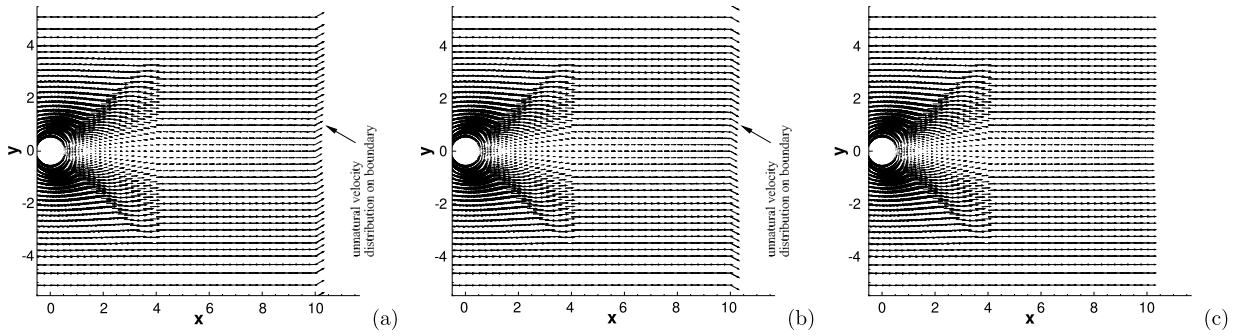


**Fig. 7.** 2D Cylinder flow ( $Re = 20$ ): velocity fields computed using OBC-A ( $\alpha = 0, a_{11} = a_{22} = a_{12} = 0$ ) with different  $a_{21}$  values: (a)  $a_{21} = -0.4$ , (b)  $a_{21} = 0.4$ , and (c)  $a_{21} = 0$ . Un-physical velocity distributions can be observed at the outflow boundary if  $a_{21} \neq 0$  with OBC-A. Velocity vectors are plotted on every eighth quadrature points in each direction within each element.

- The profiles corresponding to OBC-A with  $a_{11} = a_{22} = -0.2$  and above are quite close to those resulting from the traction-free boundary condition (86) in the near wake ( $x/d \lesssim 5$ ). Further downstream ( $x/d \gtrsim 6$ ) the discrepancy in all the profiles (except the one with  $a_{11} = a_{22} = -0.2$ ), when compared with the traction-free condition, becomes very pronounced.
- Among the set of  $a_{11}$  ( $a_{22}$ ) values tested for OBC-A, the best profile corresponds to  $a_{11} = a_{22} = -0.2$ , in terms of the comparison with results based on the traction-free condition.

In the above the effects of  $a_{11}$  and  $a_{22}$  in OBC-A on the simulation results are investigated with a fixed  $\alpha = \frac{1}{2}$ . Studies of the  $a_{11}$  ( $a_{22}$ ) effect with other  $\alpha$  values are also performed, but not as systematically. The above observed behaviors of OBC-A with respect to  $a_{11}$  and  $a_{22}$  appear to also apply to other  $\alpha$  values.

With OBC-A, when  $\alpha = 0$ , the  $\mathbf{R}$  matrix may not be diagonal in 2D, as long as its elements  $a_{ij}$  ( $i, j = 1, 2$ ) satisfy the conditions (45a), (45b) and (48). We observe however that non-zero off-diagonal elements ( $a_{21}$  and  $a_{12}$ ), especially when  $a_{21} \neq 0$ , can result in poor or unphysical simulation results with OBC-A. This point is demonstrated by the velocity distributions (steady-state) in Fig. 7 for Reynolds number  $Re = 20$ , which are computed using OBC-A with  $\alpha = 0$  and several  $a_{21}$  values ( $a_{21} = -0.4, 0.0$  and  $0.4$ ), while  $a_{11} = a_{22} = a_{12} = 0$  in the  $\mathbf{R}$  matrix. At this Reynolds number the velocity is expected to be approximately in the horizontal direction at the outflow boundary. To one’s surprise, when  $a_{21} \neq 0$ , the computed velocity at the outflow boundary points to an oblique direction, even though all the velocity vectors are approximately along the horizontal direction inside the domain; see Figs. 7(a)-(b). The angle of the velocity vectors on the boundary depends on the sign and the magnitude of  $a_{21}$ . If  $a_{21} = 0$ , on the other hand, the computed velocity is approximately along the horizontal direction as expected (Fig. 7(c)). The above unphysical results can be understood by considering equation (50b) for OBC-A, which in this case is reduced to the following on the boundary,  $v \frac{\partial v}{\partial x} = \frac{\lambda_1 - \lambda_3}{\mathcal{K}} a_{21} u + \frac{\lambda_1}{\mathcal{K}} v$ , where  $u$  and  $v$  are the  $x$  and  $y$  components of the velocity. This equation indicates that the horizontal velocity  $u$  will contribute to the vertical velocity  $v$  at the outflow boundary when  $a_{21} \neq 0$ . Therefore, even if  $v = 0$  inside the domain, a non-zero  $v$  will be generated on the outflow boundary due to the boundary condition, leading to poor velocity distributions. By considering equation (50a), one can infer that the parameter  $a_{12}$  has an analogous effect. It induces a contribution of the tangent velocity  $u_\tau$  to the normal velocity  $u_n$  on the open boundary. In practical simulations,  $a_{12}$  seems not as detrimental to the results as  $a_{21}$  does, which is probably because of the pressure term involved in  $T_{nm}$  in equation (50a).

Let us next consider OBC-B and OBC-C. Table 2 also lists the mean and rms forces on the cylinder at the Reynolds numbers  $Re = 10, 20$  and  $100$  that are computed using OBC-B and OBC-C as the outflow boundary condition. It is observed that the forces based on OBC-B and OBC-C are identical to those based on the traction-free condition for  $Re = 10$  and  $20$ . For  $Re = 100$ , the forces obtained using OBC-B and OBC-C are essentially the same as that from the traction-free condition, with only a negligible difference.

Fig. 8 shows a comparison of the streamwise velocity profiles along the vertical direction at three downstream locations ( $x/d = 1.0, 5.0$  and  $10.0$ ) and along the centerline ( $y/d = 0$ ) among results computed using OBC-B, OBC-C, and the traction-free condition at Reynolds number  $Re = 20$ . Note that  $x/d = 10$  is the outflow boundary. We observe that all the velocity profiles computed using OBC-B and OBC-C and the traction-free condition exactly overlap with one another. These results suggest that both OBC-B and OBC-C result in the same flow distributions as the traction-free condition.

Fig. 9 compares the streamwise velocity profiles at  $Re = 20$  obtained using the outflow boundary conditions OBC-B and the best case of OBC-A ( $a_{11} = a_{22} = -0.2, \alpha = \frac{1}{2}$ ). In the near wake ( $\frac{x}{d} \lesssim 5$ ) the velocity profiles corresponding to these two boundary conditions essentially overlap with each other. Further downstream ( $\frac{x}{d} \gtrsim 6$ ), some difference can be noticed in the profiles resulting from these two boundary conditions (Figs. 9(c,d)). But the differences seem quite small. These results suggest that the boundary conditions OBC-A with  $a_{11} = a_{22} = -0.2$  and OBC-B produce close velocity distributions for this problem.

Let us next consider the cylinder flow at higher Reynolds numbers ( $Re \geq 2000$ ). At these Reynolds numbers the vortices shed from the cylinder can persist far downstream into the wake, and thus may cross the outflow boundary and exit the

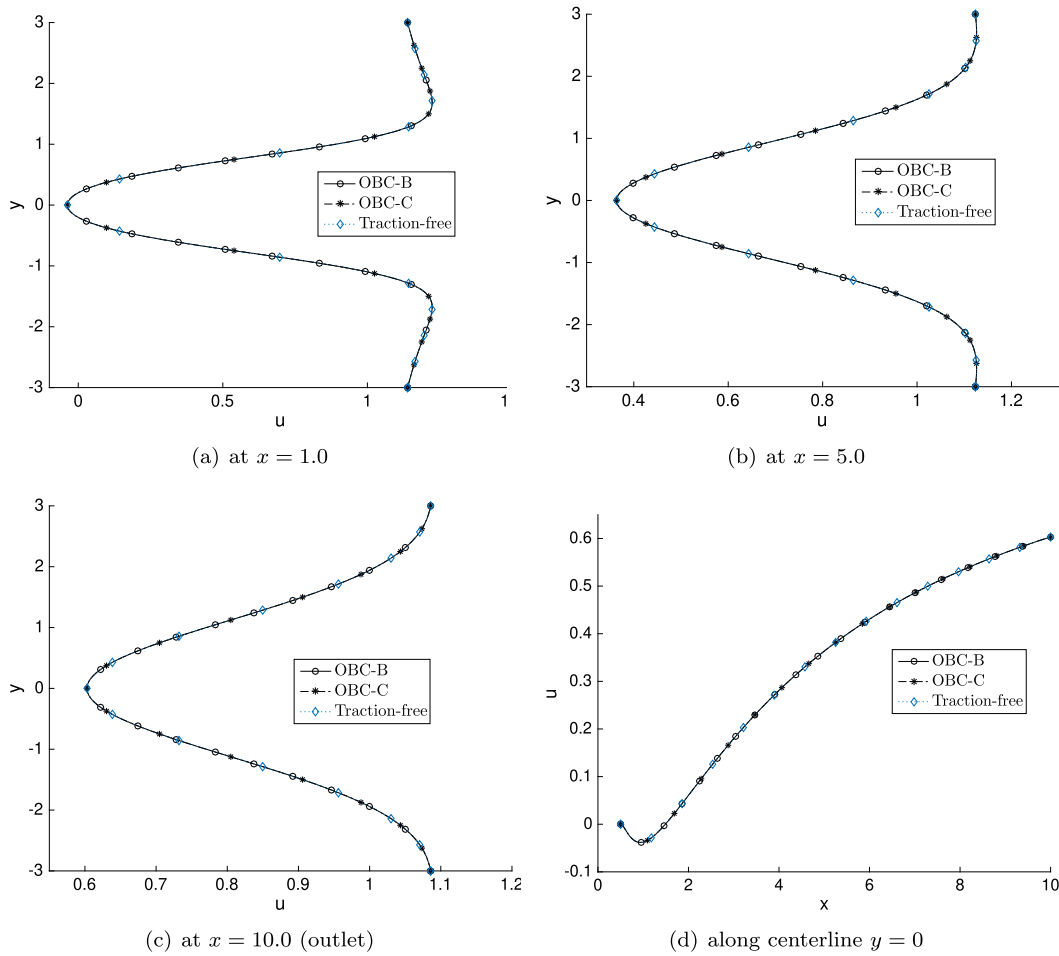


**Fig. 8.** 2D Cylinder flow ( $Re = 20$ ): Streamwise velocity profiles at several downstream locations in the wake and along the centerline of domain, computed using OBC-B and OBC-C as the outflow boundary condition. Velocity profiles obtained with the traction-free condition are included for comparison.

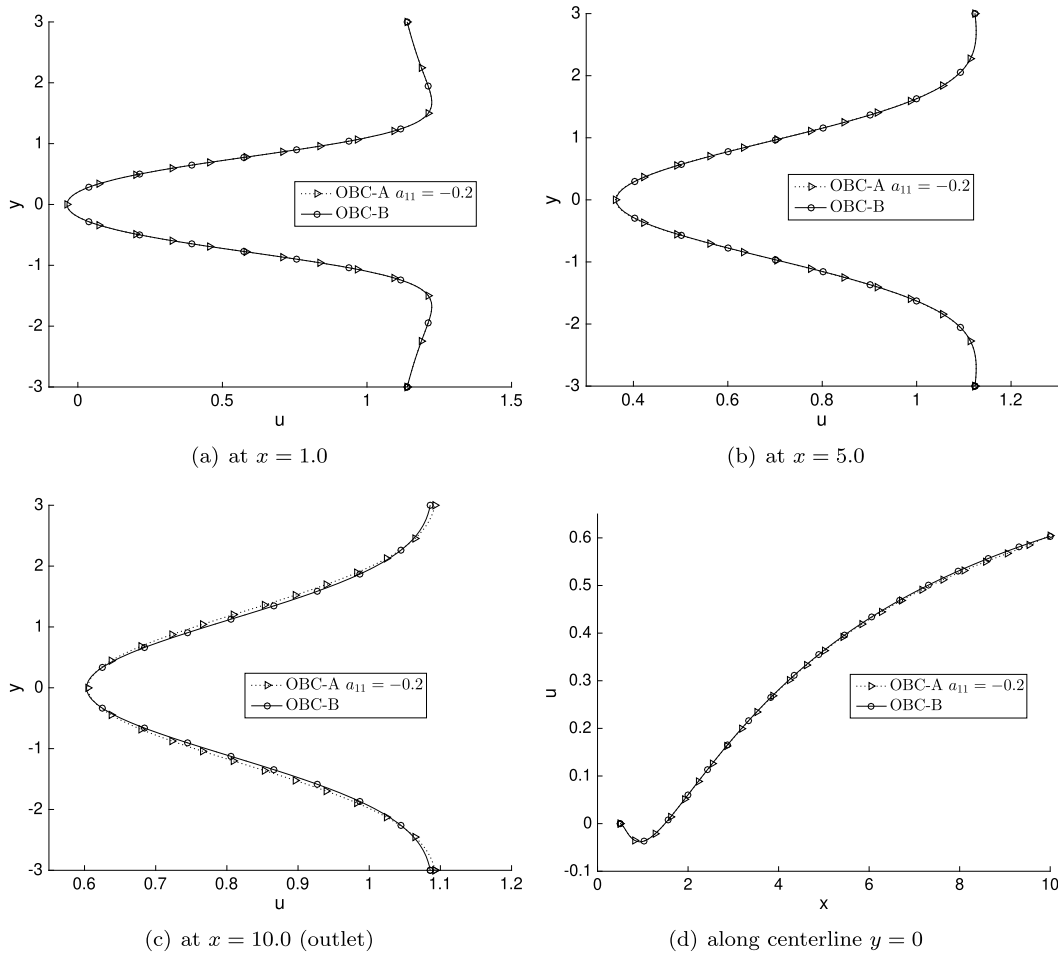
domain. This can cause severe difficulties and instabilities (backflow instability [12]) to conventional methods. Energy-stable boundary conditions are critical to overcoming the backflow instability for successful simulations at these Reynolds numbers. We have conducted long-time simulations at several Reynolds numbers ranging from  $Re = 2000$  to  $Re = 10000$  using the methods developed herein to test their performance. Note that the traction-free boundary condition is unstable for simulations in this range of Reynolds numbers.

Fig. 10 shows a temporal sequence of snapshots of the instantaneous velocity fields at  $Re = 5000$ , illustrating the dynamics of the cylinder wake based on 2D simulations. These results are obtained using OBC-B as the outflow boundary condition, and the element order is 8 and  $\Delta t = 2.5e - 4$ . One can observe pairs of vortices shed from the cylinder. These vortices are convected downstream and persist in the entire wake region. The vortices successively approach and pass through the outflow boundary, and discharge from the domain. It is observed that our method is able to allow the vortices to cross the outflow/open boundary and exit the domain in a fairly natural way (see Figs. 10(a)-(e) and 10(f)-(i)). But some distortion to the vortices can also be observed as they pass through the outflow boundary.

Long-time simulations have been performed and our methods are stable for these high Reynolds numbers. The long-term stability of the method is demonstrated by Fig. 11, which plots the time histories of the lift on the cylinder at Reynolds numbers  $Re = 5000$  (Fig. 11(a)-(b)) and  $Re = 10000$  (Fig. 11(c)-(d)). These simulations are conducted using OBC-B (Fig. 11(a) and (c)) and OBC-C (Fig. 11(b) and (d)) as the outflow boundary condition. The long-term stability of the simulations and the chaotic nature of flow are evident from the time signals.

### 3.2.2. Three-dimensional simulations

We next look into the simulation of the cylinder flow in three dimensions. Consider the 3D domain sketched in Fig. 3(b),  $-5d \leq x \leq 10d$ ,  $-10d \leq y \leq 10d$ , and  $0 \leq z \leq L_z$ , where  $d$  again denotes the cylinder diameter and  $L_z$  is the domain dimension along the  $z$  direction. The cylinder axis is assumed to coincide with the  $z$  axis of the coordinate system. The top and bottom of domain ( $y = \pm 10d$ ) are assumed to be periodic. We also assume that all the flow variables and the domain

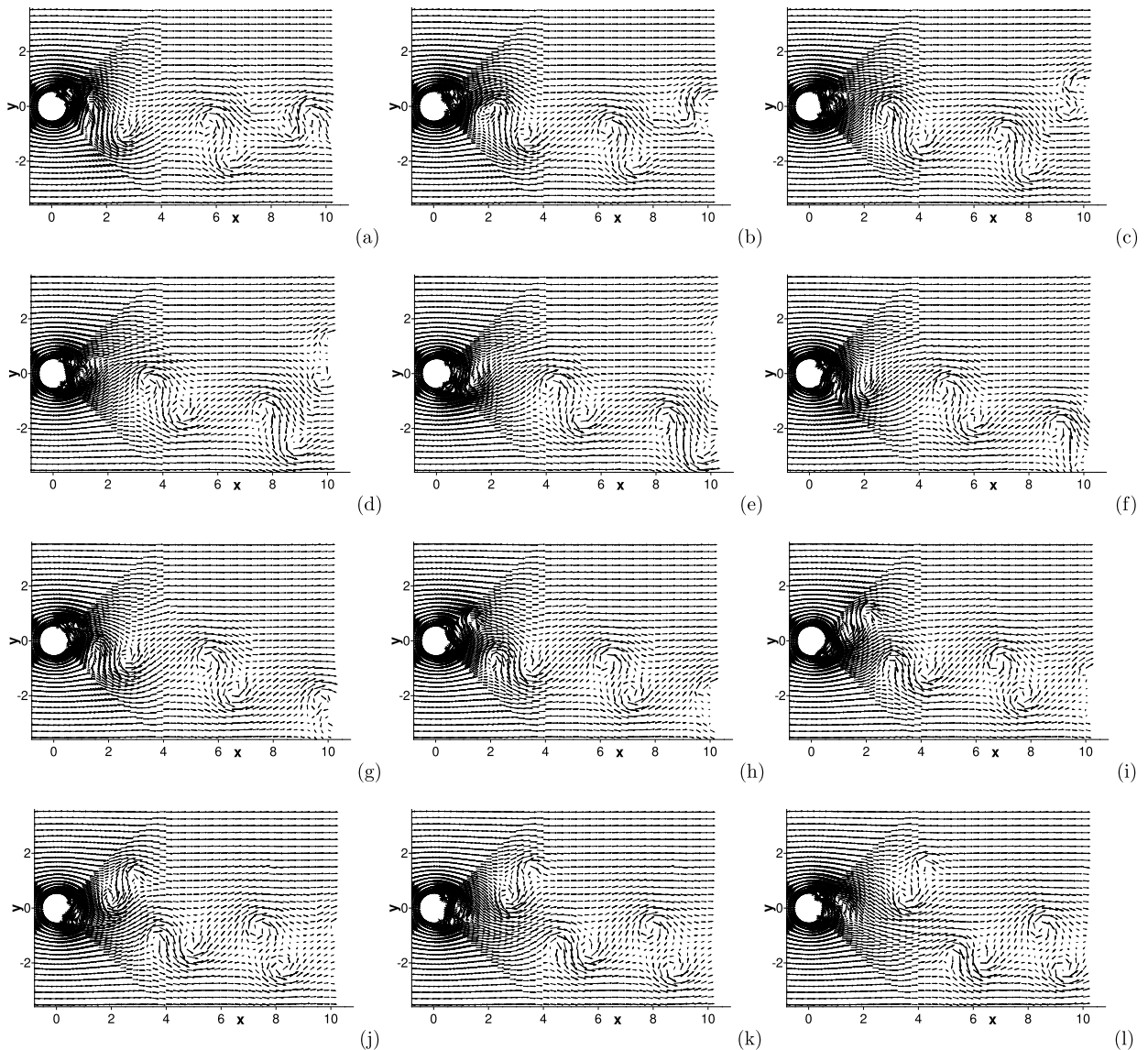


**Fig. 9.** 2D Cylinder flow ( $Re = 20$ ): Comparison of streamwise velocity profiles at several downstream locations and along the centerline, computed using OBC-A ( $a_{11} = a_{22} = -0.2$ ,  $\alpha = 1/2$ ) and OBC-B.

are homogeneous in  $z$  direction and are periodic at  $z = 0$  and  $z = L_z$ , and therefore a Fourier expansion of the field variables in  $z$  can be carried out. A uniform inflow with a free stream velocity  $U_0$  enters the domain at  $x = -5d$  along the  $x$  direction, and the wake discharges from the domain through the boundary at  $x = 10d$ . As in 2D simulations, all length variables are normalized by the cylinder diameter  $d$  and all velocity variables are normalized by the free stream velocity  $U_0$ . Therefore, the Reynolds number is defined based on  $U_0$  and  $d$ .

We consider two Reynolds numbers  $Re = 500$  and  $5000$  for 3D simulations. We employ a domain dimension  $L_z/d = 1.0$  along the  $z$  direction for  $Re = 500$  and a dimension  $L_z/d = 2.0$  for  $Re = 5000$ . The domain is discretized using 32 uniform points (i.e. 32 Fourier planes) along the  $z$  direction, and each of the plane ( $x$ - $y$  plane) is discretized using a mesh of 1228 quadrilateral spectral elements with an element order 6. Fig. 3(b) is a sketch of the 3D domain and the spectral element mesh within the  $x$ - $y$  planes. In the current work the mesh used in each  $x$ - $y$  plane for the 3D simulations is exactly the same as that of Fig. 3(a) for the 2D simulations in Section 3.2.1. We impose the no-slip condition (i.e. zero velocity) on the cylinder surface, and the Dirichlet condition (71) on the left boundary ( $x = -5d$ ), in which the boundary velocity is set according to the free stream velocity. On the top/bottom boundaries ( $y = \pm 10d$ ) periodic boundary conditions are imposed. Along the  $z$  direction a periodic condition is enforced because of the Fourier expansions of the field variables. On the outflow boundary  $x = 10d$  the open boundary condition (72) from Section 2 is imposed. Both OBC-B and OBC-C are employed for 3D simulations. Long-time simulations are performed and the flow has reached a statistically stationary state. So the initial conditions will have no effect on the state of the flow. The normalized time step size is  $\Delta t = 2.5e - 4$ .

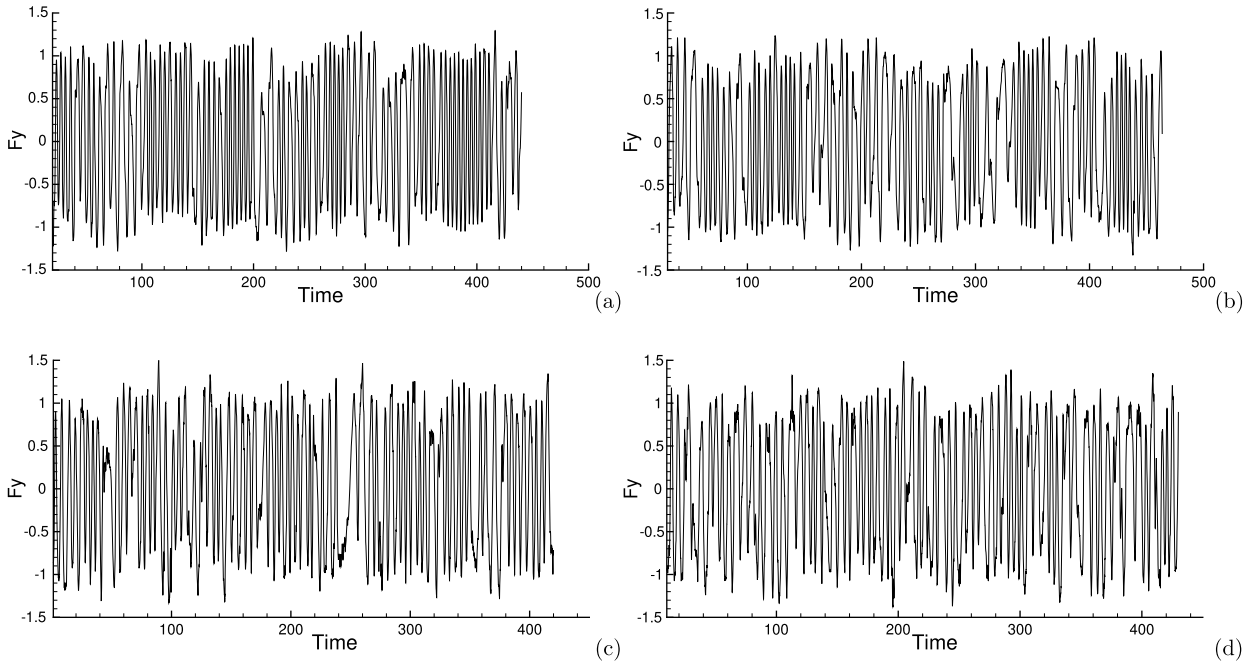
Fig. 12 shows a visualization of the vortices in the cylinder wake by plotting the iso-surfaces of the pressure fields at  $Re = 500$  (plot (a)) and  $Re = 5000$  (plot (b)). These results are obtained using OBC-C as the outflow boundary condition. In addition to the spanwise vortices (“rollers”) in the wake, 3D flow structures along the streamwise direction can be clearly observed. With the larger Reynolds number, the flow structures exhibit notably finer length scales, and the flow field is much noisier.



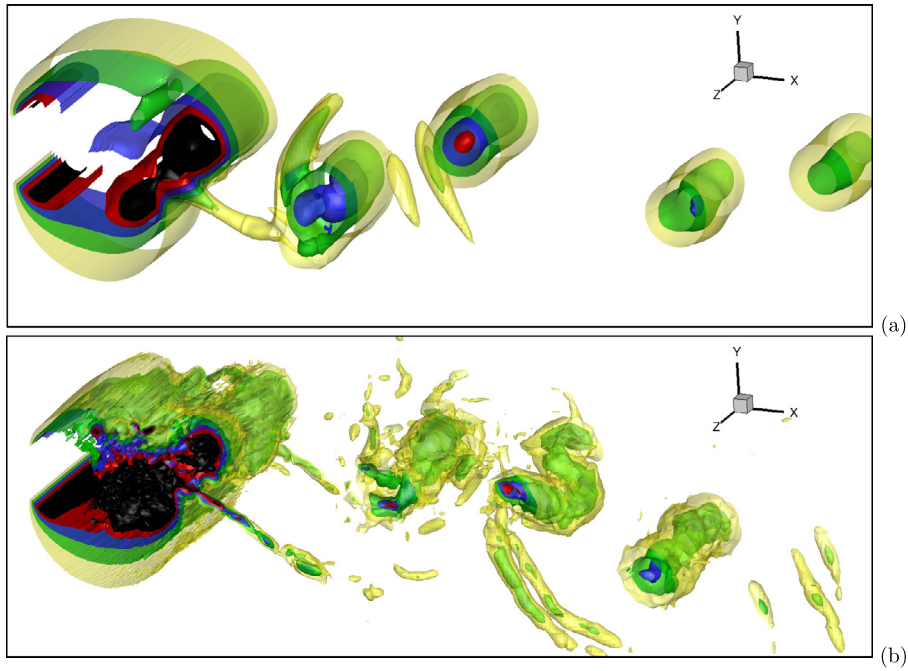
**Fig. 10.** Temporal sequence of snapshots of velocity fields ( $Re = 5000$ ): (a)  $t = 443.2$ , (b)  $t = 444.2$ , (c)  $t = 445.2$ , (d)  $t = 446.2$ , (e)  $t = 447.2$ , (f)  $t = 448.2$ , (g)  $t = 449.2$ , (h)  $t = 450.2$ , (i)  $t = 451.2$ , (j)  $t = 452.2$ , (k)  $t = 453.2$ , (l)  $t = 454.2$ . Velocity vectors are plotted on every eighth quadrature points in each direction within each element. Results are obtained using OBC-B as the outflow boundary condition.

Fig. 13 shows the time histories of the drag and lift on the cylinder at the two Reynolds numbers  $Re = 500$  (plot (a)) and  $Re = 5000$  (plot (b)) from the 3D simulations, which are obtained using OBC-B as the outflow boundary condition. The history signals show that the flow has reached a statistically stationary state. They also demonstrate the long-term stability of the methods developed herein. The energy-stable boundary conditions are critical to the stability of 3D simulations at moderate and high Reynolds numbers. It is observed that with the traction-free OBC the 3D simulation is unstable at the higher Reynolds number  $Re = 5000$ . One can also compare the lift history in Fig. 13(b) from 3D simulations with that in Fig. 11(a) from 2D simulations, both at Reynolds number  $Re = 5000$  and corresponding to OBC-B as the outflow boundary condition. The 2D simulation leads to much larger lift amplitudes (and correspondingly larger rms lift coefficient) than the 3D simulation for the same Reynolds number, which is well-known in the literature [11,13].

We have computed the drag coefficient and the rms lift coefficient based on the force histories at  $Re = 500$  and  $Re = 5000$ . These data from 3D simulations are included in Fig. 5 for comparison with the experimentally determined coefficient values. It is observed that the current 3D results are in reasonably good agreement with the experimental data. In contrast, 2D simulations grossly over-predict both the drag and the rms-lift coefficients in the regime where the flow is physically three-dimensional.



**Fig. 11.** Time histories of the lift on the cylinder at Reynolds numbers  $Re = 5000$  ((a) and (b)) and  $Re = 10000$  ((c) and (d)). Results in (a) and (c) are computed using OBC-B, and those in (b) and (d) are computed using OBC-C, as the outflow boundary condition.



**Fig. 12.** (color online) Visualization of vortices in 3D cylinder flow: Pressure isosurfaces (five uniform levels between  $p = -0.6$  and  $p = -0.2$ ) at Reynolds numbers (a)  $Re = 500$  and (b)  $Re = 5000$ . Results are obtained with OBC-C as the outflow boundary condition.

### 3.3. Jet impinging on a wall

In this section we test further the current methods with another problem, a jet impinging on a solid wall, using two-dimensional simulations. Due to the open boundaries and the physical instability of the jet, the open boundary condition is critical to the successful simulation of this flow.

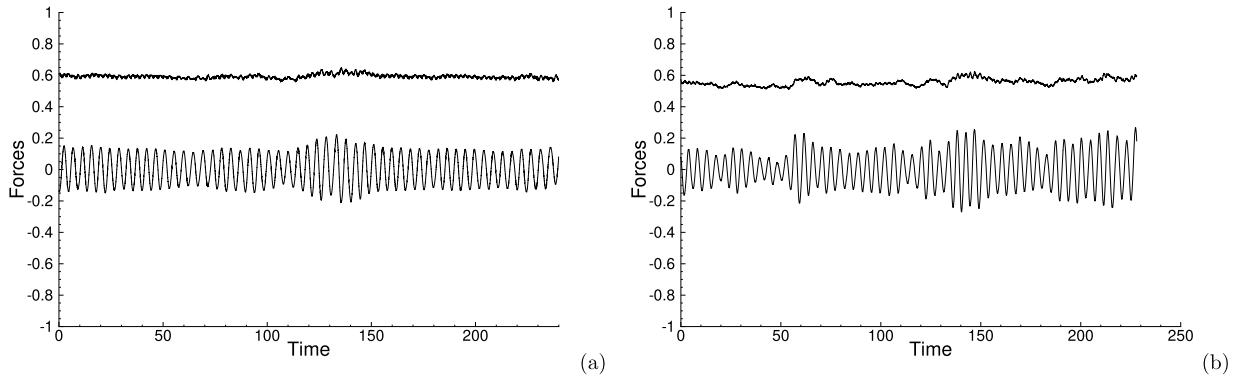


**Fig. 13.** 3D cylinder flow: time histories of drag and lift on the cylinder at Reynolds numbers (a)  $Re = 500$  and (b)  $Re = 5000$ . Results correspond to OBC-B as the outflow boundary condition.

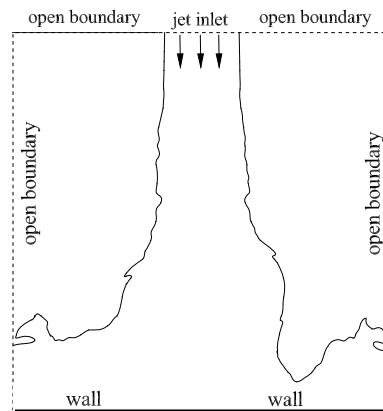


**Fig. 14.** Problem configuration of the impinging jet on a wall.

Specifically, we study a fluid jet of diameter  $d$  impinging on a wall in 2D. Fig. 14 illustrates the configuration of this problem. Consider a rectangular domain,  $-\frac{5}{2}d \leq x \leq \frac{5}{2}d$  and  $0 \leq y \leq 5d$ , where  $x$  and  $y$  axes are along the horizontal and vertical directions, respectively. The bottom side of the domain is a solid wall. The inlet of the jet (with diameter  $d$ ) is located in the middle of the top side of the domain, namely,  $-R_0 \leq x \leq R_0$  and  $y = 5d$ , where  $R_0$  is the radius of the inlet ( $R_0 = \frac{d}{2}$ ). The jet velocity is assumed to have the following profile at the inlet,

$$\begin{cases} u = 0 \\ v = -U_0 \left[ \tanh \frac{1-x/R_0}{\sqrt{2}\epsilon/d} (H(x, 0) - H(x, R_0)) + \tanh \frac{1+x/R_0}{\sqrt{2}\epsilon/d} (H(x, -R_0) - H(x, 0)) \right] \end{cases} \quad (87)$$

where  $U_0$  is the velocity scale ( $U_0 = 1$ ),  $\epsilon = \frac{1}{40}d$ , and  $H(x, a)$  is the unit step function, taking the unit value if  $x \geq a$  and vanishing otherwise. The rest of the domain boundaries, on the top and on the left and right sides, are all open, where the fluid can freely enter or leave the domain. The jet enters the domain through the inlet on the top, impinges on the bottom wall and splits into two streams, which then flow sideways out of the domain. The goal is to simulate and study this process.

We discretize the domain using a spectral element mesh of 400 quadrilateral elements, with 20 uniform elements along the  $x$  and  $y$  directions. No-slip condition is imposed on the bottom wall. At the jet inlet we impose the Dirichlet condition (71), in which  $\mathbf{w}$  is given by (87). On the rest of the domain boundary the OBC (72) is imposed, and the three conditions (OBC-A, OBC-B and OBC-C) are employed and tested. Long-time simulations have been performed, and the flow has reached a statistically stationary state. So the initial condition is immaterial and will have no effect on the long-term flow behavior. The physical variables are normalized based on the jet diameter  $d$  and the velocity scale  $U_0$ . So the Reynolds number is defined based on these scales accordingly. In accordance with the previous simulations of a variant of this problem [14], we employ an element order 12 and a time step size  $\Delta t = 2.5e - 4$  for the current simulations.

An overview of the flow characteristics is provided by Fig. 15. It shows the instantaneous velocity fields at three Reynolds numbers:  $Re = 300$ , 2000 and 10000, which are computed using OBC-C as the open boundary condition. At a sufficiently low Reynolds number (e.g.  $Re = 300$ ) this flow is at a steady state. After impinging on the wall, the vertical jet splits into two horizontal streams, and flow in opposite directions parallel to the wall until they exit the domain (Fig. 15(a)). In regions

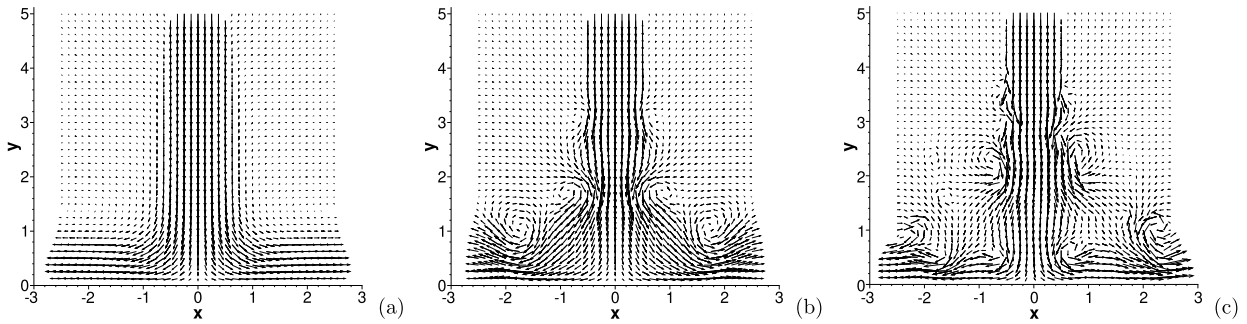


**Fig. 15.** Characteristics of the impinging jet: instantaneous velocity distribution at Reynolds numbers (a)  $Re = 300$ , (b)  $Re = 2000$ , and (c)  $Re = 10000$ . Velocity vectors are plotted on every eighth quadrature point in each direction within each element. Results are computed using OBC-C as the open boundary condition.

outside the jet stream the velocity appears negligibly small. As the Reynolds number increases the flow becomes unsteady. The vertical jet stream appears stable within some distance downstream of the inlet, and then the Kelvin-Helmholtz instability develops and the jet becomes physically unstable. Successive pairs of vortices form along the profile of the jet, and they are convected downstream and eventually out of the domain along with the jet (Fig. 15(b)). For even higher Reynolds numbers, the region with a stable jet profile shrinks, and the onset of instability moves markedly upstream toward the inlet. The vortices forming along the jet profile appear more irregular and numerous, and their interactions lead to more complicated dynamics (Fig. 15(c)).

Let us first focus on a low Reynolds number  $Re = 300$  and study the effects of different OBCs on the simulation results. Fig. 16 compares the velocity field distributions at  $Re = 300$  computed using OBC-A with  $\alpha = \frac{1}{2}$  and a range of values for  $a_{11}$  (and  $a_{22}$ , with  $a_{22} = a_{11}$ ). The result obtained using the traction-free open boundary condition (86) and OBC-B are also included for comparison. These results can be compared with that of Fig. 15(a), which is also for  $Re = 300$  but computed using OBC-C as the open boundary condition. We can make the following observations from these results:

- OBC-B and OBC-C result in velocity field distributions similar to the traction-free condition.
- The  $a_{11}$  (and  $a_{22}$ ) values strongly influence the velocity fields computed with OBC-A. The velocity distributions obtained using OBC-A with different  $a_{11}$  (and  $a_{22}$ ) values are qualitatively different.
- The velocity fields obtained using OBC-A with  $a_{11} = a_{22} = 0.5, 0.2, 0$ , and  $-0.2$  exhibit a pair (or more) of large vortices filling up the domain, which is unphysical. With larger  $a_{11}$  (and  $a_{22}$ ), the results even indicate that the flow and the vortices go out of the domain through the upper boundary.
- The flows obtained using OBC-A with  $a_{11} = a_{22} = 0.5, 0.2$  and  $0$  are unsteady for  $Re = 300$ . The forces on the wall obtained with these methods fluctuate over time, albeit in a narrow range.
- The velocity distributions computed using OBC-A with  $a_{11} = a_{22} = -0.5$  and  $-0.75$  exhibit an overall similarity to that obtained with the traction-free condition. However, in the horizontal jet streams obtained with these methods, the directions of the velocity vectors seem un-natural at the open boundary (Fig. 16(e)-(f)). In addition, although it is quite weak, a pair of large vortices can be discerned from the velocity field obtained using OBC-A with  $a_{11} = a_{22} = -0.5$  (Fig. 16(e)).
- Using the velocity field resulting from the traction-free condition as a reference, the best result for OBC-A seems to correspond to a parameter value around  $a_{11} = a_{22} = -0.5$  for this problem.

Table 3 lists the forces ( $y$ -component) on the wall obtained using different methods at  $Re = 300$ . Since the flow computed using OBC-A with  $a_{11} = a_{22} = 0.5, 0.2$  and  $0.0$  is unsteady, listed in the table are the mean and rms forces corresponding to these methods. With increasing  $a_{11}$  (and  $a_{22}$ ), the force computed using OBC-A increases substantially in magnitude. The discrepancy in the forces between OBC-A and the traction-free condition is significant. Compared with the traction-free condition, the best result obtained using OBC-A appears to correspond to around  $a_{11} = a_{22} = -0.5$ . On the other hand, the forces obtained using OBC-B and OBC-C are the same, and they are very close to the that from the traction-free condition.

Let us next look into the impinging jet at higher Reynolds numbers. Fig. 17 shows a temporal sequence of snapshots of the velocity fields at  $Re = 5000$  computed using OBC-B as the open boundary condition. These results illustrate the vortex-pair formation and the transport of the train of vortices downstream along the jet profile. They also signify that our method can allow the vortices to pass through the open boundary in a smooth and fairly natural fashion; see the left boundary in Figs. 17(c)-(f). On the other hand, a certain degree of distortion to the vortices as they cross the open boundary can also be observed (Fig. 17(f)). The physical instability of the jet and the presence of vortices on the open boundaries make these simulations very challenging. The current OBCs are very effective for such problems. It is noted that the traction-free condition is unstable in these simulations.

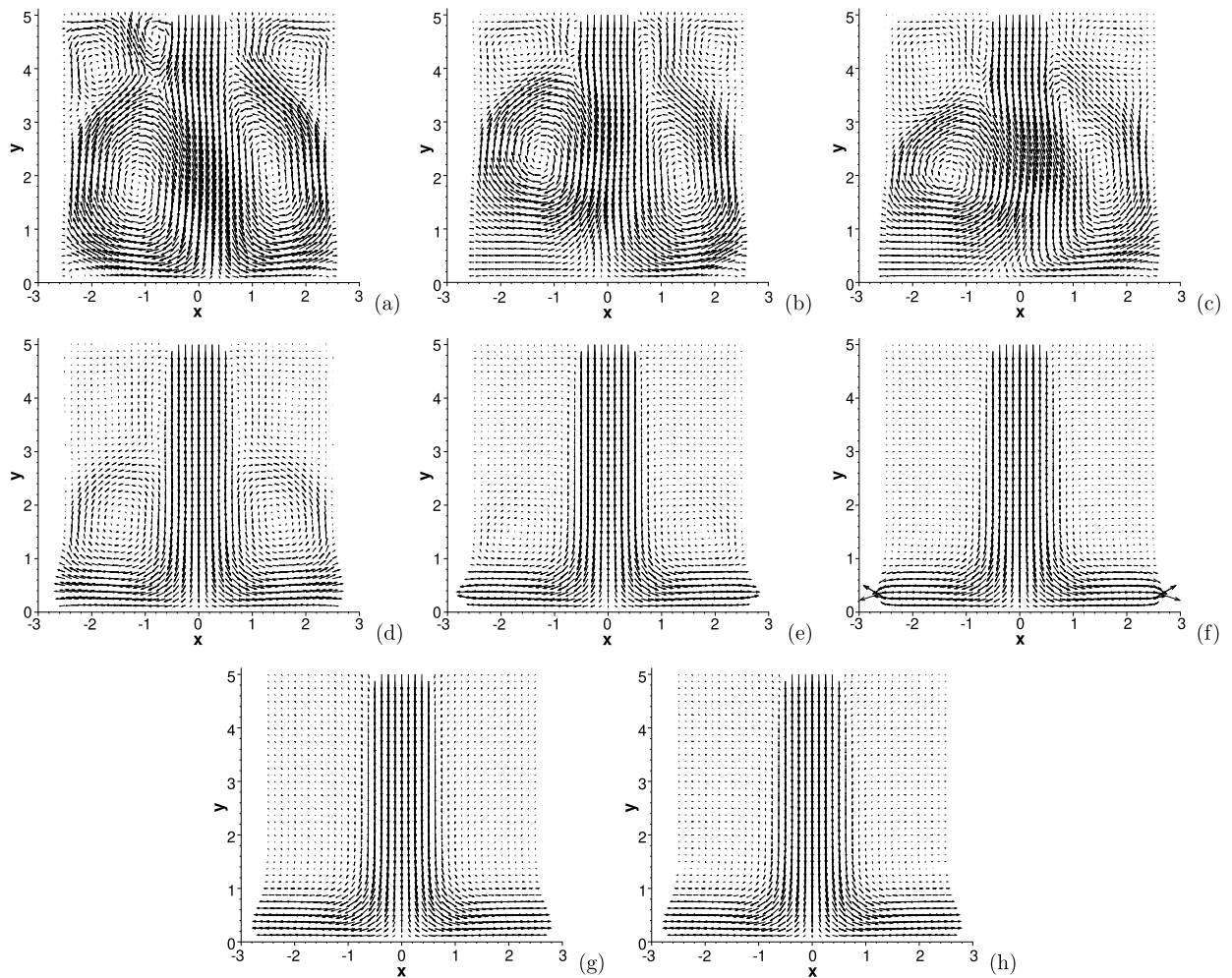


**Fig. 16.** Impinging jet ( $Re = 300$ ): velocity distributions computed using OBC-A with  $\alpha = \frac{1}{2}$  ((a)–(f)), the traction-free condition (g), and OBC-B (h). Different parameter values for  $a_{11}$  (and  $a_{22}$ , with  $a_{22} = a_{11}$ ) have been tested with OBC-A. They are  $a_{11} = a_{22} = 0.5$  (a), 0.2 (b), 0.0 (c),  $-0.2$  (d),  $-0.5$  (e), and  $-0.75$  (f). Velocity vectors are plotted on every eighth quadrature points in each direction within each element.

**Table 3**

Impinging jet ( $Re = 300$ ): vertical force on the wall computed using OBC-A (with  $\alpha = 1/2$  and various  $a_{11} = a_{22}$  values), OBC-B, OBC-C, and the traction-free condition.

Method	Parameters	$f_y$ (or mean- $f_y$ )	rms- $f_y$
OBC-A	$a_{11} = a_{22} = -0.75$	-0.912	0
	-0.5	-0.986	0
	-0.2	-1.189	0
	0	-1.384	0.0408
	0.2	-1.653	0.102
	0.5	-2.343	0.0922
OBC-B		-0.994	0
OBC-C		-0.994	0
Traction-free OBC		-1.026	0

Let us next take a closer view of the distortion to the vortices as they exit the domain through the open boundary. Fig. 18 illustrates the typical scenario when a vortex crosses the open boundary, obtained with OBC-C. This figure shows a temporal sequence of velocity fields near the right open boundary and the bottom wall. The insets of Figs. 18(b)–(e) are magnified views of a section of the open boundary near the vortex core. As the vortex approaches the open boundary, the velocity patterns show that it maintains an almost perfect circular shape, with essentially no or very little distortion (Fig. 18(a)–(d)). Then as the vortex core moves very close to the boundary a notable deformation becomes evident (Fig. 18(e)). The vortex

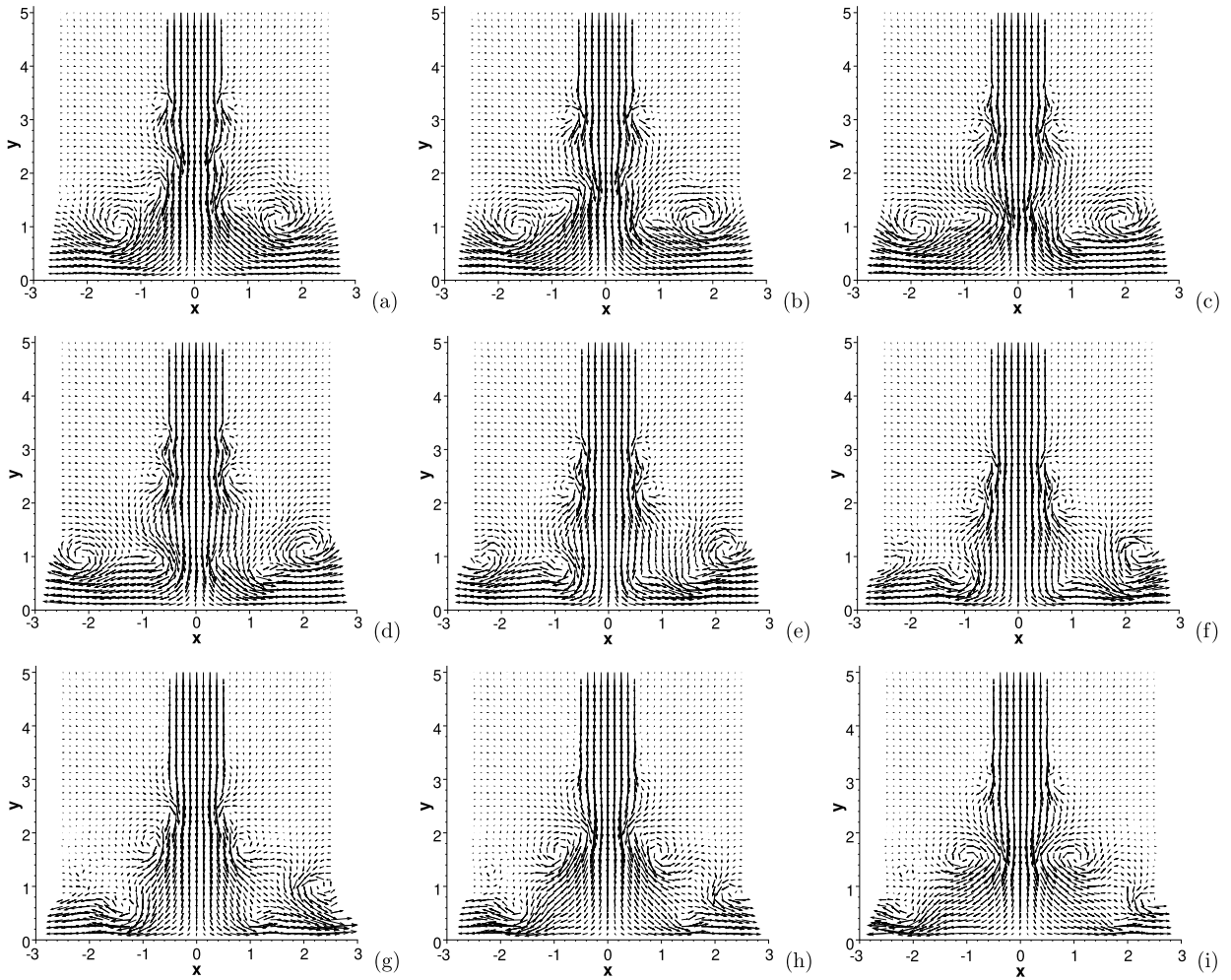


**Fig. 17.** Impinging jet ( $Re = 5000$ ): temporal sequence of snapshots of the instantaneous velocity fields at (a)  $t = 619.05$ , (b)  $t = 619.65$ , (c)  $t = 620.25$ , (d)  $t = 620.85$ , (e)  $t = 621.45$ , (f)  $t = 622.05$ , (g)  $t = 622.65$ , (h)  $t = 623.25$ , (i)  $t = 623.85$ . Velocity vectors are plotted on every eighth quadrature point in each direction within each element. Results are computed using OBC-B as the open boundary condition.

deforms into an oval and is elongated in an oblique direction to the boundary. The vortex retains an oval shape until it discharges completely from the domain. For comparison, Fig. 19 shows a comparable and typical scenario of the vortex exiting the domain obtained using the OBC from [10], but without the inertia (i.e. time derivative) term therein so that the boundary condition is also a traction-type condition. We observe a similar process, with the initial circular vortex distorted into an oval shape as it moves out of the domain (Fig. 19(e)). But the velocity patterns of Figs. 18 and 19 also reveal a notable difference. The vortex in Fig. 19 experiences another type of distortion, even before the distortion into an oval becomes evident. More specifically, we observe that, as the vortex approaches the open boundary, on the section of the boundary influenced by the vortex rotation and in its vicinity, the velocity vectors tend to point along the tangential direction to the boundary. This is evident from the insets of Figs. 19(b)–(d). This makes the velocity pattern in that region less congruent or incongruent with those outside the region, thus causing an apparent distortion to the vortex. This is especially evident from Figs. 19(c) and (d). As the vortex further evolves in time, this distortion seems to disappear and gives way to the distortion into an oval vortex (Figs. 19(d)–(e)). By contrast, from the velocity patterns obtained using the current OBC we observe that the vortex retains an essentially perfect shape (see Figs. 18(b)–(d)) and does not experience such a distortion as evidenced from Fig. 19, before the oval deformation kicks in. These results suggest that the current OBCs can be more favorable compared with that of [10] in the sense that they can produce more congruent and more natural velocity distributions near/at the open boundary and cause less distortion to the vortices as they pass through the boundary and exit the domain.

Long-time simulations have been performed using the current methods for the impinging jet flow. Fig. 20 illustrates the time histories of the vertical force on the wall at  $Re = 10000$ , obtained using OBC-B and OBC-C. The long history signals demonstrate the long-term stability of the methods developed in the current work, and that the flow has reached a statistically stationary state.

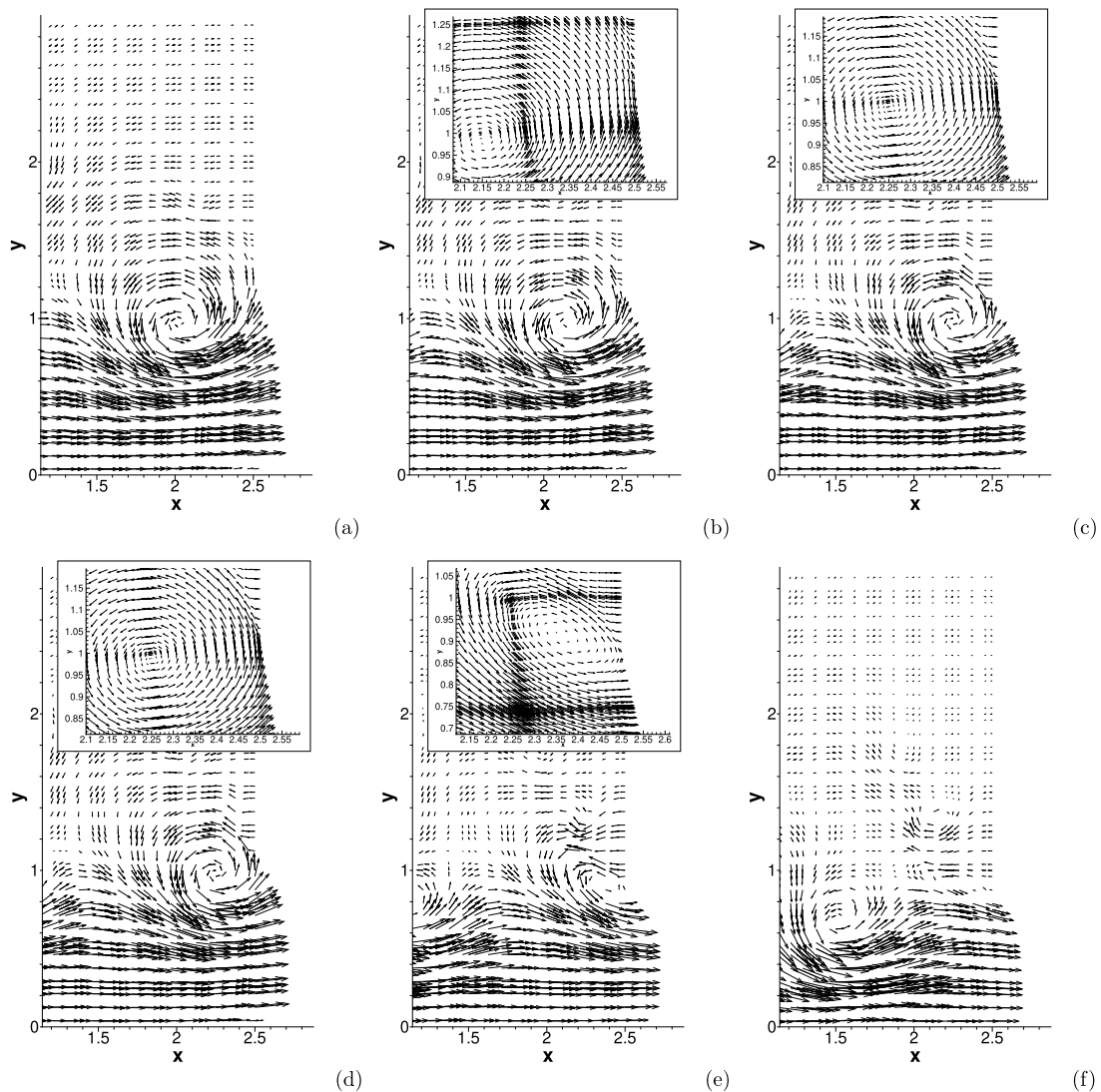


**Fig. 18.** Impinging jet ( $Re = 5000$ ): temporal sequence of velocity snapshots near the right open boundary showing the discharge of a vortex from the domain, computed using OBC-C as the open boundary condition. (a)  $t = 593.4$ , (b)  $t = 593.7$ , (c)  $t = 594$ , (d)  $t = 594.3$ , (e)  $t = 594.6$ , (f)  $t = 595.5$ . Velocity vectors are plotted on every fourth quadrature points in each direction within each element. The insets of (b)–(e) are velocity blow-up views (shown on every quadrature point) near the boundary.

#### 4. Concluding remarks

We have developed a set of new energy-stable OBCs for simulating outflow/open-boundary problems of incompressible flows. These boundary conditions can effectively overcome the backflow instability, and produce stable and accurate results when strong vortices or backflows occur at the open/outflow boundary.

The development of these boundary conditions involves two steps. First, we devise a general form of boundary conditions that ensure the energy stability on the open boundary by reformulating the boundary contribution into a quadratic form with a symmetric matrix. Second, we require that the scale of boundary dissipation, upon imposing the boundary conditions from the previous step, should match a physical scale and thus attain the final boundary conditions.

Both of these two steps are crucial. The first step ensures energy stability, and the second step ensures physical correctness and accuracy. Those boundary conditions resulting from the first step only are referred to as “OBC-A” in the current paper, and the boundary conditions “OBC-B” and “OBC-C” studied herein involve both steps in the development. Extensive numerical experiments are conducted to test the accuracy and performance of these boundary conditions. These tests show that, as expected, all three conditions (OBC-A, OBC-B and OBC-C) produce stable simulations, even when strong vortices or backflows occur at the open/outflow boundary. However, it is observed that OBC-A in general gives rise to poor or even unphysical simulation results, unless the algorithmic parameters take some “optimal” value for the flow problem under study. It is further observed that the “optimal” parameter values for OBC-A are unfortunately flow-problem dependent. For exam-

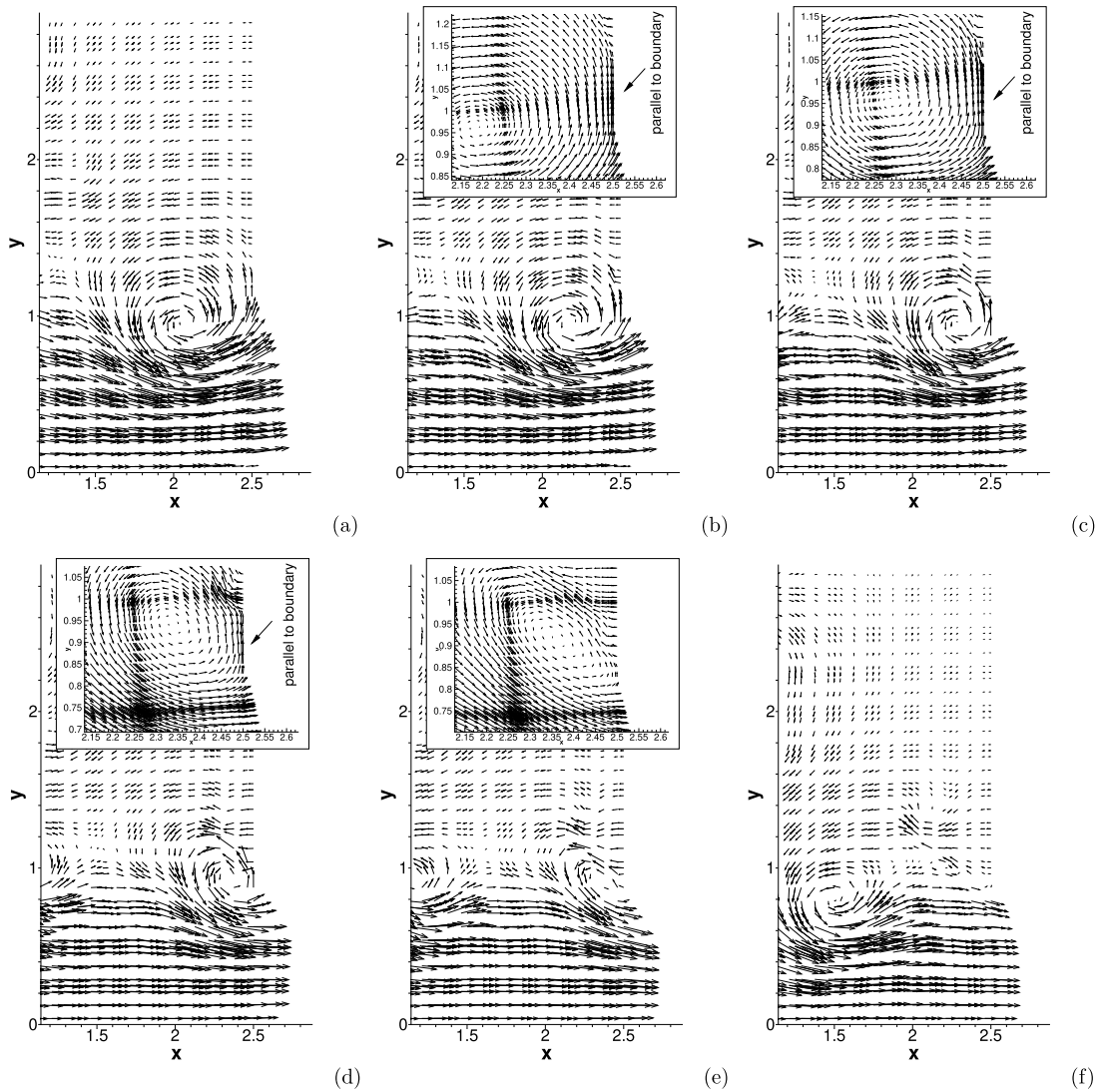


**Fig. 19.** Impinging jet ( $Re = 5000$ ): temporal sequence of velocity snapshots near the right boundary showing the discharge of a vortex from the domain, computed using the OBC from [10] (without the inertia term). (a)  $t = 1137.75$ , (b)  $t = 1138.05$ , (c)  $t = 1138.35$ , (d)  $t = 1138.65$ , (e)  $t = 1138.95$ , (f)  $t = 1139.85$ . Velocity vectors are plotted on every fourth quadrature point in each direction within each element. The insets of (b)–(e) show velocity blow-up views (shown on every quadrature point) near the boundary.

ple, for the cylinder flow the “optimal” values for  $a_{11}$  ( $a_{22}$ ) are around  $a_{11} = a_{22} = -0.2$ , while for the impinging jet they are around  $a_{11} = a_{22} = -0.5$  with OBC-A. It is further noted that OBC-A produces poor results with  $a_{11} = a_{22} = -0.5$  for the cylinder flow and with  $a_{11} = a_{22} = -0.2$  for the impinging jet problem. These observations suggest that OBC-A, i.e. the energy-stable boundary conditions resulting from the first step only, may only be of limited use in practice. While OBC-A leads to stable computations, the simulation results in general can deviate from the physical results considerably. In contrast, the open boundary conditions OBC-B and OBC-C lead to favorable results in terms of both stability and accuracy. Numerical experiments show that they produce stable and accurate results, compared with both experimental measurements and the results produced by other methods.

The OBCs devised based on the quadratic form can be formulated into a traction-type condition; see equation (72). These boundary conditions in general give rise to a non-zero traction on the entire open boundary, in both the backflow regions (if any) and the normal outflow regions. This is in contrast to the energy-stable boundary conditions from previous works (see e.g. [14]), which result in a non-zero traction in the backflow regions only and a zero traction in the normal outflow regions of the open boundary.

While their formulations are different, numerical experiments indicate that OBC-B and OBC-C tend to produce very similar or the same simulation results. The various numerical experiments appear to give a sense that the fluctuations in the physical quantities (e.g. forces) produced by OBC-B can at times be somewhat larger than that by OBC-C, resulting in

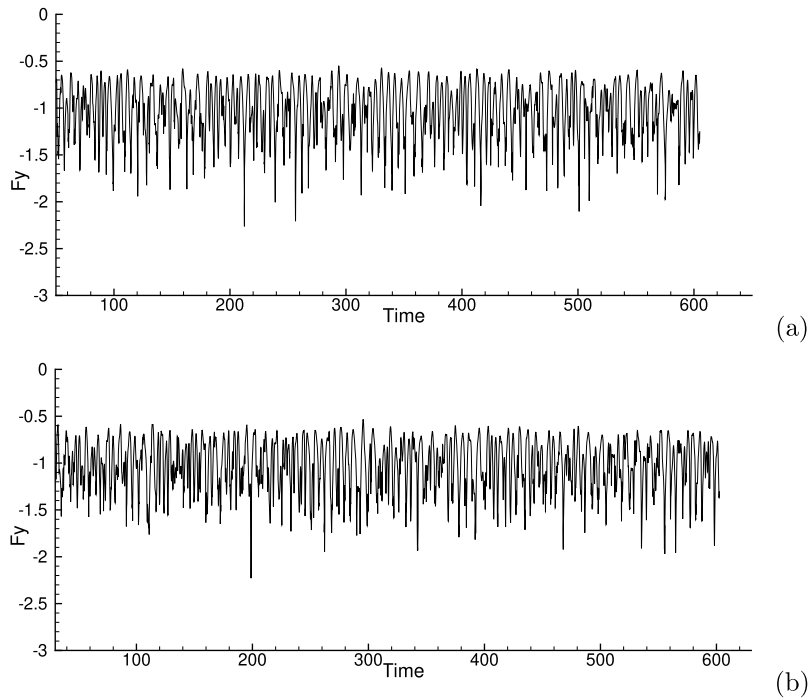


**Fig. 20.** Impinging jet: time histories of the vertical force on the bottom wall at  $Re = 10000$  computed using OBC-B (a) and OBC-C (b) as the open boundary condition.

e.g. higher values in the largest amplitude in the time-history signals. In such a sense, OBC-C may be somewhat more favorable when compared with OBC-B. But the difference in their simulation results, if any, is minor.

While the current OBCs can allow the vortices to cross the open/outflow boundary in a smooth and fairly natural fashion, even at quite high Reynolds numbers, a certain level of distortion to the vortices is also evident during the process. For example, an otherwise circular vortex can deform into an oval while exiting the domain through the open boundary. This type of distortion is also observed with previous methods (see e.g. [10]). However, as shown by the results in Section 3.3, the current OBC seems more favorable compared with that of [10] (without the inertia term) in terms of the distortions, because the current condition leads to velocity distributions more congruent on the open boundary and in its vicinity. In contrast, the boundary condition of [10] can lead to less congruent or incongruent velocity distributions on sections of the open boundary where the vortices cross, causing additional distortions.

It should be pointed out that, since the current OBCs are formulated in a traction form, it is not difficult to extend these conditions to arrive at a set of corresponding “convective-like” energy-stable OBCs, by e.g. incorporating an appropriate inertia term in a similar way to [10]. This may be desirable in term of the control over the velocity field on the open/outflow boundaries.

Backflow instability is one of the primary issues encountered when scaling up the Reynolds number in simulations of a large class of incompressible flows, such as wakes, jets, shear layers, and cardiovascular and respiratory flows. The method developed here provides a new effective technique to algorithmically eliminate the backflow instability. Algorithmic elimination of backflow instability can be critical to and will be instrumental in flow simulations at high (and moderate) Reynolds numbers. For example, it enables one to employ a significantly smaller computational domain (permitted by accuracy), thus leading to a much higher spatial resolution than otherwise, even with the same mesh size. The current work contributes a useful and effective tool toward the numerical simulations of such challenging problems.

## Acknowledgement

This work was partially supported by NSF (DMS-1318820, DMS-1522537).

## Appendix A. Proof of Theorem 2.1

Since  $\mathbf{A}$  and  $\mathbf{G}$  are symmetric and real matrices, all their eigenvalues are real. None of the eigenvalues of  $\mathbf{A}$  is zero because  $\det(\mathbf{A}) \neq 0$ . Suppose  $\lambda$  ( $\lambda \neq 0$ ) is an eigenvalue of  $\mathbf{A}$ . Then

$$\begin{aligned}
 0 &= \det \begin{bmatrix} -\lambda \mathbf{I} & -\mathbf{I} \\ -\mathbf{I} & \mathbf{G} - \lambda \mathbf{I} \end{bmatrix} = \det(-\lambda \mathbf{I}) \det[(\mathbf{G} - \lambda \mathbf{I}) - (-\mathbf{I})(-\lambda \mathbf{I})^{-1}(-\mathbf{I})] \\
 &= (-\lambda)^m \det \left[ \mathbf{G} - \left( \lambda - \frac{1}{\lambda} \right) \mathbf{I} \right] \\
 \implies \det \left[ \mathbf{G} - \left( \lambda - \frac{1}{\lambda} \right) \mathbf{I} \right] &= 0,
 \end{aligned} \tag{88}$$

where we have used the Schur complement. Therefore  $(\lambda - \frac{1}{\lambda})$  is an eigenvalue of  $\mathbf{G}$ . Suppose  $\xi$  is an eigenvalue of  $\mathbf{G}$ , and  $\lambda - \frac{1}{\lambda} = \xi$ . Then  $\lambda = \frac{\xi}{2} \pm \sqrt{\left(\frac{\xi}{2}\right)^2 + 1} \neq 0$ . So the steps in equation (88) can be reversed. We conclude that  $\lambda$  is an eigenvalue of the matrix  $\mathbf{A}$ .

Suppose  $\begin{bmatrix} \mathbf{Z} \\ -\lambda \mathbf{Z} \end{bmatrix}$  is an eigenvector of  $\mathbf{A}$  corresponding to the eigenvalue  $\lambda$ . Then  $\mathbf{Z} \neq 0$  and

$$\begin{aligned}
 0 &= \begin{bmatrix} -\lambda \mathbf{I} & -\mathbf{I} \\ -\mathbf{I} & \mathbf{G} - \lambda \mathbf{I} \end{bmatrix} \begin{bmatrix} \mathbf{Z} \\ -\lambda \mathbf{Z} \end{bmatrix} = \begin{bmatrix} 0 \\ -\mathbf{Z} - \lambda(\mathbf{G} - \lambda \mathbf{I})\mathbf{Z} \end{bmatrix} = \begin{bmatrix} 0 \\ -\lambda(\mathbf{G} - (\lambda - \frac{1}{\lambda})\mathbf{I})\mathbf{Z} \end{bmatrix} \\
 \implies \left( \mathbf{G} - \left( \lambda - \frac{1}{\lambda} \right) \mathbf{I} \right) \mathbf{Z} &= 0.
 \end{aligned} \tag{89}$$

We conclude that  $\mathbf{Z}$  is an eigenvector of  $\mathbf{G}$  corresponding to the eigenvalue  $(\lambda - \frac{1}{\lambda})$ . Now suppose  $(\lambda - \frac{1}{\lambda})$  is an eigenvalue of  $\mathbf{G}$  and  $\mathbf{Z}$  is the corresponding eigenvector. Then  $\lambda \neq 0$ , and the steps in (89) can be reversed. So we conclude that  $\begin{bmatrix} \mathbf{Z} \\ -\lambda \mathbf{Z} \end{bmatrix}$  is an eigenvector of  $\mathbf{A}$  corresponding to the eigenvalue  $\lambda$ .

**Appendix B. Summary of open boundary conditions**

In order to facilitate the implementation for the readers, this appendix summarizes the energy-stable OBCs from the main text.

*Two dimensions*

OBC-A:

Input:

- Boundary information: normal vector  $\mathbf{n}$ , tangent vector  $\boldsymbol{\tau}$ .
- Constant parameters:  $a_{11}, a_{22}, \alpha$ , where  $-1 \leq a_{11}, a_{22} < 1$  and  $0 \leq \alpha \leq \frac{1}{2}$ .

Boundary condition:

$$-p\mathbf{n} + \nu \mathbf{n} \cdot \nabla \mathbf{u} - [f_1(u_n, u_\tau)\mathbf{n} + f_2(u_n, u_\tau)\boldsymbol{\tau}] = 0, \quad \text{on } \partial\Omega \tag{90}$$

where

$$f_1(u_n, u_\tau) = \begin{cases} \frac{K_1 + K_2 \eta^2}{1 + \eta^2} u_n + \frac{\eta(K_1 - K_2)}{1 + \eta^2} u_\tau, & u_n \geq 0; \\ \frac{K_1 \eta^2 + K_2}{1 + \eta^2} u_n + \frac{\eta(K_1 - K_2)}{1 + \eta^2} u_\tau, & u_n < 0; \end{cases} \tag{91}$$

$$f_2(u_n, u_\tau) = \begin{cases} \frac{\eta(K_1 - K_2)}{1 + \eta^2} u_n + \frac{K_1 \eta^2 + K_2}{1 + \eta^2} u_\tau, & u_n \geq 0; \\ \frac{\eta(K_1 - K_2)}{1 + \eta^2} u_n + \frac{K_1 + K_2 \eta^2}{1 + \eta^2} u_\tau, & u_n < 0; \end{cases} \tag{92}$$

$$u_n = \mathbf{n} \cdot \mathbf{u}; \quad u_\tau = \boldsymbol{\tau} \cdot \mathbf{u}; \quad |\mathbf{u}| = \sqrt{\mathbf{u} \cdot \mathbf{u}} = \sqrt{u_n^2 + u_\tau^2}; \tag{93}$$

$$\eta = \frac{u_\tau}{|\mathbf{u}| + |u_n| + \epsilon}, \quad \epsilon > 0 \text{ is a constant of machine zero or smaller, e.g. } 10^{-18}; \tag{94}$$

$$K_1 = \frac{\lambda_1 - a_{11}\lambda_3}{1 - a_{11}}, \quad K_2 = \frac{\lambda_2 - a_{22}\lambda_4}{1 - a_{22}}; \tag{95}$$

$$\begin{cases} \lambda_1 = \xi_1/2 - \sqrt{(\xi_1/2)^2 + 1}; & \lambda_2 = \xi_2/2 - \sqrt{(\xi_2/2)^2 + 1}; \\ \lambda_3 = \xi_1/2 + \sqrt{(\xi_1/2)^2 + 1}; & \lambda_4 = \xi_2/2 + \sqrt{(\xi_2/2)^2 + 1}; \end{cases} \tag{96}$$

$$\xi_1 = (1 - \alpha)u_n + \alpha|\mathbf{u}|; \quad \xi_2 = (1 - \alpha)u_n - \alpha|\mathbf{u}|. \tag{97}$$

**OBC-B:**

Input:

- Boundary information: normal vector  $\mathbf{n}$ , tangent vector  $\boldsymbol{\tau}$ .

Boundary condition: same as equation (90),

$$-p\mathbf{n} + \nu\mathbf{n} \cdot \nabla\mathbf{u} - [f_1(u_n, u_\tau)\mathbf{n} + f_2(u_n, u_\tau)\boldsymbol{\tau}] = \mathbf{0}, \quad \text{on } \partial\Omega$$

where

$$f_1(u_n, u_\tau) = \frac{1}{2} [(u_n - |u_n|)u_n + \alpha u_\tau^2]; \quad f_2(u_n, u_\tau) = \frac{1}{2} u_\tau [(1 - \alpha)u_n - |u_n|]; \tag{98}$$

$$\alpha = \frac{|u_n|}{|\mathbf{u}| + |u_n| + \epsilon}; \tag{99}$$

$u_n$  and  $u_\tau$  are defined by (93), and  $\epsilon$  is defined by (94).

**OBC-C:**

Input:

- Boundary information: normal vector  $\mathbf{n}$ , tangent vector  $\boldsymbol{\tau}$ .

Boundary condition: same as equation (90),

$$-p\mathbf{n} + \nu\mathbf{n} \cdot \nabla\mathbf{u} - [f_1(u_n, u_\tau)\mathbf{n} + f_2(u_n, u_\tau)\boldsymbol{\tau}] = \mathbf{0}, \quad \text{on } \partial\Omega$$

where  $f_1(u_n, u_\tau)$  and  $f_2(u_n, u_\tau)$  are given by equations (91)–(92), with the variables involved therein given by equations (93)–(97), and

$$\alpha = \frac{|u_n|}{|\mathbf{u}| + |u_n| + \epsilon}; \tag{100}$$

$$a_{11} = a_{22} = \frac{J_t - 1}{J_t + 1}; \tag{101}$$

$$J_t = \begin{cases} \frac{|u_n||\mathbf{u}|^2}{\frac{\sqrt{\xi_1^2+4}}{1+\eta^2}(u_n+\eta u_\tau)^2 + \frac{\sqrt{\xi_2^2+4}}{1+\eta^2}(-\eta u_n+u_\tau)^2 + \epsilon}, & u_n \geq 0; \\ \frac{|u_n||\mathbf{u}|^2}{\frac{\sqrt{\xi_1^2+4}}{1+\eta^2}(\eta u_n+u_\tau)^2 + \frac{\sqrt{\xi_2^2+4}}{1+\eta^2}(u_n-\eta u_\tau)^2 + \epsilon}, & u_n < 0. \end{cases} \tag{102}$$

Three dimensions

**OBC-A:**

Input:

- Boundary information: normal vector  $\mathbf{n}$ , tangent vectors  $\boldsymbol{\tau}$  and  $\mathbf{s}$ .
- Constant parameters:  $a_{11}, a_{22}, a_{33}, \alpha_1$  and  $\alpha_2$ , where  $-1 \leq a_{11}, a_{22}, a_{33} < 1$  and  $0 \leq \alpha_1, \alpha_2 \leq \frac{1}{2}$ .

Boundary condition:

$$-p\mathbf{n} + \nu\mathbf{n} \cdot \nabla\mathbf{u} - [g_1(u_n, u_\tau, u_s)\mathbf{n} + g_2(u_n, u_\tau, u_s)\boldsymbol{\tau} + g_3(u_n, u_\tau, u_s)\mathbf{s}] = \mathbf{0}, \quad \text{on } \partial\Omega \tag{103}$$

where

$$\begin{bmatrix} g_1 \\ g_2 \\ g_3 \end{bmatrix} = \mathbf{S} \begin{bmatrix} \frac{\lambda_1 - a_{11}\lambda_4}{1 - a_{11}} & & \\ & \frac{\lambda_2 - a_{22}\lambda_5}{1 - a_{22}} & \\ & & \frac{\lambda_3 - a_{33}\lambda_6}{1 - a_{33}} \end{bmatrix} \mathbf{S}^T \begin{bmatrix} u_n \\ u_\tau \\ u_s \end{bmatrix}; \tag{104}$$

$$u_n = \mathbf{n} \cdot \mathbf{u}; \quad u_\tau = \boldsymbol{\tau} \cdot \mathbf{u}; \quad u_s = \mathbf{s} \cdot \mathbf{u}; \quad |\mathbf{u}| = \sqrt{\mathbf{u} \cdot \mathbf{u}} = \sqrt{u_n^2 + u_\tau^2 + u_s^2}; \tag{105}$$

$$\begin{cases} \lambda_1 = \xi_1/2 - \sqrt{(\xi_1/2)^2 + 1}; & \lambda_2 = \xi_2/2 - \sqrt{(\xi_2/2)^2 + 1}; & \lambda_3 = \xi_3/2 - \sqrt{(\xi_3/2)^2 + 1}; \\ \lambda_4 = \xi_1/2 + \sqrt{(\xi_1/2)^2 + 1}; & \lambda_5 = \xi_2/2 + \sqrt{(\xi_2/2)^2 + 1}; & \lambda_6 = \xi_3/2 + \sqrt{(\xi_3/2)^2 + 1}; \end{cases} \tag{106}$$

$$\mathbf{S}_{3 \times 3} = [\mathbf{Z}_1 \mathbf{Z}_2 \mathbf{Z}_3] \tag{107}$$

$$\xi_i, \mathbf{Z}_i \ (i = 1, 2, 3) \text{ are eigen-values, eigen-vectors of } \begin{bmatrix} u_n & \alpha_1 u_\tau & \alpha_2 u_s \\ \alpha_1 u_\tau & (1 - 2\alpha_1)u_n & 0 \\ \alpha_2 u_s & 0 & (1 - 2\alpha_2)u_n \end{bmatrix}. \tag{108}$$

**OBC-B:**

Input:

- Boundary information: normal vector  $\mathbf{n}$ , tangent vectors  $\boldsymbol{\tau}$  and  $\mathbf{s}$ .

Boundary condition: same as equation (103),

$$-p\mathbf{n} + \nu\mathbf{n} \cdot \nabla \mathbf{u} - [g_1(u_n, u_\tau, u_s)\mathbf{n} + g_2(u_n, u_\tau, u_s)\boldsymbol{\tau} + g_3(u_n, u_\tau, u_s)\mathbf{s}] = 0, \quad \text{on } \partial\Omega$$

where

$$\begin{cases} g_1(u_n, u_\tau, u_s) = \frac{1}{2} [(u_n - |u_n|)u_n + \alpha_1 u_\tau^2 + \alpha_2 u_s^2]; \\ g_2(u_n, u_\tau, u_s) = \frac{1}{2} u_\tau [(1 - \alpha_1)u_n - |u_n|]; \\ g_3(u_n, u_\tau, u_s) = \frac{1}{2} u_s [(1 - \alpha_2)u_n - |u_n|]; \end{cases} \tag{109}$$

$$\alpha_1 = \alpha_2 = \frac{|u_n|}{|\mathbf{u}| + |u_n| + \epsilon}. \tag{110}$$

**OBC-C:**

Input:

- Boundary information: normal vector  $\mathbf{n}$ , tangent vectors  $\boldsymbol{\tau}$  and  $\mathbf{s}$ .

Boundary condition: same as equation (103),

$$-p\mathbf{n} + \nu\mathbf{n} \cdot \nabla \mathbf{u} - [g_1(u_n, u_\tau, u_s)\mathbf{n} + g_2(u_n, u_\tau, u_s)\boldsymbol{\tau} + g_3(u_n, u_\tau, u_s)\mathbf{s}] = 0, \quad \text{on } \partial\Omega$$

where  $g_1, g_2$  and  $g_3$  are given by equation (104) with the variables involved therein given by equations (105)–(108),  $\alpha_1$  and  $\alpha_2$  are given by equation (110), and

$$a_{11} = a_{22} = a_{33} = \frac{J_t - 1}{J_t + 1}; \quad J_t = \frac{|u_n||\mathbf{u}|^2}{Y_1 V_1^2 + Y_2 V_2^2 + Y_3 V_3^2 + \epsilon}; \tag{111}$$

$$\begin{bmatrix} V_1 \\ V_2 \\ V_3 \end{bmatrix} = \mathbf{S}^T \begin{bmatrix} u_n \\ u_\tau \\ u_s \end{bmatrix}; \quad Y_i = \sqrt{\xi_i^2 + 4}, \quad i = 1, 2, 3. \tag{112}$$

**Appendix C. Numerical algorithm**

This appendix summarizes our algorithm for solving the equations (1a)–(1b), together with the boundary conditions (71) and (72). This is based on the scheme originally developed in [10] (in Section 2.4 of [10]).

We modify the outflow/open boundary condition (72) slightly by adding a source term as follows,

$$-p\mathbf{n} + \nu\mathbf{n} \cdot \nabla \mathbf{u} - \mathbf{E}(\mathbf{u}, \partial\Omega_o) = \mathbf{f}_b(\mathbf{x}, t), \quad \text{on } \partial\Omega_o \tag{113}$$

where  $\mathbf{f}_b$  is a prescribed source term on  $\partial\Omega_o$  for the purpose of numerical testing only, and it will be set to  $\mathbf{f}_b = 0$  in actual simulations.  $\mathbf{E}(\mathbf{u}, \partial\Omega_o)$  is given by (73); see also the summary in Appendix B.

The following algorithm is for equations (1a)–(1b), together with the boundary conditions (71) on  $\partial\Omega_d$  and (113) on  $\partial\Omega_o$ . Let  $n \geq 0$  denote the time step index, and  $(\cdot)^n$  denote the variable  $(\cdot)$  at time step  $n$ . Let  $J$  ( $J = 1$  or  $2$ ) denote the temporal order of accuracy of the scheme. Given  $\mathbf{u}^n$ , we compute  $(p^{n+1}, \mathbf{u}^{n+1})$  successively in a de-coupled manner in two steps:

For  $p^{n+1}$ :

$$\frac{\gamma_0 \tilde{\mathbf{u}}^{n+1} - \hat{\mathbf{u}}}{\Delta t} + \mathbf{u}^{*,n+1} \cdot \nabla \mathbf{u}^{*,n+1} + \nabla p^{n+1} + \nu \nabla \times \nabla \times \mathbf{u}^{*,n+1} = \mathbf{f}^{n+1} \tag{114a}$$

$$\nabla \cdot \tilde{\mathbf{u}}^{n+1} = 0 \tag{114b}$$

$$\mathbf{n} \cdot \tilde{\mathbf{u}}^{n+1} = \mathbf{n} \cdot \mathbf{w}^{n+1}, \quad \text{on } \partial\Omega_d \tag{114c}$$

$$p^{n+1} = \nu \mathbf{n} \cdot \nabla \mathbf{u}^{*,n+1} \cdot \mathbf{n} - \mathbf{n} \cdot \mathbf{E}(\mathbf{u}^{*,n+1}, \partial\Omega_o) - \mathbf{f}_b^{n+1} \cdot \mathbf{n}, \quad \text{on } \partial\Omega_o. \tag{114d}$$

For  $\mathbf{u}^{n+1}$ :

$$\frac{\gamma_0 \mathbf{u}^{n+1} - \gamma_0 \tilde{\mathbf{u}}^{n+1}}{\Delta t} - \nu \nabla^2 \mathbf{u}^{n+1} = \nu \nabla \times \nabla \times \mathbf{u}^{*,n+1} \tag{115a}$$

$$\mathbf{u}^{n+1} = \mathbf{w}^{n+1}, \quad \text{on } \partial\Omega_d \tag{115b}$$

$$\mathbf{n} \cdot \nabla \mathbf{u}^{n+1} = \frac{1}{\nu} \left[ p^{n+1} \mathbf{n} + \mathbf{E}(\mathbf{u}^{*,n+1}, \partial\Omega_o) - \nu (\nabla \cdot \mathbf{u}^{*,n+1}) \mathbf{n} + \mathbf{f}_b^{n+1} \right], \quad \text{on } \partial\Omega_o. \tag{115c}$$

In the above equations,  $\Delta t$  is the time step size,  $\mathbf{n}$  is the outward-pointing unit vector normal to the boundary, and  $\tilde{\mathbf{u}}^{n+1}$  is an auxiliary variable approximating  $\mathbf{u}^{n+1}$ .  $\mathbf{u}^{*,n+1}$  is a  $J$ -th order explicit approximation of  $\mathbf{u}^{n+1}$ ,

$$\mathbf{u}^{*,n+1} = \begin{cases} \mathbf{u}^n, & J = 1, \\ 2\mathbf{u}^n - \mathbf{u}^{n-1}, & J = 2. \end{cases} \tag{116}$$

$\hat{\mathbf{u}}$  and the constant  $\gamma_0$  are such that  $\frac{1}{\Delta t}(\gamma_0 \mathbf{u}^{n+1} - \hat{\mathbf{u}})$  approximates  $\frac{\partial \mathbf{u}}{\partial t}|^{n+1}$  with a  $J$ -th order backward differentiation formula, and they are given by

$$\hat{\mathbf{u}} = \begin{cases} \mathbf{u}^n, & J = 1, \\ 2\mathbf{u}^n - \frac{1}{2}\mathbf{u}^{n-1}, & J = 2, \end{cases} \quad \gamma_0 = \begin{cases} 1, & J = 1, \\ \frac{3}{2}, & J = 2. \end{cases} \tag{117}$$

By taking the  $L^2$  inner products between a test function and equation (114a), one can obtain the weak form about  $p^{n+1}$ . By taking the  $L^2$  between a test function and the equation obtained by summing up equations (114a) and (115a), one can get the weak form about  $\mathbf{u}^{n+1}$ . Let  $H^1_{p0}(\Omega) = \{ v \in H^1(\Omega) : v|_{\partial\Omega_o} = 0 \}$ , and  $H^1_{u0}(\Omega) = \{ v \in H^1(\Omega) : v|_{\partial\Omega_d} = 0 \}$ . Let  $q \in H^1_{p0}(\Omega)$  and  $\varphi \in H^1_{u0}(\Omega)$  denote the test functions for the pressure and velocity. Then the weak form for  $p^{n+1}$  is

$$\int_{\Omega} \nabla p^{n+1} \cdot \nabla q = \int_{\Omega} \mathbf{G}^{n+1} \cdot \nabla q - \nu \int_{\partial\Omega_d \cup \partial\Omega_o} \mathbf{n} \times \boldsymbol{\omega}^{*,n+1} \cdot \nabla q - \frac{\gamma_0}{\Delta t} \int_{\partial\Omega_d} \mathbf{n} \cdot \mathbf{w}^{n+1} q, \quad \forall q \in H^1_{p0}(\Omega), \tag{118}$$

where  $\boldsymbol{\omega}^{*,n+1} = \nabla \times \mathbf{u}^{*,n+1}$ , and  $\mathbf{G}^{n+1} = \mathbf{f}^{n+1} + \frac{\hat{\mathbf{u}}}{\Delta t} - \mathbf{u}^{*,n+1} \cdot \nabla \mathbf{u}^{*,n+1}$ . The weak form for  $\mathbf{u}^{n+1}$  is

$$\begin{aligned} \frac{\gamma_0}{\nu \Delta t} \int_{\Omega} \mathbf{u}^{n+1} \varphi + \int_{\Omega} \nabla \varphi \cdot \nabla \mathbf{u}^{n+1} &= \frac{1}{\nu} \int_{\Omega} (\mathbf{G}^{n+1} - \nabla p^{n+1}) \varphi \\ &+ \frac{1}{\nu} \int_{\partial\Omega_o} \left[ p^{n+1} \mathbf{n} + \mathbf{E}(\mathbf{u}^{*,n+1}, \partial\Omega_o) + \mathbf{f}_b^{n+1} - \nu (\nabla \cdot \mathbf{u}^{*,n+1}) \mathbf{n} \right] \varphi, \quad \forall \varphi \in H^1_{u0}(\Omega). \end{aligned} \tag{119}$$

The weak forms (118) and (119) can be discretized in space using a high-order spectral element method [10] or a combined spectral-element and Fourier-spectral method [11,8].

Given  $\mathbf{u}^n$ , the following operations are involved in the final algorithm for computing  $p^{n+1}$  and  $\mathbf{u}^{n+1}$ : (i) Solve equation (118), together with the Dirichlet condition (114d) on  $\partial\Omega_o$ , for  $p^{n+1}$ ; (ii) Solve equation (119), together with the Dirichlet condition (115b) on  $\partial\Omega_d$ , for  $\mathbf{u}^{n+1}$ .

The above discussion on the implementation of the numerical scheme applies to  $C^0$  spectral-element and finite-element type spatial discretizations. The scheme can also be implemented using other spatial discretization techniques; see [12,10] for comments and suggestions in this regard. The following are the equations that a possible finite-difference implementation can use, which follow the suggestions from [10] (see page 308, last paragraph of section 2.3 in [10]):

$$\nabla^2 p^{n+1} = \nabla \cdot \left( \mathbf{f}^{n+1} + \frac{\hat{\mathbf{u}}}{\Delta t} - \mathbf{u}^{*,n+1} \cdot \nabla \mathbf{u}^{*,n+1} \right); \tag{120a}$$

$$\frac{\partial p^{n+1}}{\partial n} = \mathbf{n} \cdot \left( \mathbf{f}^{n+1} + \frac{\hat{\mathbf{u}}}{\Delta t} - \mathbf{u}^{*,n+1} \cdot \nabla \mathbf{u}^{*,n+1} \right) - \nu \mathbf{n} \cdot \nabla \times \boldsymbol{\omega}^{*,n+1} - \frac{\gamma_0}{\Delta t} \mathbf{n} \cdot \mathbf{w}^{n+1}, \quad \text{on } \partial\Omega_d; \tag{120b}$$

$$p^{n+1} = \nu \mathbf{n} \cdot \nabla \mathbf{u}^{*,n+1} \cdot \mathbf{n} - \mathbf{n} \cdot \mathbf{E}(\mathbf{u}^{*,n+1}, \partial\Omega_o) - \mathbf{f}_b^{n+1} \cdot \mathbf{n}, \quad \text{on } \partial\Omega_o. \tag{120c}$$

$$\frac{\gamma_0}{\nu \Delta t} \mathbf{u}^{n+1} - \nabla^2 \mathbf{u}^{n+1} = \frac{1}{\nu} \left( \mathbf{f}^{n+1} + \frac{\hat{\mathbf{u}}}{\Delta t} - \mathbf{u}^{*,n+1} \cdot \nabla \mathbf{u}^{*,n+1} - \nabla p^{n+1} \right); \tag{121a}$$

$$\mathbf{u}^{n+1} = \mathbf{w}^{n+1}, \quad \text{on } \partial\Omega_d; \tag{121b}$$

$$\frac{\partial \mathbf{u}^{n+1}}{\partial n} = \frac{1}{\nu} \left[ \mathbf{f}_b^{n+1} + \mathbf{E}(\mathbf{u}^{*,n+1}, \partial\Omega_o) + p^{n+1} \mathbf{n} - \nu (\nabla \cdot \mathbf{u}^{*,n+1}) \mathbf{n} \right], \quad \text{on } \partial\Omega_o. \tag{121c}$$

In the above equations, (120a) is obtained by taking the divergence of equation (114a) and using equation (114b), (120b) is obtained by taking the inner product between equation (114a) and the unit normal vector  $\mathbf{n}$  of  $\partial\Omega_d$ , and (121a) is obtained by summing up equations (114a) and (115a). Equations (120c), (121b) and (121c) are the same as equations (114d), (115b) and (115c). One can solve equations (120a)–(120c) for  $p^{n+1}$ , and then solve equations (121a)–(121c) for  $\mathbf{u}^{n+1}$ .

## References

- [1] Y. Bazilevs, J.R. Hohean, T.J.R. Hughes, R.D. Moser, Y. Zhang, Patient-specific isogeometric fluid-structure interaction analysis of thoracic aortic blood flow due to implantation of the Jarvik 2000 left ventricular assist device, *Comput. Methods Appl. Mech. Eng.* 198 (2009) 3534–3550.
- [2] C. Bertoglio, A. Caiazzo, A tangential regularization method for backflow stabilization in hemodynamics, *J. Comput. Phys.* 261 (2014) 162–171.
- [3] C. Bertoglio, A. Caiazzo, A Stokes-residual backflow stabilization method applied to physiological flows, *J. Comput. Phys.* 313 (2016) 260–278.
- [4] C. Bertoglio, A. Caiazzo, Y. Bazilevs, M. Braack, M. Esmaily, V. Gravemeier, A.L. Marsden, O. Pironeau, I.E. Vignon-Clementel, W.A. Wall, Benchmark problems for numerical treatment of backflow at open boundaries, *Int. J. Numer. Methods Biomed. Eng.* 34 (2018) e2918.
- [5] M. Braack, P.B. Mucha, Directional do-nothing condition for the Navier-Stokes equations, *J. Comput. Math.* 32 (2014) 507–521.
- [6] C.-H. Bruneau, P. Fabrie, Effective downstream boundary conditions for incompressible Navier-Stokes equations, *Int. J. Numer. Methods Fluids* 19 (1994) 693–705.
- [7] C.-H. Bruneau, P. Fabrie, New efficient boundary conditions for incompressible Navier-Stokes equations: a well-posedness result, *Math. Model. Numer. Anal.* 30 (1996) 815–840.
- [8] S. Dong, Direct numerical simulation of turbulent Taylor-Couette flow, *J. Fluid Mech.* 587 (2007) 373–393.
- [9] S. Dong, An outflow boundary condition and algorithm for incompressible two-phase flows with phase field approach, *J. Comput. Phys.* 266 (2014) 47–73.
- [10] S. Dong, A convective-like energy-stable open boundary condition for simulations of incompressible flows, *J. Comput. Phys.* 302 (2015) 300–328.
- [11] S. Dong, G.E. Karniadakis, DNS of flow past stationary and oscillating cylinder at  $Re = 10,000$ , *J. Fluids Struct.* 20 (2005) 14–23.
- [12] S. Dong, G.E. Karniadakis, C. Chrysosostomidis, A robust and accurate outflow boundary condition for incompressible flow simulations on severely-truncated unbounded domains, *J. Comput. Phys.* 261 (2014) 83–105.
- [13] S. Dong, G.E. Karniadakis, A. Ekmecki, D. Rockwell, A combined DNS-PIV study of the turbulent near wake, *J. Fluid Mech.* 569 (2006) 185–207.
- [14] S. Dong, J. Shen, A pressure-correction scheme for generalized form of energy-stable open boundary conditions for incompressible flows, *J. Comput. Phys.* 291 (2015) 254–278.
- [15] S. Dong, X. Wang, A rotational pressure-correction scheme for incompressible two-phase flows with open boundaries, *PLoS ONE* 11 (5) (2016) e0154565.
- [16] M. Feistauer, T. Neustupa, On the existence of a weak solution of viscous incompressible flow past a cascade of profiles with an arbitrarily large inflow, *J. Math. Fluid Mech.* 15 (2013) 701–715.
- [17] R.K. Finn, Determination of the drag on a cylinder at low Reynolds numbers, *J. Appl. Phys.* 24 (1953) 771–773.
- [18] J. Fouchet-Incaux, Artificial boundaries and formulations for the incompressible Navier-Stokes equations. applications to air and blood flows, *SeMA J.* 64 (2014) 1–40.
- [19] N.S. Ghaisas, D.A. Shetty, S.H. Frankel, Large eddy simulation of turbulent horizontal buoyant jets, *J. Turbul.* 16 (2015) 772–808.
- [20] V. Gravemeier, A. Comerford, L. Yoshihara, M. Ismail, W.A. Wall, A novel formulation for Neumann inflow boundary conditions in biomechanics, *Int. J. Numer. Methods Biomed. Eng.* 28 (2012) 560–573.
- [21] P.M. Gresho, Incompressible fluid dynamics: some fundamental formulation issues, *Annu. Rev. Fluid Mech.* 23 (1991) 413–453.
- [22] J.G. Heywood, R. Rannacher, S. Turek, Artificial boundaries and flux and pressure: conditions for the incompressible Navier-Stokes equations, *Int. J. Numer. Methods Fluids* 22 (1996) 325–352.
- [23] M. Ismail, V. Gravemeier, A. Comerford, W.A. Wall, A stable approach for coupling multidimensional cardiovascular and pulmonary networks based on a novel pressure-flow rate or pressure-only Neumann boundary condition formulation, *Int. J. Numer. Methods Biomed. Eng.* 30 (2014) 447–469.
- [24] G.E. Karniadakis, S.J. Sherwin, *Spectral/hp Element Methods for Computational Fluid Dynamics*, 2nd edn., Oxford University Press, 2005.
- [25] M. Lanzendorfer, J. Stebel, On pressure boundary conditions for steady flows of incompressible fluids with pressure and shear rate dependent viscosities, *Appl. Math.* 56 (2011) 265–285.
- [26] M.E. Moghadam, Y. Bazilevs, T.-Y. Hsia, I.E. Vignon-Clementel, A.L. Marsden, A comparison of outlet boundary treatments for prevention of backflow divergence with relevance to blood flow simulations, *Comput. Mech.* 48 (2011) 277–291.
- [27] C. Norberg, Fluctuating lift on a circular cylinder: review and new measurements, *J. Fluids Struct.* 17 (2003) 57–96.
- [28] J. Nordstrom, A roadmap to well posed and stable problems in computational physics, *J. Sci. Comput.* 71 (2017) 365–385.
- [29] J. Nordstrom, C.L. Cognata, Energy-stable boundary conditions for the nonlinear incompressible Navier-Stokes equations, *Math. Comput.* 88 (2019) 665–690.
- [30] A. Porpora, P. Zunino, C. Vergara, M. Piccinelli, Numerical treatment of boundary conditions to replace branches in hemodynamics, *Int. J. Numer. Methods Biomed. Eng.* 28 (2012) 1165–1183.
- [31] A. Roshko, Experiments on the flow past a circular cylinder at very high Reynolds numbers, *J. Fluid Mech.* 10 (1961) 345–356.
- [32] R.L. Sani, P.M. Gresho, Resume and remarks on the open boundary condition minisymposium, *Int. J. Numer. Methods Fluids* 18 (1994) 983–1008.
- [33] S.J. Sherwin, G.E. Karniadakis, A triangular spectral element method: applications to the incompressible Navier-Stokes equations, *Comput. Methods Appl. Mech. Eng.* 123 (1995) 189–229.
- [34] D.J. Tritton, Experiments on the flow past a circular cylinder at low Reynolds numbers, *J. Fluid Mech.* 6 (1959) 547.
- [35] S.S. Varghese, S.H. Frankel, P.F. Fischer, Direct numerical simulation of stenotic flows. Part 1. Steady flow, *J. Fluid Mech.* 582 (2007) 253–280.
- [36] C. Wieselsberger, Recent statements on the laws of liquid and air resistance, *Phys. Z.* 22 (1921) 321–328.
- [37] C.H.K. Williamson, Vortex dynamics in a cylinder wake, *Annu. Rev. Fluid. Dyn.* 28 (1996) 477–539.
- [38] Z. Yang, S. Dong, Multiphase flows of  $N$  immiscible incompressible fluids: an outflow boundary condition and algorithm, *J. Comput. Phys.* 366 (2018) 33–70.
- [39] X. Zheng, S. Dong, An eigen-based high-order expansion basis for structured spectral elements, *J. Comput. Phys.* 230 (2011) 8573–8602.